HIGH-BANDWIDTH IDENTIFICATION AND COMPENSATION OF HYSTERETIC DYNAMICS

LIU LEI

NATIONAL UNIVERSITY OF SINGAPORE
2012

HIGH-BANDWIDTH IDENTIFICATION AND COMPENSATION OF HYSTERETIC DYNAMICS

LIU LEI
(B.Eng., HARBIN INSTITUTE OF TECHNOLOGY)

A THESIS SUBMITTED
FOR THE DEGREE OF DOCTOR OF PHILOSOPHY

NUS GRADUATE SCHOOL FOR INTEGRATIVE
SCIENCES AND ENGINEERING
NATIONAL UNIVERSITY OF SINGAPORE
2012

Declaration

I hereby declare that the thesis is my original work and it has been written by me in its entirety. I have duly acknowledged all the sources of information which have been used in the thesis.

This thesis has also not been submitted for any degree in any university previously.

2 NOV 2012

LIU LEI

Acknowledgments

I would like to express my most sincere gratitude and appreciation to all who helped me during my PhD candidature at the National University of Singapore. First, I would like to thank my supervisors, Professor Lee Tong Heng and Professor Tan Kok Kiong for their helpful discussions, support and encouragement. Their wisdom, vision, gentleness and devotion greatly brighten my research paths. Without their support and guidance, I would not have accomplished this thesis.

I would like to thank my parents and my wife for their endless love and support. Specially, I would like to express my deepest gratitude to my wife, Weiming for her love, understanding, supporting and inspiration. This thesis is dedicated to my family for their infinite stability margin.

I would also like to express my appreciation to all my friends who helped me in the last four years. Special thanks must be made to Dr Teo Chek Sing for his close collaboration and warmhearted help. Great thanks to Mr Yuan Jian and Miss Er Poi Voon for their revisions of my manuscripts and reports. Many thanks to Mr Liang Wenyu for his help of setting up dSPACE 1104 control platforms. Lots of thanks to Dr Huang Sunan and Dr Chen Si-Lu for their discussions. Many thanks to all my colleagues in Mechatronics

and Automation Lab for their friendship and help.

Finally, I am thankful to NUS Graduate School for Integrative Sciences and Engineering for providing the NGS scholarship to undertake my PhD research. Many thanks to Department of Electrical and Computer Engineering (ECE) for providing high-class laboratory environment. Special thanks also to the Mechatronics group of Singapore Institute of Manufacturing Technology (SIMTech).

Contents

Summary

Piezoelectric actuators (PAs) are widely used in precision engineering applications due to their capability of accurate tracking, such as nano-fabrication, dynamic imaging of molecules by using scanning probe microscopies (SPMs), and advanced spacecrafts with optical sensitive instruments. The requirements for the bandwidth and accuracy of these precise motion systems are clearly tight and stringent. It is often desirable to have precision motion at rates of several kHz, which may be higher than the resonant frequencies. However, PAs exhibit limited performance at high-bandwidth tracking. The dynamic tracking is typically slower than 10% of the resonant frequencies, because of the coupled hysteresis, creep and vibration dynamics.

To achieve precision motion control of PAs, accurate identification and compensation of hysteretic dynamics can be employed. In this thesis, the accurate identification and compensation of hysteretic dynamics in PAs are investigated at broadband frequencies. In the experimental studies, the high-bandwidth and precision motion of PAs are achieved, simultaneously.

First, at low frequencies, the identification and compensation of Preisach hysteresis are investigated by using singular value decomposition (SVD)-based least squares es-

timation. The Preisach-based inversion compensator is also presented to compensate the static hysteresis in PAs. With the inversion compensator, the feedback performance with PID tuning controller is significantly improved in the experimental studies.

As the input frequencies increase, the hysteretic dynamics becomes more significant. Thus, the electric and vibration dynamics of PAs are identified at high frequencies by using the identification result of Preisach hysteresis at low frequencies. The model-based composite controller is designed, which consists of a model-based inversion feedforward compensator and a PI tuning feedback controller. In the experimental studies, the precision tracking is achieved at rates higher than the resonant frequencies.

Furthermore, at broadband frequencies, a comprehensive identification of hysteretic dynamics is developed for PAs. The non-hysteretic dynamics, such as the creep, electric and vibration dynamics are identified first. Afterwards, the Preisach hysteresis is identified by using the specially designed input signals and sampling rules. The effectiveness of the identification strategy is validated in the experimental studies.

Finally, based on the identified hysteretic dynamics obtained by using the comprehensive method, the multirate-based controller is designed to achieve precision motion at higher bandwidth. The model-based inversion feedforward compensator consists of the inversions of the creep, Preisach hysteresis, electric and vibration dynamics. The discrete H_∞ controller is designed according to disturbances, modeling uncertainties and hardware limitations. In the experimental studies, the precision motion is achieved at rates higher than twice of the resonant frequency.

List of Tables

List of Figures

Nomenclature

Symbol	Meaning or Operation
PA	Piezoelectric Actuator
SPM	Scanning Probe Microscopes
RMS	Root Mean Square
SVD	Singular Value Decomposition
PE	Persistent Excitation
LVDT	Linear Variable Differential Transformer
DSP	Digital Signal Processing
PID	Proportional Integral Derivative
PI	Proportional Integral
ZOH	Zero Order Hold
DOF	Degree Of Freedom
ARMAX	Autoregressive-moving-average model with exogenous inputs
etc.	et cetera
f, v	Hysteresis output
S	Preisach plane
μ	Density function of Preisach hysteresis
$\hat{\mu}$	Estimated of μ
μ_{ij}	Discretization of μ
L	Discretization level of Preisach hysteresis
$\gamma_{\alpha\beta}$	Relay output
α, β	Parameter of Preisach plane
$u(t)$	Input voltage
X	Identified variable
$\hat{X}$	Identification of X
A, Y	Measured matrix and variable for identification
A^+	Pseudo inverse of A
U, Σ, V	SVD of $A^T A$

Symbol	Meaning or Operation
σ_i	Singular values
u_i, v_i	Vectors of SVD
r	Truncated value of singular values
Δ	Iteration step
ω_s	Angular frequency
t	Time
Γ	Preisach hysteresis
G_{e}	Creep dynamics
G_{v}	Vibration dynamics
G	Non-hysteretic Dynamics
y	Measured displacement of PAs
y_r	Desired displacement
K_{FF}	Feedforward controller
K_{FB}	Feedback controller
n	Noise
u_{fb}	Feedback control signal
u_{ff}	Feedforward control signal
ω_c	Crossover frequency
p_u	Ultimate period
g_m	Ultimate gain
T	Sampling interval
e_{h}	Relative error
τ	Time constant
ω_i, ω_j	Mode frequencies of PAs
ξ_i, ξ_j	Damping ratio
e_{RMS}	Relative RMS error
z_{ci}, p_{ci}	Zeroes and poles of creep dynamics
w_1	Performance weighting function
w_2	Control weighting function
w_n	Noise weighting function
w_d	Disturbance weighting function
δ_f	Feedforward error
Δ_δ	Unit complex uncertainty
f_{FF}	Feedforward sampling rate
f_{FB}	Feedback sampling rate

Chapter 1

Introduction

1.1 Background and Motivation

Piezoelectric actuators (PAs) are one of the most popular smart actuators which are increasingly appealing for precision motion control [1]. Directly driven PAs are investigated in this thesis, in which the inverse piezoelectric effect is used. To achieve sufficient travel span, stacking sequences of piezoelectric patches and motion amplifiers could be employed in practice. Additionally, instead of common joints, flexible joints could be used to avoid the friction nonlinearity. PAs have appealing properties, such as:

- *High bandwidth: PAs work well at rates of kHz [2].*
- *High accuracy: PAs can achieve sub-nano accuracy [1].*
- *Friction-free: Flexible joints are commonly used to avoid the friction nonlinearity.*

In precision engineering applications, PAs have been increasingly employed, such as in modern micro and nano fabrication [3, 4], dynamic imaging with scanning probe microscopes (SPMs) [5], and advanced spacecrafts with sensitive optical instruments.

Modern micro and nano fabrication: 3D nanofabrication by femtosecond laser direct writing [6], Nanoscale scratching [7], submicron lithography [8], diamond turning machines [9], etc.

Dynamic imaging with SPMs: Three-dimensional nano patterning and dynamic imaging of molecules [6, 7, 10, 11], nano-visualization of dynamic biomolecular processes [12–16], etc.

Advanced spacecrafts with sensitive optical instruments: Space telescopes [17], deep-space laser communication [18], space-based laser weapons [19], space-based interferometers [20], etc.

Various methods of modeling, identification and compensation have been investigated for PAs [21, 22], for instance:

- *Hysteresis modeling: Preisach and Prandtl-Ishlinskii are two popular mathematical models. Both static and dynamic hysteresis have been investigated.*

- *Hysteresis identification and inverse compensation: Various approaches of hysteresis identification have also been investigated, and the model-based inversion compensation based on the identified hysteresis is one direct and effective approach to eliminate the hysteresis.*

- *Feedback control: Various feedback controllers have been investigated to achieve precision motion control, consisting of the model-based and model-free controllers.*

With the development of ultra-accurate applications, more strict requirements are presented [23], which lay out the scope of current techniques.

- *High-bandwidth: In SPMs, the PAs are required to track at rates on the order of kHz, which may exceed the resonant frequencies of PAs. Currently, PAs typically operate at frequencies less than 10% of the resonant frequencies.*

- *High-accuracy: In addition to high-bandwidth requirements, high-accuracy is another requirement for PAs. Furthermore, the simultaneous high-bandwidth and high-accuracy are current requirements in which the precision tracking are required at rates possibly beyond the resonant frequencies.*

- *Feedforward control: Feedback controllers have been limited at frequencies higher than the resonant frequencies due to the measurement noise at high frequencies. Compared with feedback control, the model-based inversion feedforward compensation, which relies on the model identification, is an alternative method to increase the tracking rates and enhance the tracking accuracy at high frequencies, because feedforward controllers are effective to avoid the measurement noise which are more serious at high frequencies.*

1.2 Objectives and Challenges

PAs are widely applied in precision engineering to achieve nanometer scale tracking. However, the scanning accuracy of piezoelectric mechanisms over broadband frequencies

are limited due to inherent dynamic hysteresis. This phenomenon has been a key bottleneck to the use of piezoelectric mechanisms in fast and precision scanning applications.

The main objective of this thesis is to increase the bandwidth and enhance the accuracy of piezoelectric systems by proposing and identifying the models at broadband frequencies, including Preishach hysteresis, creep, electric and vibration dynamics.

1.3 Experimental Setup

The experimental setup consists of a piezoelectric stage, a linear voltage amplifier, a linear variable differential transformer (LVDT) displacement sensor and a dSPACE 1104 board. Fig. 1.1 illustrates the piezoelectric stage, amplifier and sensor conditioning. The travel of the stage is $100\mu m$. The amplifier is E-662 with the output voltage range of $[-20, 120]$V. The noise in the measurement signal is white noise with the root-mean-square (RMS) value of 0.009 μm.

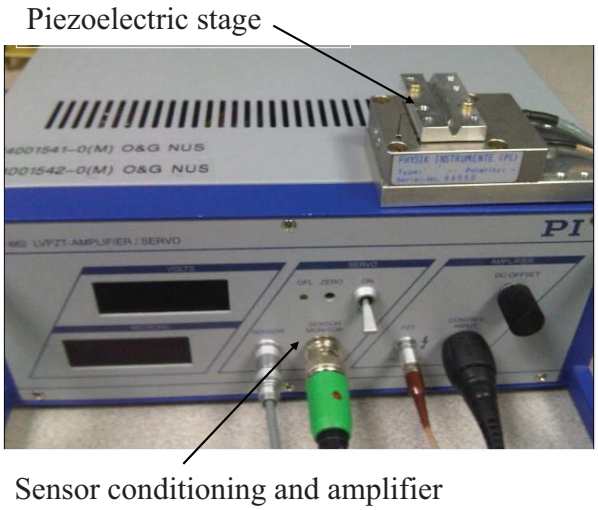

Figure 1.1: Experimental setup.

1.4 Contributions

This thesis aims to propose efficient identification and compensation of hysteretic dynamics of PAs to achieve precision motion control over a broadband range of frequencies. Based on the objectives and challenges listed in Section 1.2, the following contributions have been made in this thesis.

- *The SVD-based identification and compensation of Preisach hysteresis are investigated at low frequencies*
- *The model-based composite compensation of hysteretic dynamics is designed for both high-bandwidth and precision motion control of PAs*
- *The comprehensive identification of hysteretic dynamics in PAs is developed at broadband frequencies*
- *The multirate-based compensation controller is designed for precision motion control of PAs*

1.4.1 SVD-based Identification and Compensation of Preisach Hysteresis

The singular value decomposition (SVD)-based identification and compensation of the hysteretic phenomenon in piezoelectric actuators (PAs) are addressed using a Preisach model. First, the accurate identification method of Preisach hysteresis is presented, containing the SVD-based least squares algorithm and revision approach of the identification through updating of the SVD. With the identified parameters and a log of

the memory curve, a Preisach-based inversion compensator is constructed which is complemented with a feedback controller to address the inevitable and residual modeling errors. Experimental results are furnished for both the identification and compensation approaches. The Preisach-based feedforward controller significantly improves the tracking performance and reduces the root-mean-square (RMS) tracking error of a PID tuning controller by 76.7% and 89% at 1Hz and 25Hz, respectively. With the proposed composite controller, the percent-RMS errors at 1 Hz and 25 Hz are reduced to 0.035% and 0.31% respectively.

1.4.2 Comprehensive Identification of Hysteretic Dynamics in PAs at Broadband Frequencies

A comprehensive approach is provided to identify the hysteresis and coupled non-hysteretic dynamics of PAs over a broad range of frequencies. The approach leverages on the special characteristics and distinctions of the hysteretic and non-hysteretic components to identify them in sequence, efficiently. The non-hysteretic dynamics is identified using square wave input signals. The creep dynamics is identified using an input signal with a long period. Conversely, electric and vibration dynamics are identified using an input signal with a small period. Moreover, the drift due to the creep is eliminated by employing its model inversion. The Preisach hysteresis is identified with specially designed harmonic input signals and sampling rules, which overcomes the persistent excitation (PE) problem of hysteresis identification and improves the computational efficiency. Simulation and experiments are conducted to validate the effectiveness of the

identification approach.

1.4.3 Model-based Composite Compensation of Hysteretic Dynamics

A simple model identification and composite control strategy without hysteresis measurement for such applications is introduced. First, least squares estimation using harmonic signals is applied to achieve the Preisach density function. Next, the hysteresis output is estimated, such that the non-hysteretic dynamics can be identified. The discrete composite control strategy is proposed with a feedforward-feedback structure. The feedforward controller is the primary component designed for performance. The secondary PI feedback controller is employed to suppress disturbances for robustness. Finally, the identification and composite control strategy is implemented with a dSPACE 1104 board for a real piezoelectric actuator setup. The experimental results indicate that adequate scanning performance can be sustained at a rate higher than the first resonant frequency.

1.4.4 Multirate-based Compensation Control of PAs for High-bandwidth and Precision Tracking

To track trajectories at rates higher than the resonant frequencies of the PAs, this chapter presents a multirate-based composite controller consisting of a slow sampled H_∞ feedback controller and a fast sampled feedforward controller. The feedback controller is designed for stability and robustness in the presence of disturbances and modeling errors. The feedforward controller is designed for high-bandwidth tracking by reducing phase-lag and gain distortion. The proposed composite controller is realized in a piezoelectric

stage based on a dSPACE 1104 board. With a sampling rate of 1 kHz in the feedback loop and a sampling rate of 40 kHz in the feedforward branch, the RMS tracking error at 1 kHz (2.2 times of the resonant frequency) is less than 2.3% of the trajectory amplitude.

1.5 Organization of Thesis

The organization of this thesis is as follows. Chapter 2 investigates the SVD-based identification and compensation of Preisach hysteresis at low frequencies. Chapter 3 presents the model-based composite control for high-bandwidth and precision scanning of PAs. Chapter 4 develops the comprehensive identification of hysteretic dynamics in PAs. Chapter 5 presents the multirate-based controller design for simultaneous high-bandwidth and precision tracking. Finally, Chapter 6 concludes this thesis and presents possible future work.

Chapter 2

SVD-based Identification and Compensation of Preisach Hysteresis

2.1 Introduction

Hysteresis contributes to the main uncertainty, which affects the control performance, among the nonlinearities present in piezo systems. In the open loop, the maximum error from hysteresis is 10%-15% of the total displacement of PAs [24]. This error may not be tolerable for precision applications. The modeling and identification of the hysteresis nonlinearity in PAs can enhance the control performance and the identification accuracy of non-hysteretic dynamics at higher frequencies. Currently, to avoid the hysteresis effect, only 5% of the travel range of PAs is used to identify the transfer functions [25]. Moreover, the input voltage slower than 1Hz is typically not used for identification due to the hysteresis nonlinearity.

This chapter focuses on the hysteresis identification issue of PAs. The identification result is applied at higher frequencies. PAs are typically quasi-static at low frequencies [26],

and can be represented by a rate-independent hysteresis model. Generally, hysteresis models can be classified into mathematical models and physical models [27–29]. The mathematical model is a vehicle to provide an input-output relationship of the actual system and it is usually more amenable to practical use for identification and control. Conversely, the physical model is constructed based on physical laws applied to the phenomenon of hysteresis and thus the model is intuitive to understanding, but it is typically in a complex form which is difficult to be identified and not often used for control purposes [30]. In the current literature, the examples of mathematical models are the Preisach model and the Prandtl-Ishlinskii (P-I) model [31, 32]. Moreover, the P-I model is a special case of the Preisach model [33].

The Preisach model is popular and effective to describe the quasi-static hysteresis of PAs, but the accurate identification of the Preisach model is still not solved well due to the large number of split lattices and the corresponding density values. Preisach hysteresis is a static nonlinearity and has global memories. All the extreme values of input history can affect current and future outputs. The classical Preisach model satisfies the wiping out and the congruency properties [29]. Other mathematical models, such as the Bouc-Wen model [34, 35], have also been applied to describe hysteresis behaviors of PAs. Compared to the Preisach model, these models are in a highly nonlinear form, possibly including dynamical parameters which are difficult to be laid out in a form for parameter identification and model-based inversion compensation.

Modeling of the Preisach hysteresis entails essentially the identification of Preisach

density functions. Hu and Song identified these functions by differentiating the measurements [36, 37], possibly causing the identified functions to be sensitive to measurement noise. Tan and Iyer developed recursive schemes for parameter identification and designed a closest-match algorithm for the compensation of the Preisach hysteresis [38,39]. Henze provided approaches for the identification of the Preisach function based on different distribution characteristics [40], but these approaches rely on assumptions of the form of the density functions and are typically not amenable to be used for the purpose of producing a model for hysteresis compensation.

As evident in the published literature, approximate Preisach density functions can be identified more efficiently through a discretized Preisach plane by transforming the double integral of density functions to a numerical summation, thus reducing the effort to an identification of a set of finite parameters in the linear regression form. Furthermore, no restrictive assumption on the density functions is necessary. However, to achieve an accurate and smooth approximation of these functions from a discretized plane, a large number of the split lattices will be needed and equivalently, a large number of model parameters is to be determined from the data. This leads to a requirement to collect a large amount of sufficiently exciting data to satisfy a persistent excitation (PE) condition for parameter estimation [39, 41]. Under practical conditions, this issue is equivalent to solving an ill-conditioned inverse problem [42].

Various hysteresis compensation approaches have been investigated. Aphale proposed a high-gain feedback controller to suppress hysteresis, but the achieved bandwidth with

adequate tracking accuracy is significantly decreased [43]. The compensation of hysteresis through model-based inversion is adopted in some cases [44], Tao designed an adaptive controller with a parameterized inverse hysteresis [45], but the model is too simple to describe global memories of PAs. Chen developed adaptive techniques without requiring an inversion of the hysteresis, but the density function is still assumed in the controller [46]. This chapter presents a Preisach-based inversion feedforward controller without the measurement of hysteresis output in real-time.

The organization of this chapter is as follows. Section 2.2 presents the least squares estimation algorithm and the revision of identification, both based on singular value decomposition (SVD). The SVD-based approach can address the ill-conditioned issue as it uses a complete orthogonal decomposition to compute a pseudo inverse solution in the least squares sense. Additionally, the SVD-based updating can reduce the computing time and provide more precise estimation of the density function. Section 2.3 adopts a feedback-feedforward control structure for hysteresis compensation and motion tracking. A feedforward compensator constructs an inversion of the hysteresis phenomenon to minimize the hysteresis effect. A PID feedback controller is employed to improve the tracking performance by addressing the residual effects arising from incomplete feedforward cancelation. Section 2.4 provides experimental studies on a piezoelectric stage to demonstrate the proposed identification and compensation strategy. Though the Preisach identification is implemented at low frequencies, it is effective to reduce the tracking error at higher frequencies. Section 2.5 makes a discussion of experimental

results. Finally, Section 2.6 concludes the chapter.

2.2 Parameter Identification of Preisach Hysteresis

2.2.1 Preisach Hysteresis

The hysteresis relay constitutes the basic element of hysteresis in PAs. The outputs of these operators are weighted by the Preisach density function $\mu(\alpha, \beta)$ and then summed continuously over possible values of α and β. The relationship between input voltage and hysteresis output of PAs is represented as [29]

$$f(t) = \iint_{\alpha \geq \beta} \mu(\alpha, \beta) \gamma_{\alpha\beta}[u(t)] d\alpha d\beta \tag{2.1}$$

where $\mu(\alpha, \beta)$ is the density function and $f(t)$ is the hysteresis output. At low frequencies, typically less than 1Hz, $f(t)$ is approximately equal to the piezo displacement. α and β are the switching threshold values of the hysteresis operator $\gamma_{\alpha\beta}[u(t)]$, as shown in Fig. 2.1(a).

In the Preisach model (2.1), the input $u(t)$ is first applied to all the hysteresis operators $\gamma_{\alpha\beta}[u(t)]$. The hysteresis output can thus be considered to be a superposition of a continuous set of two-position relay operators $\gamma_{\alpha\beta}[u(t)]$ over the range of input signal. Let S be Preisach triangle which is formed by $\alpha \geq \beta$ and the saturation value of input voltages, shown in Fig. 2.1(b), and can be divided to S^+ with $\gamma_{\alpha\beta}[u(t)] = \theta_1$ and S^- with $\gamma_{\alpha\beta}[u(t)] = \theta_2$. In PAs with positive input voltage, $\theta_1 = 1$ and $\theta_2 = 0$ can be used.

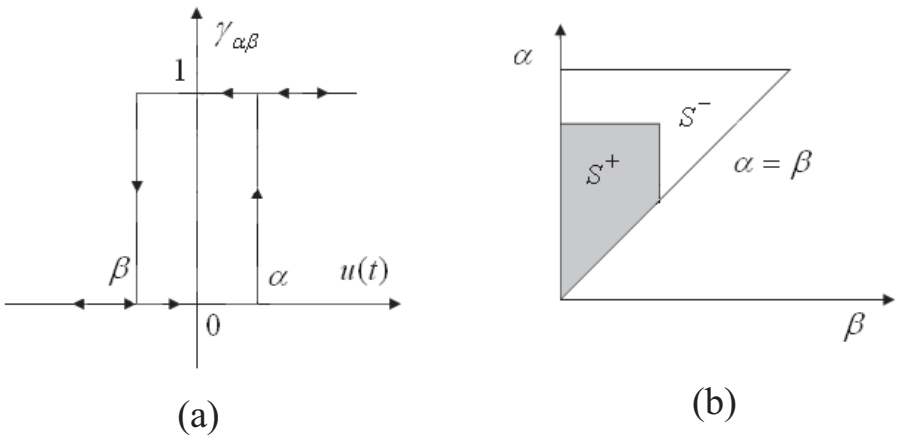

Figure 2.1: (a): Preisach relay operator. (b): Preisach triangle.

Identification of the Preisach model essentially entails the identification of the density functions. In the continuous form, the parameter $\mu(\alpha, \beta)$ are continuous over the limiting region and it is thus difficult to identify the continuous Preisach functions. In this section, the limiting region will be considered to be comprising of discrete lattices. Each lattice cell may have a weight assigned to it which is the discrete equivalence of a specific lattice density. The hysteresis output can be computed by transforming the double integral to a numerical summation as shown in Eq. (2.2) which is also linear-in-parameter and suitable for estimation and control.

$$f(k) = \sum_{i=1}^{L} \sum_{j=1}^{i} \mu_{ij} \gamma_{ij}[u(k)] s_{ij} \tag{2.2}$$

where $f(k)$ and $u(k)$ are the hysteresis output and input voltage at time instant k, respectively, s_{ij} denotes the area of lattice (i, j). The Preisach plane is discretized into $L \times L$ lattices. Thus effectively with the symmetry, there are $L(L+1)/2$ lattices in Preisach triangle to be identified.

Let $v_{ij} = \mu_{ij} s_{ij}$. Moreover, s_{ij} is known. The $f(k)$ at time k is rewritten as

$$f(k) \quad = \quad A_k X \tag{2.3}$$

where $A_k = [\ \gamma_{11}(k) \quad \gamma_{21}(k) \quad \gamma_{22}(k) \quad \gamma_{31}(k) \quad \cdots \quad \gamma_{LL}(k)\ ]$,

$X^T = [\ v_{11} \quad v_{21} \quad v_{22} \quad v_{31} \quad \cdots \quad v_{LL}\ ]$, X is to be estimated.

2.2.2 Least Squares Estimation by SVD

The dimension of X is large and the PE condition may not be satisfied, thus least squares estimation using SVD is employed in this section. Over a time range of $t_1 < t < t_N$, the data samples are collected at time instances $t_1, \cdots, t_i, \cdots, t_N$. With N samples, Eq. (3.4) can be produced and posed in the following matrix form

$$AX \quad = \quad Y \tag{2.4}$$

where $A = [\ A_1^T \quad A_2^T \quad \cdots \quad A_N^T\ ]^T$, $Y = [\ f(1) \quad f(2) \quad \cdots \quad f(N)\ ]^T$, X and Y belongs to normed linear spaces, and A is a matrix mapping X to Y. If $M = A^T A$ is non-singular, the least squares estimation of μ is unique and given by [41]

$$\hat{X} = M^{-1} A^T Y \tag{2.5}$$

where $\hat{X}$ is the estimation of X.

If $A^T A$ is singular, there will be infinite solutions. To identify the Preisach parameters, detailed discretization is needed. If the discretization level L is 60, the sampling time is 120s and the sampling interval is 1ms, the dimension of matrix A is 120000×1830 and it is difficult to compute $A^T A$. Thus, iterations are employed to compute M and $A^T Y$.

First, to allow the least squares solution, Eq. (2.6) is formed.

$$(A_1^T A_1 + A_2^T A_2 + \cdots + A_N^T A_N)X = A_1^T f(1) + A_2^T f(2) + \cdots + A_N^T f(N) \tag{2.6}$$

The iterations to compute M and $A^T Y$ are shown as follows

$$\begin{cases} M^{(k)} = M^{(k-1)} + A_k^T A_k \\ (A^T Y)^{(k)} = (A^T Y)^{(k-1)} + A_k^T f(k) \end{cases} \tag{2.7}$$

where $k = 1, 2, \cdots, N$. $M^{(k)}$ is the matrix M at time k, $M^{(0)} = 0$, and $Y_A^{(0)} = 0$ If $A^T A$ is singular or significantly ill-conditioned, the PE condition is not satisfied which is likely to occur in this application of Preisach identification. In this case, The SVD approach is used to obtain the pseudo-inverse. The SVD of $A^T A$ is given by

$$M = U \Sigma V \tag{2.8}$$

where $U = [\ u_1 \quad u_2 \quad \cdots \quad u_n\ ]$, $V = [\ v_1 \quad v_2 \quad \cdots \quad v_n\ ]$, $\Sigma = \mathrm{diag}([\sigma_1, \sigma_2, \cdots, \sigma_n])$, singular values $\sigma_1 \geq \sigma_2 \geq \cdots \geq \sigma_n$, U and V are unitary matrices.

Assume the rank of matrix M is k, then $\sigma_{k+1}, \sigma_{k+2}, \cdots, \sigma_n = 0$. If $\sigma_j/\sigma_1 \ll 1$, $j = r+1, r+2, \cdots, k$, M is ill-conditioned and can be decomposed as follows

$$M = \sum_{1}^{r} \sigma_i u_i v_i^T + \sum_{r+1}^{k} \sigma_i u_i v_i^T. \tag{2.9}$$

Small singular values can be truncated to yield improved least squares estimation in an ill-conditioned situation. The approximation of the pseudo inverse of A can be given by

$$A^+ \approx V_r \Sigma_r^{-1} U_r^T A^T \tag{2.10}$$

where A^+ denotes the pseudo inverse of A and $\Sigma_r^{-1} = \text{diag}\ [\ 1/\sigma_1 \quad 1/\sigma_2 \quad \cdots \quad 1/\sigma_r\ ]$.

The pseudo inverse of A is reformulated as

$$A^+ \approx \sum_1^r \frac{1}{\sigma_i} v_i u_i^T A^T. \tag{2.11}$$

Finally, the estimation of X in least squares sense is given by

$$\hat{X} = A^+ Y \tag{2.12}$$

where $\hat{X}$ is the estimation of X.

2.2.3 Identification Revision Using SVD Updating

In this section, the Preisach identification in (2.12) is revised using SVD updating, since Preisach estimation by SVD in least squares sense is time-consuming. The initial identified result is used and the density values are revised according to new data. Bunch and Nielsen provided some methods of SVD revision and updating [47]. Brand applied a rank-1 modifications to movie recommender systems [48]. In this section, the identification revision is based on the initial values A_0 and Y_0 in above section. For A_0 and Y_0, the following equation exists.

$$A_0 X = Y_0. \tag{2.13}$$

When a new vector a_1 and scalar output y_1 are added to the matrix, the following equation is achieved.

$$\begin{bmatrix} A_0 \\ a_1 \end{bmatrix}^T \begin{bmatrix} A_0 \\ a_1 \end{bmatrix} X = \begin{bmatrix} A_0 \\ a_1 \end{bmatrix}^T \begin{bmatrix} Y_0 \\ y_1 \end{bmatrix} \tag{2.14}$$

where Y_0 is a vector, y_1 is a scalar.

Let M_0 and M_1 denote $A_0^T A_0$ and $A_0^T A_0 + a_1^T 1_1$, respectively. Using the analysis in Section 2.2.2, the initial estimation is written as $M_0 = U_r \Sigma_r V_r^T + \varepsilon_r$, ε_r is the residual error. Then, M_1 can be written as

$$M_1 = U_r \Sigma_r V_r^T + a_1^T a_1 + \varepsilon_r. \tag{2.15}$$

Neglecting ε_r, M_1 can be reformulated as

$$M_1 \approx \begin{bmatrix} U_r & a_1 \end{bmatrix} \begin{bmatrix} \Sigma_r & 0 \\ 0 & I \end{bmatrix} \begin{bmatrix} V_r & a_1 \end{bmatrix}^T. \tag{2.16}$$

The components of a_1 orthogonal to the space spanned by U_r and V_r are given by

$$\begin{cases} p = a_1 - U_r U_r^T a_1 \\ q = a_1 - V_r V_r^T a_1 \end{cases}. \tag{2.17}$$

Let $R_U = \|p\|$ and $R_V = \|q\|$, then the unit vector u_p and v_q can be written as

$$\begin{cases} u_p = p/R_U \\ v_q = q/R_V \end{cases}. \tag{2.18}$$

According to the method provided by Ref. [48], $\begin{bmatrix} U_r & a_1 \end{bmatrix}$ and $\begin{bmatrix} V_r & a_1 \end{bmatrix}$ can be written as

$$\begin{bmatrix} U_r & a_1 \end{bmatrix} = \begin{bmatrix} U_r & u_p \end{bmatrix} \begin{bmatrix} I & U_r^T a_1 \\ 0 & R_U \end{bmatrix}. \tag{2.19}$$

$$\begin{bmatrix} V_r & a_1 \end{bmatrix} = \begin{bmatrix} V_r & v_q \end{bmatrix} \begin{bmatrix} I & V_r^T a_1 \\ 0 & R_V \end{bmatrix}. \tag{2.20}$$

Then M_1 can be written as

$$M_1 = \begin{bmatrix} U_r & u_p \end{bmatrix} K \begin{bmatrix} V_r & v_q \end{bmatrix}^T \tag{2.21}$$

where $K = \begin{bmatrix} I & U_r^T a_1 \\ 0 & R_U \end{bmatrix} \begin{bmatrix} \Sigma_r & 0 \\ 0 & I \end{bmatrix} \begin{bmatrix} I & V_r^T a_1 \\ 0 & R_V \end{bmatrix}^T$.

The SVD of M_1 is transformed to the SVD of K which is $(r+1) \times (r+1)$, as is shown in Eq. (2.22). The SVD of the small matrix K can save computing time, compared to the SVD of the large matrix M_1.

$$K = U_K \Sigma_K V_K^T \tag{2.22}$$

where $U_K^T U_K = I$ and $V_K^T V_K = I$

Then, the approximation SVD of M_1 can be achieved as

$$M_1 = \left(\begin{bmatrix} U_r & u_p \end{bmatrix} U_K \right) \Sigma_K \left(\begin{bmatrix} V_r & v_q \end{bmatrix} V_K \right)^T. \tag{2.23}$$

Let U_1 be the $1:r$ columns of $[\ U_r \quad u_p\ ]U_K$, V_1 be the $1:r$ columns of $[\ V_r \quad v_q\ ]V_K$, $\Sigma_1 = \Sigma_K(1:r, 1:r)$. The SVD updating with the fixed rank r is obtained as

$$M_1 = U_1 \Sigma_1 V_1^T. \tag{2.24}$$

Finally, the estimation revision of X is given by

$$\hat{X} = V_1 \Sigma_1^{-1} U_1^T A^T Y \tag{2.25}$$

where $\widehat{X}$ denotes the estimation of X.

2.2.4 Simulation Study of Proposed Identification Approach

This section presents the simulation study of the proposed hysteresis identification and its revision using SVD. Additionally, a measure of the estimation error of the Preisach

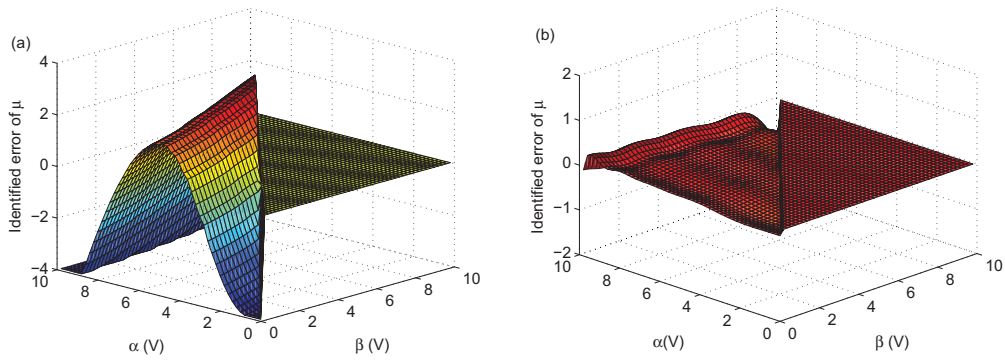

Figure 2.2: Estimated error of density function. (a): Projection algorithm. (b): SVD-based least squares.

density is defined as

$$\begin{cases} \|\mu - \hat{\mu}\| = \sqrt{\sum_{j=1}^{L} \sum_{i=1}^{j} (\mu_{ij} - \hat{\mu}_{ij})^2} \\ \|\mu\| = \sqrt{\sum_{j=1}^{L} \sum_{i=1}^{j} \mu_{ij}^2} \end{cases} \tag{2.26}$$

where $\hat{\mu}$ is the estimation of μ and can be directly computed using $\hat{X}$ and s_{ij}.

For comparison, the parameter vector X is also estimated using the projection algorithm in [41].

$$\hat{X}_k = \hat{X}_{k-1} - \gamma_L \frac{(\hat{f}(k) - f(k-1))A_{k-1}}{\theta + A_{k-1}^T A_{k-1}} \tag{2.27}$$

where $0 < \gamma_L < 1$, $\theta > 0$ and $\hat{X}_k$ is the estimation of X at the time instant k.

Let $\alpha_{\max} = 10$, $\alpha_{\min} = 0$, $\beta_{\max} = 10$, $\beta_{\min} = 0$, $\mu(\alpha, \beta) = 4$, $L = 50$. A sinusoidal input signal $10\sin(5t)$ is used. Moreover, the white noise with RMS of 0.01μm is added to the measurement. The sampling interval is 0.001s and the number of sampling points is 4000. Fig. 2.2(a) shows the estimated error using the projection algorithm. The estimated error $\|\mu - \hat{\mu}\|$ is 128.3, and the relative error $\|\mu - \hat{\mu}\|/\|\mu\|$ is 91.6%. The parameter identification error of the projection algorithm is significant. Fig. 2.2(b) shows the estimated error using the SVD-based identification.

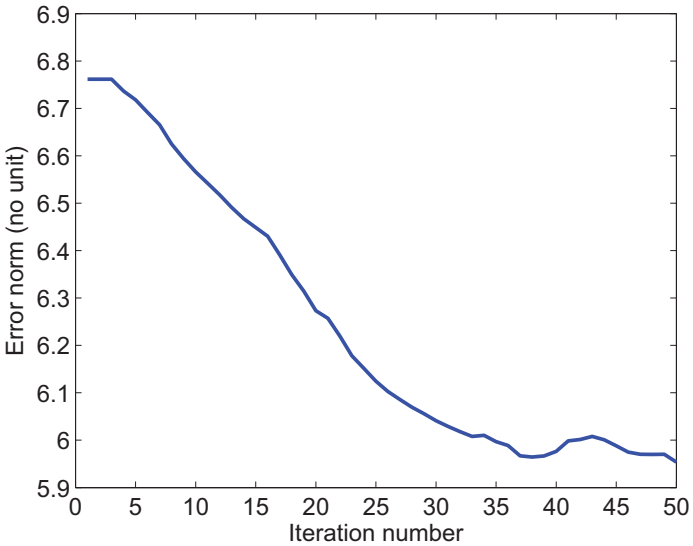

Figure 2.3: Converge error of SVD updating.

The dimension of A is 4000×1275, and we can get the determinant $\det(M) = 0$. The rank of M is 99. Then, r is set to 64 with $\sigma_{r+1}/\sigma_1 = 0.001$, the estimation error $\|\mu - \hat{\mu}\|$ and relative error $\|\mu - \hat{\mu}\|/\|\mu\|$ of the SVD-based identification are reduced to 6.67 and 4.7%, respectively. The difference between the real and estimated $\mu(\alpha, \beta)$ is small.

Finally, with SVD updating using 50 new points, the estimation error $\|\mu - \hat{\mu}\|$ is reduced from 6.67 to 5.9, as shown in Fig. 2.3. It can be seen that the SVD updating improves the estimation performance. The SVD-based approach gives better identification of Preisach hysteresis. The relative strengths of the identification approach when applied for this purpose will be investigated and highlighted through experimental studies.

2.3 Compensation Strategy of Preisach Hysteresis

2.3.1 Preisach-based Inversion Compensation

This section presents a Preisach-based inversion to compensate the hysteresis in PAs. The Preisach-based inversion is rate-independent because of the rate-independence of Preisach model [33], which simplifies the hysteresis compensation. The model-based inversion can be computed off-line based on the identified Preisach model and the reference trajectories.

First, with the models obtained via the possible approaches presented in Section 2.2, a hysteresis compensator based on these models can be designed. Fig. 2.4 shows the flow chart of Preisach-based inversion compensator. At time instant k, define the reference displacement as $x_r(k)$, the estimated hysteresis output as $\hat{f}(k)$, and the control action as $u_{ff}(k)$. The feedforward compensator works to obtain $u_{ff}(k+1)$ based on the identified Preisach hysteresis $\hat{H}$. Fig. 2.5 shows the Preisach-based inversion feedforward controller. x_r, d and u_{ff} denote the reference trajectory, the output disturbance and the feedforward control signal, respectively. From the reference trajectory and its memory curve, the feedforward compensator will compute the feedforward control signal based on the identified density function, and enforce the output of the PA to track the desired trajectory, thereby compensating the effects of the hysteresis.

In the flow chart, e is the tracking error bound, Δ is the iteration step and given as

$$\Delta = \lambda \frac{u_{\max}}{L} \tag{2.28}$$

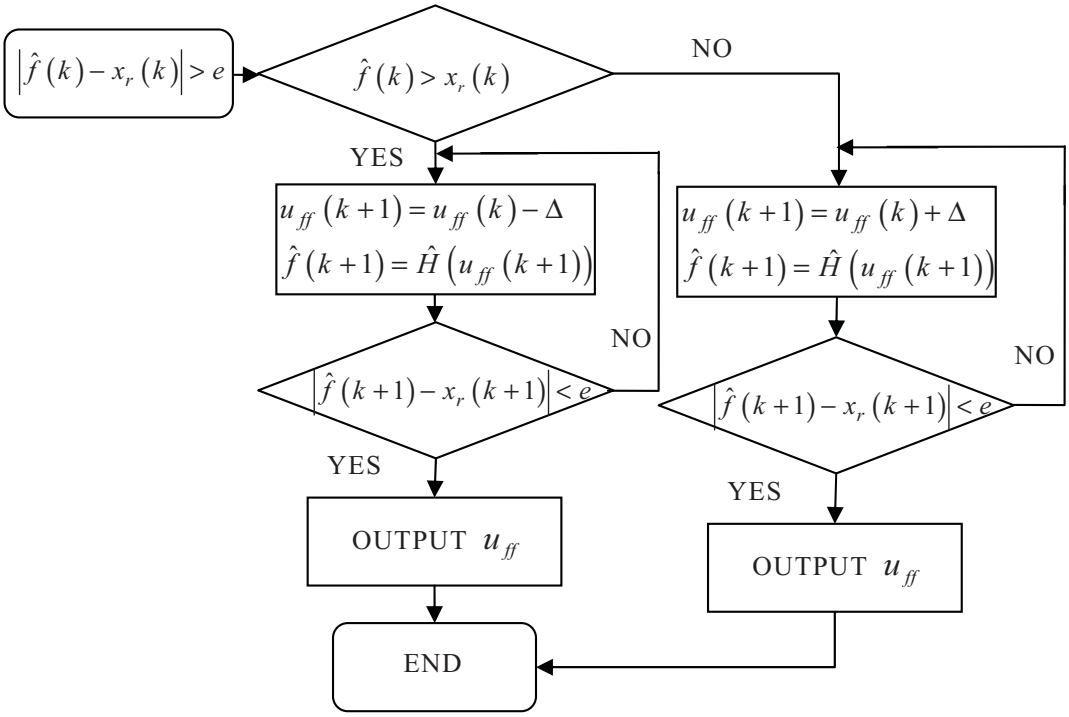

Figure 2.4: Flow chart of Preisach-based inversion compensator.

where λ is the factor to regulate the step which is less than 1, and L is the discretization level of the Preisach plane.

2.3.2 Proposed Composite Control Strategy

In this section, a composite controller comprises a Preisach-based inversion feedforward controller and a PID feedback controller. The Preisach-based feedforward can be used to compensate the static hysteresis in PAs, but commonly there are offset and disturbances in real-time control of PAs, thus, a feedback controller is also necessary. At low frequencies, the feedback controller eliminates the residual errors and disturbances. As the reference frequency increases, the feedback controller also suppresses the dynamic effects. The feedback controller design is not the key issue in this chapter. Thus, a PID controller is employed.

The techniques of the PID controller and its tuning are mature. Theoretical analysis, such as stability analysis, and experimental tests of PID controllers have been applied in piezo systems [37, 49], but the tracking performance is still limited due to the hysteresis effect. Based on accurate identification of hysteresis, this chapter uses the Preisach-based inversion feedforward to enhance the tracking performance. Fig. 2.5(b) shows the composite control of the PAs. u_{fb} denotes the feedback control signal. The measurement noise is also considered.

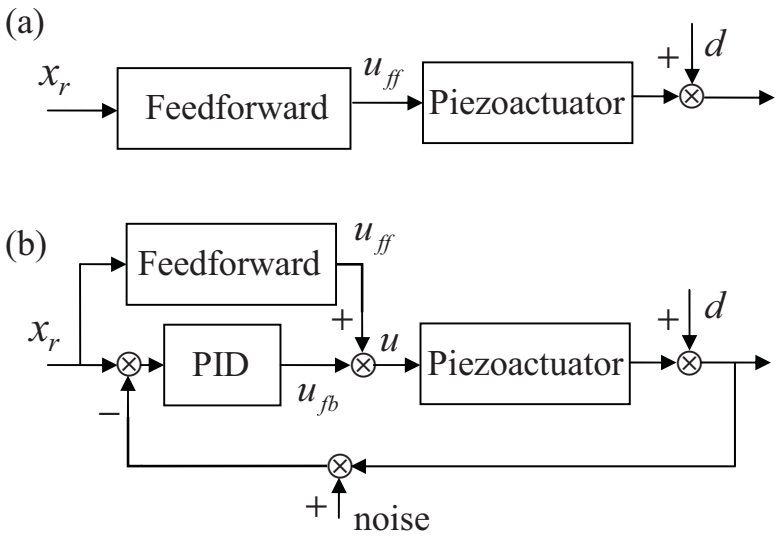

Figure 2.5: (a): Feedforward control. (b): Composite control.

2.3.3 Simulation Study of Proposed Compensation Strategy

The proposed compensation strategy is simulated in this section. The Preisach hysteresis and the estimated results in the Section 2.2.4 are used. Moreover, the output disturbance of 5μm is also added to the system. The reference signal is given as $20(1 - \cos 2\pi t)$. The performance of Preisach-based inversion feedforward is shown in Fig. 2.6(a). The RMS tracking error is $5.02\mu m$. However, the output disturbance is not suppressed by

the feedforward controller. Conversely, the RMS tracking error is reduced to $0.22\mu m$ with the proposed composite controller while the proportional and integral gains of the PID controller are set to 0.001 and 3, respectively. The constant disturbance is also suppressed, as shown in Fig. 2.6(b).

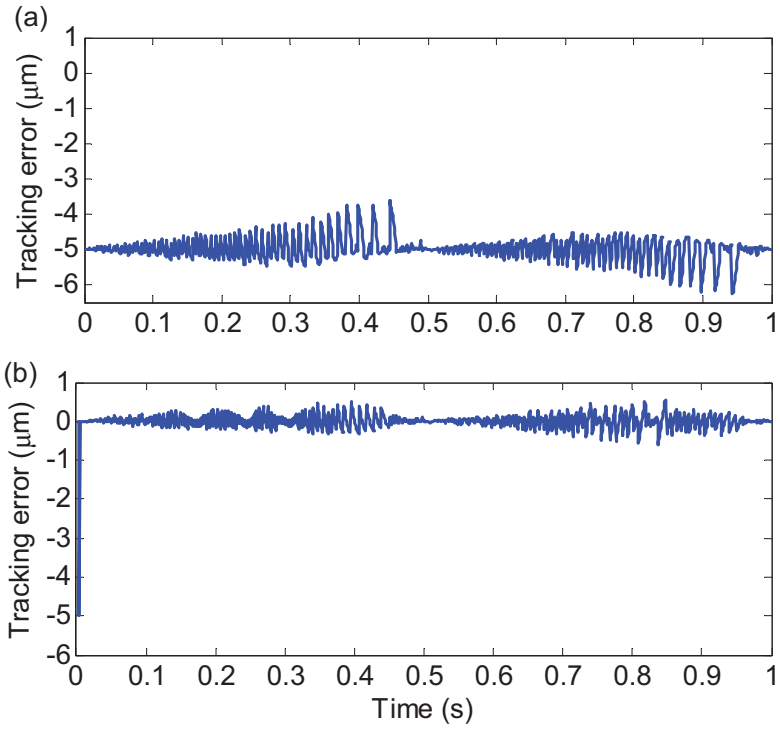

Figure 2.6: Tracking errors. (a): Preisach-based Inversion feedforward control. (b): Composite control.

2.4 Experimental Studies

This section presents the experimental studies of the proposed identification and compensation approaches. First, to validate the SVD-based least squares estimation of Preisach hysteresis, the Preisach density function is identified at low frequencies where the piezo displacement can be regarded as the hysteresis output. The proposed hysteresis compensation strategy is also verified. Section 2.4.1 proposes the experimental study of the

Preisach hysteresis identification. Section 2.4.2 provides the Preisach-based inversion feedforward and the composite control at low frequencies. To extend the application of the identified Preisach hysteresis. Section 2.4.3 presents the proposed composite control at high frequencies where the hysteresis output is not measurable due to the dynamics effect. The Preisach-based inversion feedforward is computed according to the reference trajectory and identified Preisach model.

2.4.1 Hysteresis Identification at Low Frequencies

The hysteresis identification of the piezoelectric stage is finished at frequencies lower than 1Hz. The Preisach model is still used to represent the quasi-static hysteresis. At low frequencies, the hysteresis of a PA is quasi-static [26], since the vibration and electric dynamics approach to a DC gain [50]. Therefore, the low frequency piezo displacement without drift can be regarded as the hysteresis output [51]. To avoid the high frequency dynamics, the Preisach hysteresis of the piezoelectric stage is identified using smooth input voltage at low frequencies such that the quasi-static assumption holds. The input voltage range is set to [0, 60]V, i.e., the parameters $\alpha_{\min} = 0$, $\beta_{\max} = 60$, $\beta_{\min} = 0$, $\beta_{\max} = 60$. The input signal is constructed as follows:

$$u(t) = \left\lfloor 1 + \frac{t - 120\lfloor t/120 \rfloor}{2} \right\rfloor \frac{1 - \cos \pi t}{2} \tag{2.29}$$

where $\lfloor \cdot \rfloor$ is the $floor$ function which rounds elements to their negative integers.

Moreover, the sampling interval is set to 1ms. 120000 points are sampled. Using the iterative method in Eq. (2.7), the matrix $M = A^T A$ and $A^T Y$ are achieved. Fig. 2.7(a)

shows the singular values of matrix M. The max singular value is 2.541×10^7 and the non-zero minimum singular value is 0.734. The condition number of M is 3.462×10^7. Thus, the matrix M is significantly ill-conditioned. The singular values that are less than 2.5 are truncated. Fig. 2.7(b) shows the corresponding identification result of the Preisach density function. The identified density values are positive and its inversion is easy to achieve.

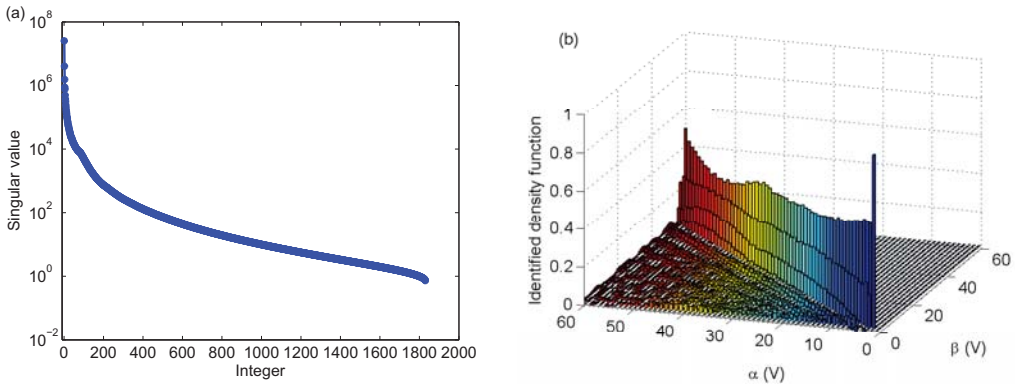

Figure 2.7: (a): Singular values. (b): Identified density function.

Two methods are used to test the soundness of the identified hysteresis. First, this section presents the comparison of hysteresis curves according to the measured and simulated data. Then, the Preisach-based inversion feedforward in Section 2.3.1 is used to test the identification soundness, since the model-based inversion is sensitive to modeling error. Fig. 2.8(a) shows the measured and simulated hysteresis curves at 1Hz. The two curves are close to each other. Fig. 2.8(b) shows the curve of the actual piezo displacement versus the desired displacement at 1 Hz. The hysteresis curve is significantly reduced. Thus, the hysteresis identification is satisfactory.

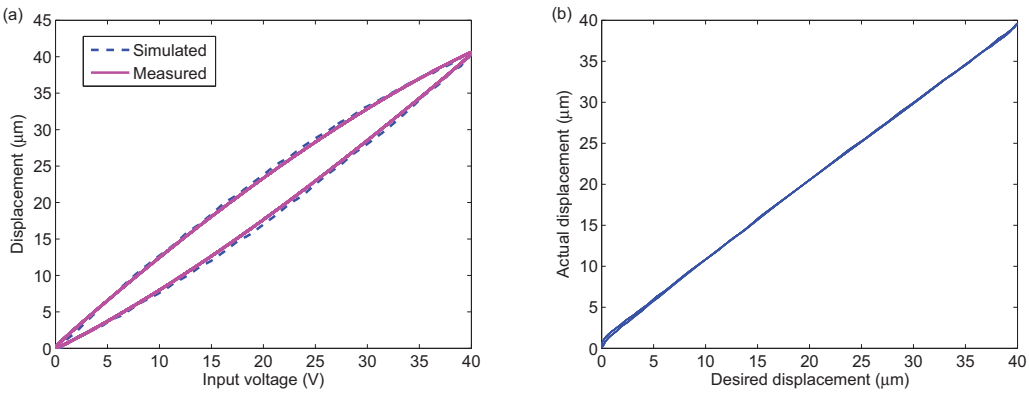

Figure 2.8: Validation of hysteresis identification. (a): Comparison of the measured and simulated hysteresis curves at 1Hz. (b): Actual displacement versus desired displacement at 1Hz.

2.4.2 Performance of Proposed Composite Controller at Low Frequencies

In this section, the proposed composite control strategy is validated at low frequencies where the piezo output can be regarded as the hysteresis output. The inverse Preisach feedforward is given in Fig. 2.4. Moreover, the parameters are $\lambda = 0.1$, e=0.2, $L = 60$ and $u_{\max} = 60$V. Eq. (2.30) shows the harmonic reference trajectory x_{r1} with a large amplitude.

$$x_{r1} = 20(1 + \sin 2\pi t) \tag{2.30}$$

Additionally, the PID feedback controller is designed using Ziegler-Nichols rules. A relay is employed to obtain the ultimate gain and ultimate period. Applying the tuning method, the PID controller K_{fb} is given by

$$K_{fb} = 0.6K_p(1 + \frac{2}{T_i s} + \frac{T_i}{8}\frac{s}{\epsilon s + 1}) \tag{2.31}$$

where the ultimate gain K_p is 2.62, the ultimate period T_i is $0.002s$, ϵ is a small positive

value to reduce the bandwidth of the derivative, and ϵ is set to 0.005.

To test whether the PID controller in Eq. (2.31) achieves its limit, the K_p is increased. When the PID gain K_p is increased by 8%, significant chattering arises and the tracking performance worsens. It indicates that the PID controller achieves its limit.

To measure the tracking performance, the percent root-mean-square (RMS) error e_{rms} as a percentage of the output range is defined as [25]

$$e_{\text{rms}}(\%) = \left(\frac{\sqrt{\frac{1}{n}\sum_{i=1}^{n}(x_r(i) - y(i))^2}}{\max(x_r) - \min(x_r)} \right) \times 100\%, \tag{2.32}$$

where n is the number of samplings, $x_r(i)$ and $y(i)$ are the reference and the measured piezo displacement at the time instant i.

Figs. 2.9(a-b) shows the tracking error and the feedforward control signal of the Preisach-based inversion feedforward controller. The RMS tracking error is 2.431μm, the offset is 2.1μm, e_{rms} is 6.08%. It indicates that the inverse Preisach feedforward controller is effective to compensate the Preisach hysteresis, but the feedforward controller cannot reject disturbances and suppress modeling errors. Fig. 2.9(c) shows the tracking performance of the PID controller in (2.31). The RMS tracking is 0.061μm, and e_{rms} is 0.15%. The PID controller is effective to track low frequency trajectories, but its performance is still limited by the Preisach hysteresis.

Fig. 2.10 shows the tracking performance of the proposed composite controller. The RMS tracking error is reduced to 0.014μm, the offset disturbance is also suppressed, and e_{rms} is 0.035%. The tracking error is reduced by 76.7%, compared to the PID controller in (2.31). The composite controller gives the best performance.

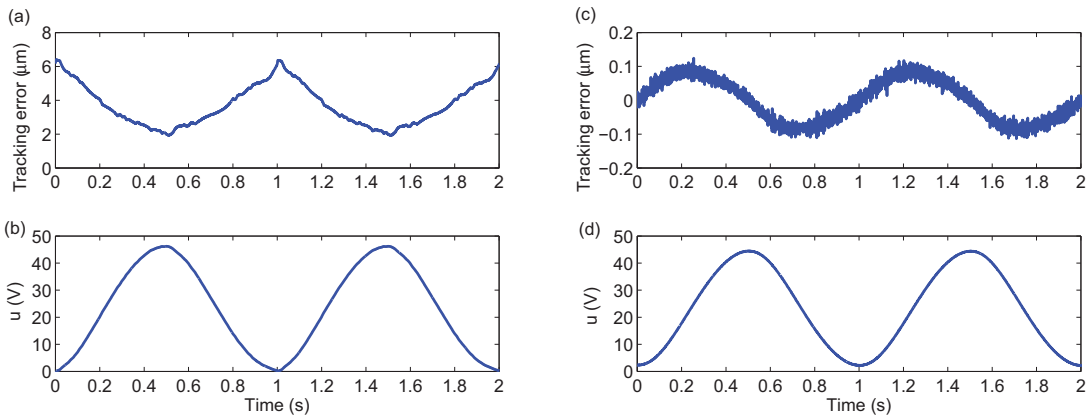

Figure 2.9: Experimental results of the feedforward controller and the PID controller. (a): Tracking error of the inversion feedforward controller. (b): Feedforward control signal. (c): Tracking error of the PID controller. (d): PID feedback control signal.

The feedback control signal u_{fb} of the composite controller, as shown in Fig. 2.10(b), is less than 12% of the PID control signal in Fig. 2.9(d). The feedforward control signal of the inversion feedforward controller and the composite controller are the same. The control signals in Figs. 2.9(b), 2.9(d) and 2.10(b) indicate that the Preisach-based feedforward eliminates the hysteresis and the PID feedback controller suppresses the disturbances and residual errors.

2.4.3 Performance of Proposed Composite Controller at Higher Frequencies

In this section, the proposed composite controller is employed to track high frequency trajectories. Though the Preisach hysteresis is identified at low frequencies, the Preisach model in (2.1) is rate-independent. Thus, the Preisach-based inversion feedforward still holds at high frequencies. As the input frequency increases, the dynamic effects also increases.

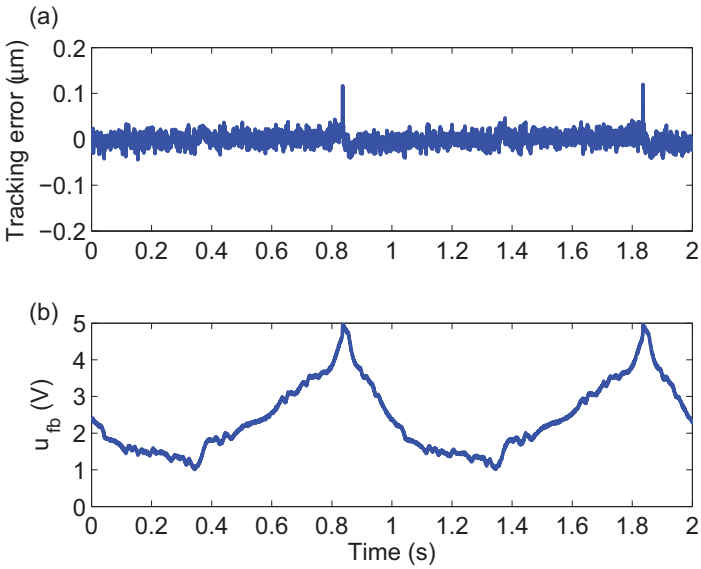

Figure 2.10: Experimental results of the proposed composite controller. (a): Tracking error. (b): Feedback control signal u_{fb} of the composite controller.

The piezo displacement is not the hysteresis output due to the dynamic effects, but the hysteresis in the PA also can be modeled using the rate-independent Preisach model in (2.1). The hysteresis is still compensated through the reference trajectories and the identified μ in Section 2.4.1.

The harmonic trajectory at 25Hz is shown in Eq. (2.33). According to the rate-independence of Preisach hysteresis, the feedforward control signal of x_{r2} can be achieved by altering the time scale of the feedforward control signal of x_{r1}.

$$x_{r2}(t) = 20(1 + \sin 50\pi t). \tag{2.33}$$

At first, the same PID tuning controller in Eq. (2.31) is applied to the piezoelectric stage. Figs. 2.11(a-b) shows the tracking error and the control signal of the PID controller. The tracking error is significant, the RMS value is $1.187\mu m$, and e_{rms} is 3%.

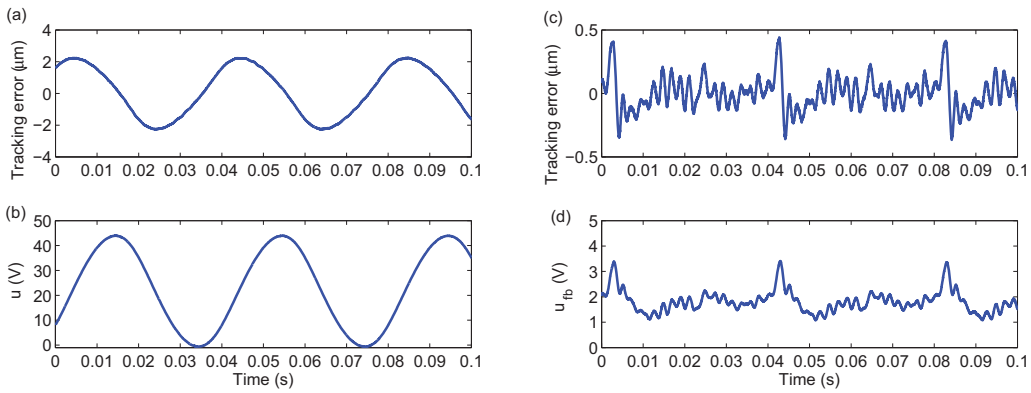

Figure 2.11: Experimental results of the PID controller and the composite controller. (a): Tracking error of the PID controller. (b): PID feedback control signal. (c): Tracking error of the composite controller. (d): Feedback control signal u_{fb} of the composite controller.

Finally, the composite controller is implemented. Fig. 2.11(c) shows the tracking error using the proposed composite controller, the RMS tracking error is 0.123μm and e_{rms} is 0.31%. e_{rms} is reduced by 89% compared to the PID controller. The composite controller gives the best tracking performance among the Preisach-based inversion feedforward controller, the PID controller and the composite controller.

Fig. 2.12 shows the curves of the actual displacement versus the desired displacement under the inversion feedforward, the PID controller and the composite controller, respectively. The proposed composite controller achieves the smallest hysteresis curve, meaning the piezo tracks the displacement with the smallest delay and error.

2.5 Discussion

To achieve accurate motion control of PA mechanisms, this chapter presents the identification and compensation of Preisach hysteresis. The SVD-based algorithm is able to deal with an ill-conditioned mathematical issue due to the large number of discretized param-

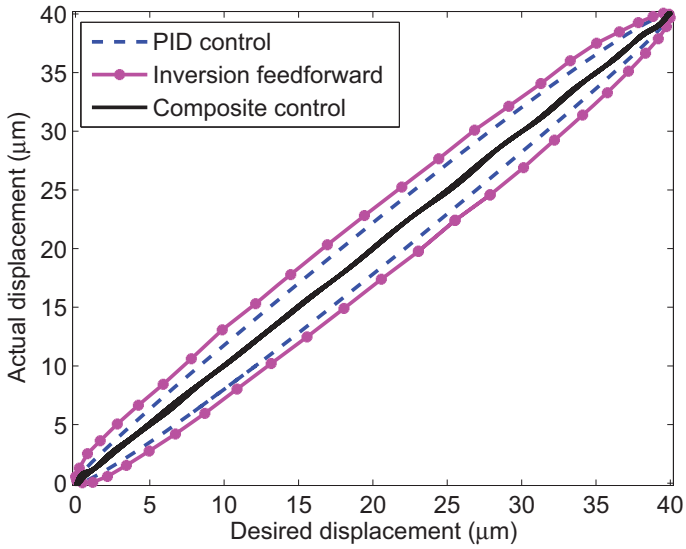

Figure 2.12: Actual versus desired displacement with the PID controller (dashed), the Preisach-based inversion feedforward controller (solid-dotted) and the composite controller (solid), respectively.

eters on hand and it can thus achieve more accurate estimation, but it requires a higher level of computational infrastructure for an online implementation to be viable. SVD-based parameter updating is employed to revise least squares estimation with higher computing efficiency, and this approach improves the estimation performance.

The experimental results validate the soundness of Preisach hysteresis identification using the Preisach-based inversion feedforward. With the identified parameters and a log of the memory curve, a Preisach-based feedforward compensator is constructed which is complemented with a PID feedback controller. If only the inversion feedforward controller is used, the residual error and the dynamic effect due to vibration dynamics are not eliminated. If only the PID controller is used, the tracking performance of the PID controller is degraded due to the hysteresis effect. As the reference frequency increases, the tracking performance of the PID controller is degraded more significantly because of

vibration effects. The composite controller still has adequate tracking performance as the reference frequency increases to 25Hz, where the Preisach-based feedforward controller and the PID feedback controller can compensate the hysteresis and dynamics effect, respectively. In the experiment of the piezoelectric stage, accurate motion control is achieved by the proposed composite controller. The e_{rms} at 1Hz and 25Hz are 0.035% and 0.31%, respectively.

2.6 Conclusion

Based on the Preisach model, the identification and compensation of hysteretic phenomenon in PAs are addressed in this chapter. The SVD-based least squares estimation and revision are adopted for the identification of these parameters. The Preisach-based inversion feedforward is developed to compensate the hysteresis in PAs. Additionally, a PID feedback controller is also augmented to suppress residual errors, disturbances and dynamics effects. Experimental studies have been done to highlight the relative strengths of these algorithms with a view towards real-time precise control tracking applications.

In summary, the hysteresis of PAs has been investigated at low frequencies in this chapter. For further investigation, in Chapter 3, the vibration and electric dynamics at high frequencies will also be identified. Additionally, a model-based composite controller will be designed and demonstrated.

Chapter 3

Model-based Composite Control for High-Bandwidth and Precision Scanning of PAs

3.1 Introduction

High-bandwidth and precision scanning are required in scanning probe microscopes (SPMs) for high-speed imaging and high-speed nanofabrication. However, the hysteretic dynamics in PAs greatly limits the scanning and tracking performance. In the open loop, the maximum error due to quasi-static hysteresis in PAs is 10%-15% of the travel range [24]. As the input frequency increases, PAs exhibit dynamic response and the error from the hysteretic dynamics becomes more significant. Generally, a high gain PID controller is adequate for scanning and tracking at low frequencies [52], but there is still a low gain margin due to the rapid phase-drop [53]. The closed loop bandwidth attained using a simple feedback controller is typically less than 5%-10% of the first resonant frequency because of complex hysteretic dynamics in PAs [54–56].

At high frequencies relative to the resonant frequencies, PAs exhibit dynamic and com-

plex hysteresis. Thus, the rate-independent hysteresis model should be replaced with a dynamic type. [57] presents a dynamic Preisach model to describe hysteresis at broadband frequencies, but the parameter identification process is complex and difficult. [58] and [59] expand the rate-independent Prandtl-Ishlinskii hysteresis to a rate-dependent type, and density functions are assumed for parameter identification. Instead of expanding rate-independent hysteresis, the cascade connection of the rate-independent hysteresis and non-hysteretic dynamics is another approach to represent dynamic hysteresis over a broad range of frequencies [39]. We employ the cascaded model comprising the rate-independent Preisach hysteresis, electric and vibration dynamics to represent the hysteretic dynamics of PAs at broadband frequencies.

To push the application frontier of PAs towards fine scanning, various feedback control schemes have been investigated [45, 60]. For instance, [39] proposes the adaptive identification and control of hysteretic systems. [61] and [62] employ a bounded uncertainty to represent the PA hysteresis, and propose a sliding mode controller and a robust adaptive controller to enhance tracking performance. [63] presents the Prandtl-Ishlinskii hysteresis based sliding model controller. However, fine and high-speed scanning is not simultaneously achieved with such approaches, since the hysteretic dynamics is not adequately compensated over a broad range of frequencies. Furthermore, feedback controllers have limited bandwidth. Alternatively, a model-based inversion feedforward controller can be employed to increase the scanning bandwidth and improve the scanning performance simultaneously, which relies on accurate model identification.

To achieve scanning at a rate higher than the first resonant frequency, this chapter proposes a composite controller consisting of a model-based inversion feedforward controller and a PI feedback controller. To design the composite controller, the PA model is identified first. The quasi-static hysteresis is identified using harmonic signals with varying amplitudes. The persistently exciting (PE) condition is satisfied with the harmonic input signals. Following this, the non-hysteretic dynamics is identified using a multi-frequency harmonic input. Then, the composite controller is constructed based on the identified model. The inversion feedforward controller strictly depends on the hysteretic model and can be computed off-line. The feedforward controller effectively expands the scanning bandwidth. To reject disturbances, the PI feedback controller is employed. The proposed composite controller presents simultaneous high-speed and precision scanning of PAs.

This chapter is organized as follows. Section 3.2 presents the model identification strategy of PAs. Section 3.3 proposes the composite control strategy for high-speed and precision scanning. Then, Section 3.4 presents the experimental study of the identification and composite control on a piezoelectric stage. Finally, Section 3.5 concludes the chapter.

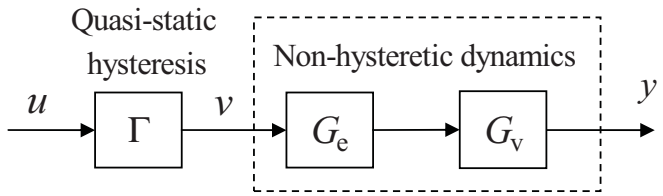

Figure 3.1: Block diagram of PA model.

3.2 Proposed Model Identification Strategy

3.2.1 Model of PA systems

The cascade connection is employed to represent the hysteretic dynamics in PA systems. Fig. 3.1 illustrates the cascade structure. Γ, G_{e} and G_{v} denote the quasi-static hysteresis, electric and vibration dynamics, respectively. The non-hysteretic dynamics consists of G_{e} and G_{v}, which are assumed to be time invariant. u, v and y represent the input voltage, hysteresis output and piezo displacement, respectively. Furthermore, the hysteresis output v is unmeasurable.

The quasi-static hysteresis is rewritten as the following rate-independent Preisach model [29].

$$v(t) = \iint_S \mu(\alpha, \beta)\gamma_{\alpha\beta}[u(t)]d\alpha d\beta \tag{3.1}$$

where S is the Preisach area, $\mu(\alpha, \beta)$ is the density function, and $\gamma_{\alpha\beta}$ is the hysteron output at point (α, β).

In this chapter, both the electric dynamics G_{e} and the vibration dynamics G_{v} are considered. Thus, the non-hysteretic dynamics $G = G_{\mathrm{e}}G_{\mathrm{v}}$ can be written as

$$G = \frac{k_{ev}}{\tau s + 1} \cdot \frac{\prod_j^{n-2}(s^2 + 2\xi_j\omega_j s + \omega_j^2)}{\prod_i^{n}(s^2 + 2\xi_i\omega_i s + \omega_i^2)} \tag{3.2}$$

where τ is the time constant of electric dynamics, ω_i and ω_j are the mode frequencies of vibration dynamics, ξ_i and ξ_j are the damping ratio, and k_{ev} is the DC gain of the non-hysteretic dynamics G.

The dynamics of PAs is quasi-static and almost rate-independent at low frequencies, since the vibration and other high frequency dynamics approach their DC gains at low frequencies [65]. Thus, the key idea behind the proposed approach is to identify the Preisach hysteresis using low frequency harmonic signals. Then, the hysteresis effects can be computed using the estimated Preisach model. Thereafter, the non-hysteretic dynamics is identified.

3.2.2 Identification of Quasi-static Hysteresis

The identification of quasi-static hysteresis essentially entails the identification of the density function of the Preisach model (3.1). Based on the investigation in Chapter 2, the identification of quasi-static hysteretic will be further studied in this section. The discretization method is also used for the ease of hysteresis identification. The hysteresis output in (3.1) at the time instant k can be represented as

$$v(k) = A_k X \tag{3.3}$$

where $A_k = [\gamma_{11}(k), \gamma_{21}(k), \cdots, \gamma_{L1}(k), \cdots, \gamma_{LL}(k)]$,

$X = [\mu_{11}s_{11}, \mu_{21}s_{21}, \cdots, \mu_{L1}s_{L1}, \cdots, \mu_{LL}s_{LL}]$, L is the discretization level of the Preisach plane, γ_{ij}, μ_{ij} and s_{ij} are the hysteron output, the density value and the area of grid (i, j), respectively.

The identification of $\mu_{i,j}$ is equivalent to the estimation of $\mu_{ij}s_{ij}$, since s_{ij} is known. The data samples are collected at the time instants $t_1, t_2, \cdots, t_i, \cdots, t_N$, and a linear equation for Preisach hysteresis identification can be written as

$$AX = b \tag{3.4}$$

where $A^{\mathrm{T}} = \left[A_1^{\mathrm{T}}, A_2^{\mathrm{T}}, \cdots, A_N^{\mathrm{T}}\right]$, $b^{\mathrm{T}} = [v(1), v(2), \cdots, v(N)]$.

The least squares method is employed to estimate X. However, the PE problem is associated with a large number of parameters. This PE condition is mathematically equivalent to the singularity of $A^{\mathrm{T}}A$. Furthermore, the ill-condition due to small singular values of $A^{\mathrm{T}}A$ also has to be suppressed, and the SVD-based estimation is employed, as shown in Appendix. The estimation of X in the least squares sense is given by

$$\hat{X} = A^{+}b \tag{3.5}$$

where A^{+} is the pseudo-inverse of matrix A. To perform the identification of quasi-static hysteresis, the low frequency harmonic signal with varying amplitudes is proposed to eliminate the PE condition and solve equation (3.4) in least squares sense. Also, a sampling method that is uniform in the magnitudes of input voltages is also proposed.

For the ease of identification, the variant input voltage is given in (3.6), whose amplitudes match the discretization of the Preisach plane.

$$u(t) = (P(t) - 0.5\delta)\,\frac{1 - \cos\omega_s t}{2} \tag{3.6}$$

where $\delta = \max(u(t))/L$, ω_s is angular frequency, $(P(t) - 0.5\delta)$ is the amplitude at time

t and $P(t)$ is given by

$$P(t) = \left\lfloor 1 + \left(t - T_{\mathrm{P}} \left\lfloor \frac{t}{T_{\mathrm{P}}} \right\rfloor \right) \frac{\omega_s}{2\pi} \right\rfloor \delta \tag{3.7}$$

where T_{P} is the period of $P(t)$, and $\lfloor \cdot \rfloor$ is the *floor* function that rounds the elements to the nearest integers in the direction of negative infinity.

The relationship between T_{P} and ω_s can be represented as

$$T_{\mathrm{P}} = L\omega_s \tag{3.8}$$

The Preisach model (3.1) is not rate-dependent but path-dependent. Thus, the sampling for identification is not uniform with respect to (w.r.t.) time but uniform w.r.t. the input voltage $u(t)$. This sampling method is proven to be more effective in the experiment in Section 3.4.1.

The sampling instants of the ith harmonic signal are given by

$$t_{i,j} = \frac{1}{\omega_s} \arccos \left[1 - \frac{2(j - 0.5\delta)\delta}{P(t)} \right] + t_{i,1} \tag{3.9}$$

$$t_{i,2i-j} = \frac{1}{\omega_s} \left\{ 2\pi - \arccos \left[1 - \frac{2(j - 0.5\delta)\delta}{P(t) - 0.5} \right] \right\} + t_{i,1} \tag{3.10}$$

where $t_{i,1}$ is the starting time of the ith harmonic signal, $i = 1, 2, \cdots, P(t)/\delta$, $j = 1, 2, \cdots, i$, and $P(t) - 0.5\delta$ is the amplitude of the ith harmonic signal determined by equation (3.7).

Remark 3.1. *Adequate amplitudes are required to identify the Preisach hysteresis in Eq. 3.3. Furthermore, the sampling is uniform w.r.t. the input signal due to the rate-independence but path-dependence of Preisach hysteresis.*

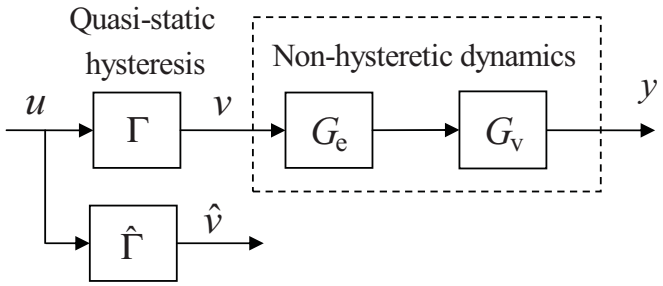

Figure 3.2: Output estimation of quasi-static hysteresis

The identification of the electric and vibration dynamics is performed at high frequencies. A multi-frequency harmonic input is employed for adequate frequencies. The hysteresis output is estimated by the identified Preisach model. Fig. 3.2 illustrates the estimation of the hysteresis output according to the identified Preisach model. $\hat{\Gamma}$ and $\hat{v}$ denote the identified Preisach model and the estimated hysteresis output, respectively. The identification of the electric and vibration dynamics is performed using $\hat{v}$ and y. Mature identification methods can be employed in this part. For instance, ARMAX method can be employed for parameter identification where the model structure is specified according to equation (3.2).

3.3 Proposed Composite Controller

This section presents the design of the composite controller. The structure of the control system is shown in Fig. 3.3. r denotes the reference trajectory, u_{ff} and u_{fb} denote the feedforward and feedback control signals, respectively, $\hat{G}^{-1}$ and $\hat{\Gamma}^{-1}$ denote the estimated of the non-hysteresis dynamics and the hysteresis nonlinearity, respectively. The composite controller consists of a primary model-based inversion feedforward controller and

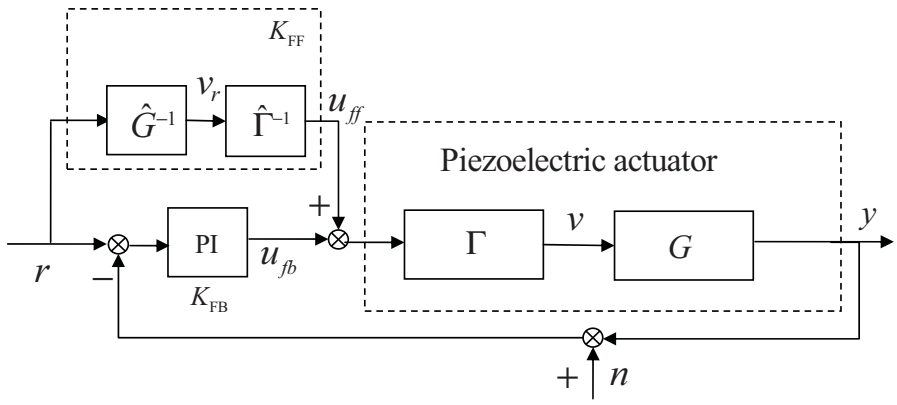

Figure 3.3: Composite control strategy

a secondary PI feedback controller. The feedforward controller is used to reduce phase-lag and achieve high-speed scanning. It comprises of the inversions of the non-hysteretic dynamics and the Preisach hysteresis. The feedforward controller is constructed based on the hysteresis and non-hysteretic dynamics. The discrete PI controller is employed for feedback which compensates disturbances and reduces modeling uncertainty within the feedback bandwidth.

3.3.1 Analysis of Feedforward and Feedback Controllers at High Frequencies

A model-based inversion feedforward controller is suitable to track high-frequency trajectories, because the feedforward controller is not affected by the measurement noise which is outside of the feedforward control branch. In addition, the feedforward control signal approaches the inverse of the system gain. However, the feedforward controller is not capable of rejecting disturbances. Conversely, a feedback controller is capable of rejecting disturbances within the feedback control bandwidth, typically at low frequencies. Furthermore, the feedback gain at low frequencies can be set to a large value

due to non-significant measurement noise, but at high frequencies, it is inappropriate to perform a large gain feedback controller because of the possible chattering in case of noise.

The tracking error under the feedforward controller K_{FF} can be written as

$$\left.\frac{e}{r}\right|_{K_{\mathrm{FF}}} = 1 - (G \circ \Gamma)\, K_{\mathrm{FF}} \tag{3.11}$$

where $e = r - y$ is the tracking error, and $\circ$ denotes the composition operator which represents the relationship between G and Γ [33].

Under the model-based inversion feedforward controller, the feedforward control signal u_{ff} can be represented as

$$u_{ff} = r\left(\hat{\Gamma}^{-1} \circ \hat{G}^{-1}\right) \tag{3.12}$$

where $\hat{G}^{-1}$ and $\hat{\Gamma}^{-1}$ denote the inversion of the estimation of the non-hysteretic dynamics and the Preisach hysteresis.

The feedforward control signal is not affected by measurement noise, and depends on the inversion gain of the PA model. With perfect inversion feedforward control, i.e., the inversion is sufficiently accurate, the feedforward controller can give adequate tracking without considering disturbances.

Alternatively, the tracking error under the feedback controller K_{FB} can be written as

$$\left.\frac{e}{r}\right|_{K_{\mathrm{FB}}} = \frac{1}{1 + (G \circ \Gamma)\, K_{\mathrm{FB}}} \tag{3.13}$$

The tracking error under the feedback controller K_{FB} can be reduced adequately if the control gain can be set to sufficiently large. At low frequencies, it is common to

implement a feedback controller with a large integral action towards fine motion of PAs [60]. If the tracking error is suppressed by a factor of η, i.e., $e/r = 1/\eta$, the feedback control signal u_{fb} can be written as

$$u_{fb} = (n + r)(\eta - 1)\left(\Gamma^{-1} \circ G^{-1}\right) \tag{3.14}$$

where $\eta \gg 1$ for fine tracking, and n is broadband noise.

The feedback control signal u_{fb} in (3.14) indicates that high gains of the feedback controller at high frequencies easily result in instability due to the measurement noise n. Typically, the PA is a low pass filter and the system gain is decreased at high frequencies, but the model-based inversion $\Gamma^{-1} \circ G^{-1}$ is a high pass filter. Thus, if equation (3.14) with $\eta \gg 1$ at high frequencies, the feedback control signal easily approaches chattering and saturation when the amplified high frequency measurement noise coincides with the vibration modes of PAs.

Thus, we employ both the feedforward controller and the feedback controller to achieve high-speed and precision scanning. The feedforward controller will expand the scanning bandwidth and the feedback controller will reject disturbances.

Remark 3.2. *Model-based inversion feedforward controllers are suitable to expand tracking bandwidth and achieve high-speed scanning. Conversely, feedback controllers are suitable to reject unknown disturbances within the feedback bandwidth, and achieve precision scanning.*

3.3.2 Design of Feedforward Controller

In this section, the model-based inversion feedforward controller is constructed to achieve high-speed scanning. It encompasses the inverse non-hysteretic dynamics and the inverse hysteresis. The reference signals pass through the inverse non-hysteresis dynamics $\hat{G}^{-1}$, then the inverse hysteresis $\hat{\Gamma}^{-1}$. The inversion of the non-hysteretic dynamics has more zeros than poles and thus cannot be directly implemented for unknown and general reference signals in dSPACE board. To solve this problem, known and sufficiently smooth trajectories are employed. Furthermore, $\hat{v}_r$ can be computed off-line.

After obtaining the inversion of the non-hysteresis dynamics, its output v_r is regarded as the reference of hysteresis inversion $\hat{\Gamma}^{-1}$. The feedforward voltage u_{ff} is regulated such that the unmeasurable hysteresis output v tracks v_r. The regulation is achieved using the hysteresis inversion based on the identified Preisach model. If the estimated hysteresis output $\hat{v}$ tracks the reference within the error range e_r, the feedforward voltage u_{ff} remains the same. If the estimated hysteresis output $\hat{v}$ is less than the reference v_r and $|v_r - \hat{v}| > e_r$, the feedforward voltage u_{ff} is increased and vice versa. Algorithm 1 illustrates the hysteresis inversion. The unmeasurable hysteresis output $\hat{v}$ is estimated using the identified density function $\hat{\mu}$. Parameter m is the total number of iterations in each regulation.

The iteration step δ_h is represented as

$$\delta_h = \lambda u_{\max}/L' \tag{3.15}$$

Algorithm 1 Inversion of the identified Preisach hysteresis

```
if v_r(k) < v̂(k) then
    u_ff(k+1) = u_ff(k) − iδ_h,        i = 1, ··· , m
    v̂(k+1) = Γ̂(u_ff(k+1))
    if |v_r(k) − v̂(k+1)| ≤ e_r then
        break
    end if
else
    if v_r(k) > v̂(k) then
        u_ff(k+1) = u_ff(k) + iδ_h, i = 1, ··· , m
        v̂(k+1) = Γ̂(u_ff(k+1))
        if |v_r(k) − v̂(k+1)| ≤ e_r then
            break
        end if
    else
        u_ff(k+1) = u_ff(k)
    end if
end if
```

where λ is a coefficient to regulate the step, $u_{\max}$ is the maximum input voltage used in the hysteresis identification, and L' is the new discretization level.

3.3.3 Design of Feedback Controller

Though robust control and high gain control have been commonly studied to compensate the hysteresis and vibration dynamics of PA, they are complex and are not suitable to track trajectories faster than the resonant frequencies. The high-speed scanning performance will be achieved primarily by the model-based inversion feedforward controller. However, a feedback controller is also necessary to maintain stability and robustness in the face of disturbances and modeling errors. For disturbance rejection, a simple PI controller is designed according to the identified hysteretic dynamics. The more complex computations required for the hysteretic dynamics compensation is left outside of the feedback loop.

In Chapter 2, the traditional tuning method has been used to obtain a PID controller for feedback control. In this Chapter, the PID tuning considering hysteretic dynamics will be investigated. Additionally, to reduce the sensitivity to high frequency measurement noise, the derivative action is not used. Alternatively, the compensation performance at high frequencies is achieved by using the model-based inversion feedforward control.

The identified model of PAs is used to compute the ultimate gain and the ultimate period. Ziegler-Nichols (Z-N) tuning rules can be used to obtain the parameters of the PI controller. First, the ultimate gain and period are computed using the identified non-hysteretic dynamics. Then, the ultimate gain is adjusted according to the identified Preisach model, while the ultimate period is kept unchanged as it is not affected by the Preisach hysteresis.

Characteristic of PID Tuning in PAs

PAs have both rate-independent hysteresis and non-hysteresis dynamics. The hysteresis is represented by the Preisach model (3.1) which is static and path-dependent. The static hysteresis does not exhibit dynamic responses, but will alter the input gain. Conversely, the electric and vibration dynamics exhibit dynamic responses. Thus, the PID tuning methods using step response or relay tuning will result in the uncertainty of ultimate gain in PAs. The gain uncertainty w.r.t. input voltage $u(t)$ due to Preisach hysteresis is illustrated in Fig. 3.4. $S^{\max}$ is the activated area corresponding to the maximum gain for $u(t)$. Conversely, $S^{\min}$ is the area corresponding to the minimum gain for $u(t)$.

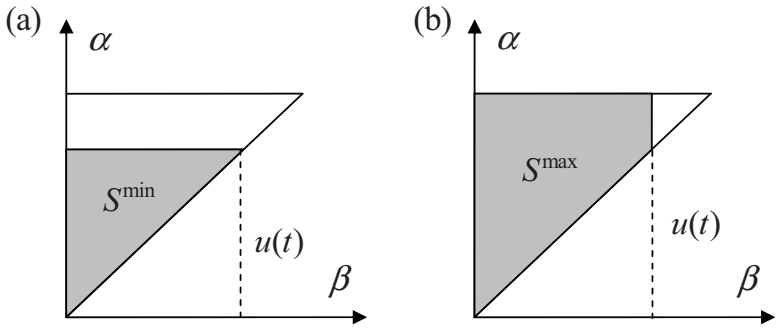

Figure 3.4: Illustration of the uncertain gain due to Preisach hysteresis. (a): Minimum gain. (b): Maximum gain.

The minimum and maximum gains of the input voltage $u(t)$ due to Preisach hysteresis are represented as

$$\begin{cases} \Delta_{\max} = \iint\limits_{S^{\max}} \mu(\alpha,\beta)\gamma_{\alpha\beta}[u(t)]d\alpha d\beta/u(t) \\ \Delta_{\min} = \iint\limits_{S^{\min}} \mu(\alpha,\beta)\gamma_{\alpha\beta}[u(t)]d\alpha d\beta/u(t) \end{cases} \tag{3.16}$$

where $\Delta_{\min}$ and $\Delta_{\max}$ denote the minimum and maximum gains due to the Preisach hysteresis.

Thus, the gain uncertainty Δ_h due to the Preisach hysteresis can be represented as

$$\Delta_{\min} \leq \Delta_h \leq \Delta_{\max} \tag{3.17}$$

Ultimate Gain and Period

At first, the ultimate period p_u and the gain margin g_m are determined at the cross frequency ω_c of the non-hysteretic dynamics G

$$p_u = \frac{1}{\omega_c} \tag{3.18}$$

where ω_c is the cross frequency on the order of hertz.

The gain margin g_m of the non-hysteretic dynamics at the cross frequency ω_c is given

by

$$g_m = \frac{1}{|G(j\omega_c)|}$$

where $G(j\omega_c)$ is the gain of the non-hysteretic dynamics at the cross frequency ω_c.

Then, the overall ultimate gain k_u is obtained through the gain margin g_m and the uncertainty $\Delta_{\max}$.

$$k_u = \frac{g_m}{\Delta_{\max}} \tag{3.19}$$

Finally, the PI controller determined by Z-N tuning rules can be represented as

$$K_{\mathrm{PI}}(z) = 0.6k_u(1 + \frac{2}{p_u}\frac{T}{2}\frac{z+1}{z-1}) \tag{3.20}$$

where T is the sampling interval, k_u and p_u are the ultimate gain and ultimate period, respectively.

Remark 3.3. *The hysteresis effect alters the ultimate gain of the PI controller determined by Z-N tuning rules. The ultimate gain can be modified by the identified Preisach hysteresis.*

3.4 Experimental Studies

3.4.1 Identification of Quasi-static Hysteresis

The piezoelectric hysteresis is quasi-static at low frequencies, and low frequency harmonic signals are used to identify the rate-independent Preisach hysteresis. In equations (3.6)-(3.10), $u_{\max} = 60$ V, $L = 60$, $\delta = 1$, $\omega_s = 0.6$ Hz, and $T_{\mathrm{P}} = 100$s are used for the input voltage and the sampling in hysteresis identification.

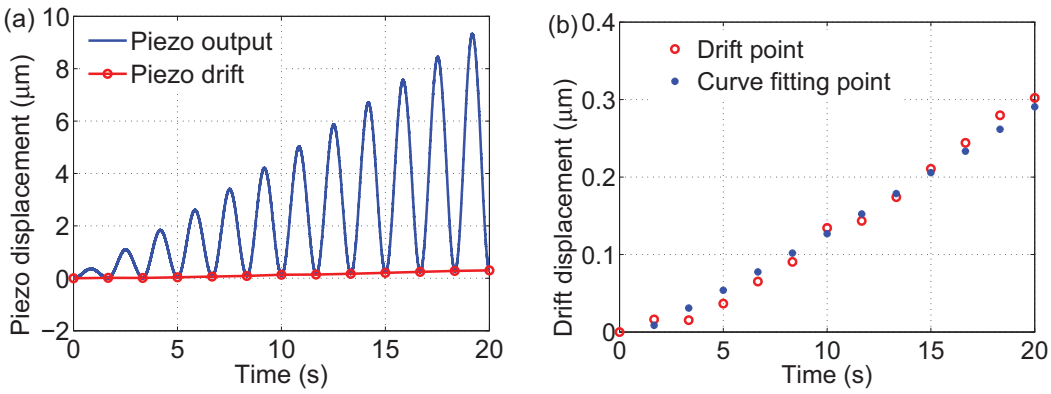

Figure 3.5: (a): Displacement drift. (b): Drift suppression.

Drift Suppression

There exist displacement drift in the piezoelectric stage. Fig. 3.5 (a) shows the drift effect in the piezo displacement till 20s. In this experiment, 100 sampling points are used and the sampling time is the starting time $t_{i,1}$ of the ith harmonic signal. The polynomial curve fitting is employed to suppress the drift. MATLAB function `polyfit` is used, and the polynomial for the drift suppression is given by

$$y_d(t) = 0.000121t^2 + 0.0127t - 0.013 \tag{3.21}$$

where $y_d(t)$ is the drift displacement, and t is the time. Fig. 3.5 (b) shows the drift suppression performance using the curve fitting approach. The curve fitting gives satisfactory accuracy.

Preisach Hysteresis Identification

The discretization level L of Preisach plane is set to 60. Then, the dimension of $A^{\mathrm{T}}A$ is 1830×1830. In each grid (i, j), the density at the central point is regarded as the density of grid (i, j). To reduce the computing time, only the points determined (3.9)

and (3.10) are used. Extremes of the input signal are still preserved, thus preserving the hysteresis memory.

In hysteresis identification, only 3661 points are sampled. The rank of $A^{\mathrm{T}}A$ is 1830. Thus, the PE condition is eliminated. Fig. 3.6 (a) shows the singular values of $A^{\mathrm{T}}A$. The condition number of $A^{\mathrm{T}}A$ is 1.92×10^7, which indicates $A^{\mathrm{T}}A$ is ill-conditioned and small singular values should be truncated.

The singular value selection is a tradeoff problem. A larger truncation threshold increases the matrix approximation error but suppresses the ill-conditioned problem. Conversely, a smaller truncation threshold decreases the matrix approximation error but results in a more serious ill-conditioned problem. In this chapter, the truncation is implemented according to the error analysis of hysteresis identification. The relative error between the estimated displacement error and the measured displacement is employed to describe the hysteresis identification accuracy, because the density function μ is unknown.

The relative error is given by

$$e_{\mathrm{h}}(\%) = \frac{\|y - \hat{y}\|}{\|y\|} \tag{3.22}$$

where y and $\hat{y}$ are the measured and estimated displacements. With trials, the singular values smaller than 1.2 are truncated to suppress the ill-condition problem. Equation (3.5) is employed to identify the density function. Fig. 3.6(b) shows the identified density function. The relative error in (3.22) is less than 3%, and the Preisach hysteresis identification is satisfactory.

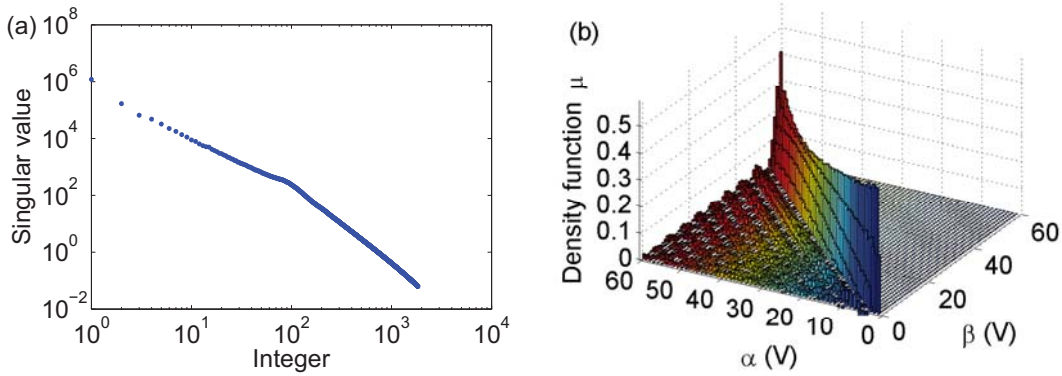

Figure 3.6: (a): Singular values of $A^{\mathrm{T}}A$. (b): The identified density function

3.4.2 Identification of Non-hysteresic Dynamics

The non-hysteretic dynamics is identified using a multi-frequency input. The output $\hat{v}$ of the quasi-static hysteresis is computed using the identified Preisach model. First, to choose the input frequency, a relay feedback is used to estimate the ultimate frequency of the piezoelectric stage. Fig. 3.7 shows the sketch of relay feedback where the relay output switches between 0 and 10 V. From the experiment, the estimated ultimate frequency is 500Hz. The harmonic signal with adequate frequencies is required to excite more modes. In the experiment, two vibration modes are identified. According to the estimated ultimate frequency, the multi-frequency input signal consisting of six sinusoids is given by

$$u_{\mathrm{d}}(t) = a_0 + \sum_{i=1}^{6} a_i \sin 2\pi f_i t$$

where $a_0 = 24$, $a_1 = 3$, $a_2 = 6$, $a_3 \sim a_6 = 3$, $f_1 = 100$Hz, $f_2 = 200$Hz, $f_3 = 300$Hz, $f_4 = 400$Hz, $f_5 = 500$Hz, and $f_6 = 600Hz$.

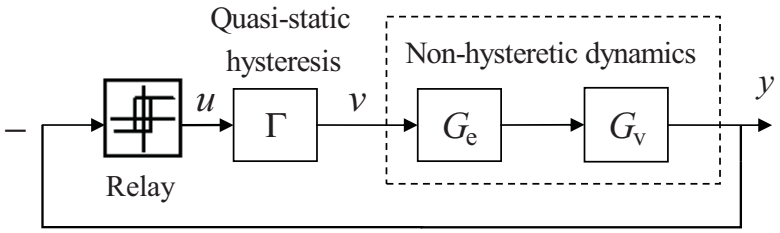

Figure 3.7: Ultimate frequency estimation using relay feedback.

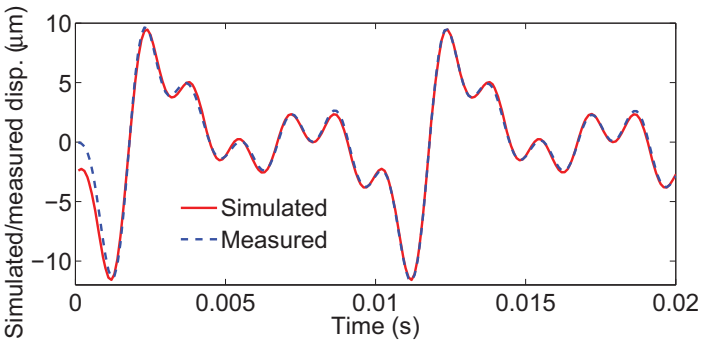

Figure 3.8: Comparison of simulated and measured displacement.

To estimate the hysteresis output accurately, the Preisach plane is rediscretized to be 180×180, i.e., $L' = 180$. The estimated hysteresis output $\hat{v}$ based on the identified Preisach model is regarded as the input to the non-hysteretic dynamics.

The non-hysteretic dynamics is identified using the ARMAX method [64] where the denominator, the numerator and the error are identified with orders of 5, 1, 5, respectively. The estimated parameters of the non-hysteretic dynamics are $\hat{k}_{\text{ev}} = 0.8716$, $\hat{\tau} = 0.000474$s, $\hat{\omega}_1 = 453.5$Hz, $\hat{\omega}_2 = 792.7$Hz, $\hat{\xi}_1 = 0.67$, and $\hat{\xi}_2 = 0.081$, respectively. Fig. 3.8 shows the comparison of the simulated and measured displacements with zero mean value. It can be seen that the simulated displacement accurately matches the measured displacement.

Remark 3.4. *The detailed discretization gives more smooth and precise estimation of the hysteresis output. In the experiments, the discretization level is 60 for the hysteresis identification, but the discretization level is 180 for the hysteresis estimation.*

3.4.3 Controller Design

For easy application, harmonic signals are used as the scanning trajectories. The proposed composite controller is designed and implemented in the dSPACE board 1104. The composite controller consists of a mode-based inversion feedforward controller and a PI feedback controller. Based on the identified Preisach hysteresis in Section 3.4.1 and the non-hysteretic dynamics in Section 3.4.2, the mode-based inversion feedforward is constructed. λ, $u_{\max}$ and L' are set to 1, 60 and 180 in Algorithm 1, respectively.

In order to suppress disturbances, the simple PI feedback controller in Section 3.3.3 is augmented. Based on the identified non-hysteretic model of the piezoelectric stage, the ultimate period is 0.0018s. The maximum gain $\Delta_{\max}$ due to Preisach hysteresis is 1.06. The ultimate gain k_u is 1.65. Finally, the following discrete PI controller is given by

$$K_{\mathrm{PI}}(z) = \frac{1.01z - 0.976}{z - 1} \tag{3.23}$$

where the sampling interval is 0.025ms.

3.4.4 Performance Evaluation

Proposed Feedforward Controller

The proposed model-based inversion feedforward controller is employed to reduce the phase-lag and gain distortion. Furthermore, the feedforward controller can also be employed to validate the soundness of the model identification. Based on the identified hysteresis and non-hysteretic dynamics, the proposed model-based inversion feedforward controller is implemented in the piezoelectric stage. For comparison, open loop control is also considered and it only employs a positive value to regulate the actual-desired displacement gain to one. The positive gain 2.22 is used at 600Hz, such that the actual and the desired displacements have the same amplitude.

Fig. 3.9 (a) shows the curve of the actual and the desired displacements under the model-based inversion feedforward controller. Compared to the open loop response, the phase-lag and the magnitude distortion are reduced significantly by the model-based inversion feedforward controller. The effectiveness of the model-based inversion feedforward controller also validates the soundness of the model identification.

Fig. 3.9 (b) shows the scanning error at 600Hz. The root-mean-square (RMS) scanning error of the open loop control is 18.7 μm. The RMS scanning error of the model-based inversion feedforward is 13.54μm, and it is reduced by 27.5%. Fig. 3.9(a) also shows the offset and drift under the inversion feedforward controller. The offset is 13.5 μm and the maximum drift range is 1.1μm, which will be suppressed using the PI feedback controller.

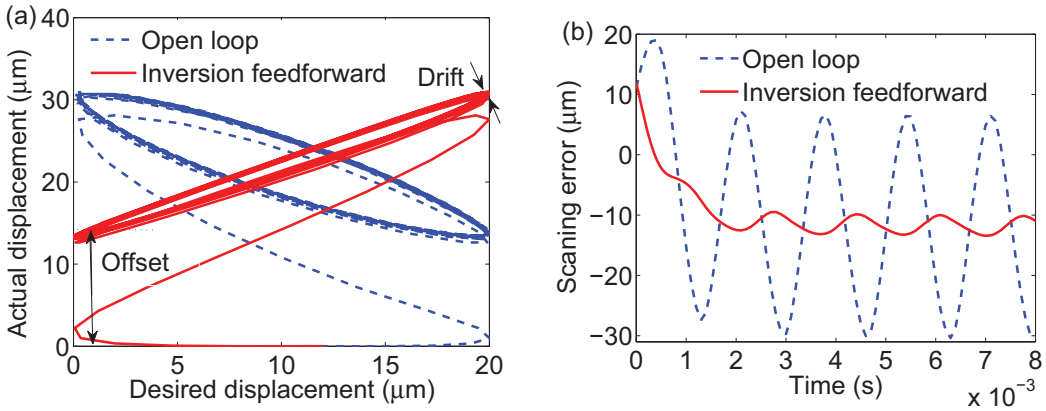

Figure 3.9: Performance of the model-based inversion feedforward controller

Proposed Composite Controller

The proposed composite controller is implemented. Moreover, the RMS error e_{rms} as a percentage of the output range is defined as [25]

$$e_{\text{rms}}(\%) = \left(\frac{\sqrt{\frac{1}{p}\sum_{i=1}^{p}\left(y_r(i) - y(i)\right)^2}}{\max\left(y_r\right) - \min\left(y_r\right)} \right) \times 100\% \tag{3.24}$$

where p is the number of sampling points, $y_r(i)$ and $y(i)$ are the desired and actual displacements at time instant i, respectively.

Figs. 3.10 (a1-a3) show the curves of the actual versus the desired displacements with the above three different controllers at 40Hz, 100Hz and 600Hz, respectively. Figs. 3.10 (b1-b3) and Table 3.1 show the corresponding scanning performances at 40Hz, 100Hz and 600Hz, respectively.

The proposed composite controller achieves both high-speed and precision scanning. Compared with the open loop case, the PI controller improves the scanning performance, but the phase-lag and scanning error of the PI controller also increases significantly as the scanning frequency increases. Thus, the PI controller has limited scanning bandwidth

Table 3.1: Scanning errors RMS (μm) and e_{rms} (%)

Frequency	Open-loop	PI control	Composite control
40Hz	5.144 (12.9%)	2.526 (6.31%)	0.30 (0.75%)
100Hz	11.616 (29.1%)	6.218 (15.6%)	0.484 (1.21%)
600Hz	14.961 (74.8 %)	8.014(40.1%)	0.352 (1.76%)

and performance at frequencies higher than the first resonant frequency.

The composite controller presents the best performance. Both the phase-lag and the scanning error are reduced significantly. Compared with the PI controller, the scanning errors are reduced by 88.1%, 75.5% and 79.7% at frequencies 40Hz, 100Hz, and 600Hz, respectively. Specially, fine scanning performance is achieved by the composite controller. The RMS scanning error at 600Hz is 0.352μm and e_{rms} is 1.76%.

Remark 3.5. *The model-based inversion feedforward controller is successful to expand the scanning bandwidth higher than the resonant frequency of the PA. Furthermore, the PI feedback controller is successful to reject known disturbances within the feedback bandwidth.*

3.4.5 Discussion

The experimental results confirm that the proposed composite controller provides both high-speed and precision scanning at a rate higher than the resonant frequency. By applying the proposed composite controller, the scanning error e_{rms} is reduced to be 0.30%, 1.21%, 1.76% of the desired amplitudes at the scanning frequencies 40Hz, 100Hz, 600Hz (8.84%, 22.1%, 132.0% of the first resonant frequency), respectively.

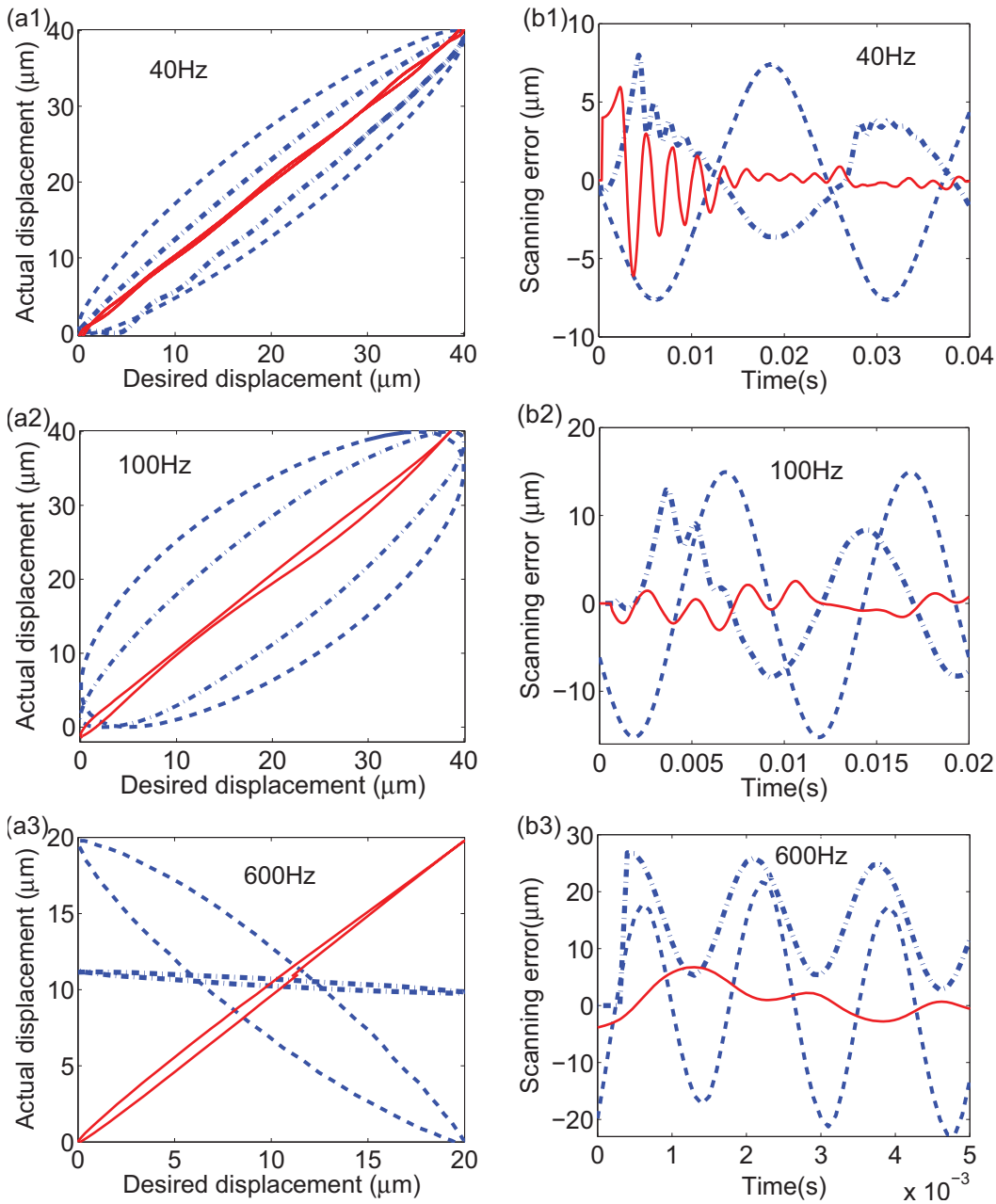

Figure 3.10: Scanning performance at different frequencies under open loop control (dashed), PI control (dash-dotted), and composite control (solid). (a1)-(a3): Curves of the actual displacement versus the desired displacement. (b1)-(b3): Scanning error.

Table 3.2: Comparison of scanning frequency and relative scanning error (%)

	Ref. [65]	Ref. [25]	Proposed method
Resonant frequency	800Hz	486Hz	453.5Hz
Scanning frequency	300Hz	450Hz	600Hz
Relative RMS error (%)	5.28%	10.25%	1.76%

Currently, in most published works to the best of the authors' knowledge, the scanning frequency with satisfactory performance is lower than the resonant frequency. For instance, Wu presented the robust inversion-based 2-DOF control for the PA with a resonant frequency of 800Hz [65], but the electric dynamics and hysteresis is not modeled. The scanning error e_{rms} for the small range (5μm) trajectory at 300Hz is 5.28%, as shown in Table 3.2. Results at higher scanning frequencies are not provided in the PA experiment [65]. Leang proposed the high-gain feedback and inverse feedforward control for the AFM piezoelectric actuator with a resonant frequency of 486Hz [25], as shown in Table 3.2, the scanning error e_{rms} at 450Hz is 10.15%, while results at higher scanning frequencies are still not provided.

In this chapter, the coupled hysteresis, electric and vibration dynamics of PAs are identified, and a simple composite controller is designed. The model identification strategy of PAs is effective, and the model-based feedforward controller is significant to expand the scanning bandwidth by reducing phase-lag and gain distortion. The satisfactory scanning performance can be achieved at frequencies higher than the resonant frequency of the piezoelectric stage.

3.5 Conclusion

This chapter presents an approach amenable to practical applications for dynamic hysteresis identification and high-speed motion control. The feedforward controller, employing a model-based inversion, greatly extends the control bandwidth, while the PI feedback controller suppresses disturbances. The identification methodology and the composite control scheme are fully implemented on a real piezoelectric stage using a dSPACE control platform. The proposed composite controller achieves precision scanning at a rate higher than the resonant frequency.

In summary, the hysteresis and the non-hysteresis dynamics have been identified separately in this chapter. To identify and compensate the hysteretic dynamics over a broad band range of frequencies, the comprehensive modeling and identification of PAs will be investigated in Chapter 4.

Chapter 4

Comprehensive Identification of Hysteretic Dynamics in PAs

4.1 Introduction

Piezoelectric actuator (PA) systems are widely employed in precision engineering, and the capability for precision tracking at broadband frequencies is increasingly appealing in many applications, such as the high-bandwidth nano-positioning of scanning probe microscopes (SPMs) and high-speed imaging of dynamic molecular processes [44, 66]. However, the performance of dynamic tracking is limited over a wide range of frequencies, because of the coupled hysteresis, creep and vibration dynamics [54, 60]. For example, the operating bandwidth of SPMs with fine tracking is lower than 1%−5% of the first resonant frequencies [53].

Various approaches have been proposed to improve the tracking performance of PAs [34, 44, 56]. At low frequencies, proportional-integral-derivative (PID) controller may be adequate to compensate the hysteresis and creep of PAs [44, 52, 67]. As the tracking frequency increases, model-based approaches become necessary to compensate the

hysteretic dynamics. A model-based inversion feedforward controller, which bases on an accurate modeling of PAs, is an effective approach to broaden the bandwidth and enhance the tracking performance. However, the hysteretic dynamics identification of PAs over a broad range of frequencies is still a main research issue for model-based feedforward compensation [44]. It is still difficult to accurately identify the parameters of PAs [30]. Thus, up-to-date various complex modeling and identification approaches have been investigated to achieve accurate model of PAs [51, 68–72]. At broadband frequencies, the effects due to hysteresis, creep, electric and vibration dynamics are significant and should be considered simultaneously.

At low frequencies, typically lower than 10Hz, hysteresis and creep are the main effects of PAs. Hysteresis is a strongly nonlinear element with global memories [73, 74]. At low frequencies, PAs can be approximately represented with a rate-independent hysteresis model, such as Preisach model and Prandtl-Ishlinskii (P-I) model, and the latter is a special case of the former. The classical Preisach model is employed to identify the static hysteresis of PAs and to track low frequency trajectories in [37]. The rate-independent Preisach hysteresis satisfies wiping out and congruency property [29], which will be used in this chapter for hysteresis identification.

Creep is slow dynamics and its modeling is not as mature as hysteresis. A non-hysteretic spring-damper model can be employed to represent creep dynamics [75]. Alternatively, [76] proposes a Preisach-type creep and hysteresis model at low frequencies, but the parameter identification is difficult when other non-hysteretic dynamics are also

considered. In this chapter, a non-hysteretic creep model is used to simplify the model identification.

As the input frequency increases, the electric and vibration dynamics become more dominant. Dynamic models can be employed for PAs. The second order vibration dynamics is used to represent and control the piezoelectric tube for fast scanning in [77]. However, the hysteresis and creep are not modeled. In [57], a Preisach model is proposed with a dynamic density function. The Preisach model is also used to compensate the hysteresis of piezoceramic mirrors [78]. Moreover, [79] proposes a generalized Preisach model without the limitation of congruency property. [59] regards the dynamic hysteresis of PAs as a rate-dependent P-I model. However, the identification of rate-dependent hysteresis model still relies on density function assumption and nonlinear curve fitting.

Alternatively, over broadband frequencies, the combination of rate-independent hysteresis and non-hysteretic dynamics can also be used to represent the PA dynamics. [39] presents a cascade connection of the Preisach hysteresis and the non-hysteretic dynamics without availability of intermediate. However, it is difficult to implement the identification because of the couplings among the hysteresis, creep, electric and vibration dynamics. Until now, the coupling between the hysteretic and non-hysteretic dynamics is not fully considered while identifying a PA model, and isolated treatments of these dynamics are reported in [80, 81].

Fig. 4.1 shows the dynamic hysteretic curves between the input voltage and the output displacement of the PA investigated in this chapter. The significant dynamic

hysteresis is observed. As the input frequency increases, the gain distortion and phase delay also increase. This indicates the rate-independent hysteresis model is not adequate to represent the hysteretic dynamics of PAs at broadband frequencies. The dynamic behavior of the PA also should be encompassed in the model if it is employed over a broad range of frequencies.

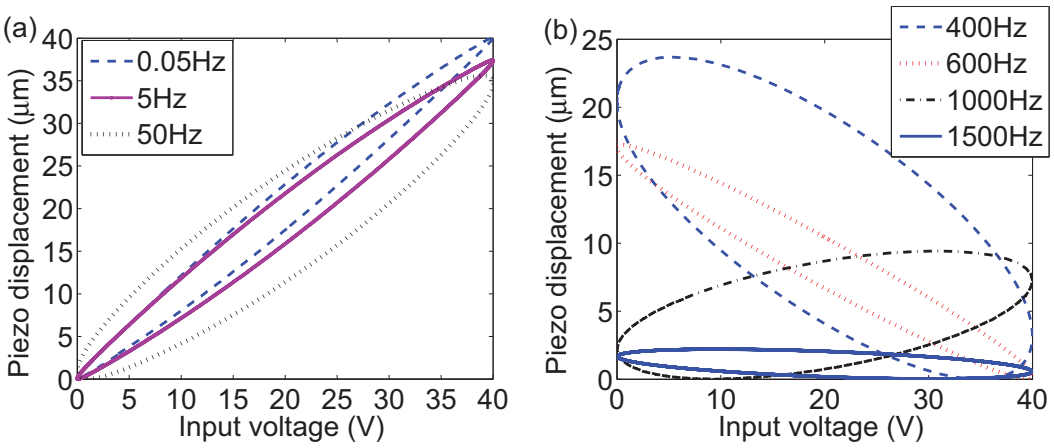

Figure 4.1: Input-output hysteretic curves of the piezoelectric stage at different frequencies. As the input frequencies increase, the dynamic response also increases significantly. Over broadband frequencies, the rate-independent or static hysteresis is not effective. Alternatively, the rate-independent hysteresis cascaded with the non-hysteretic dynamics can be used.

This chapter employs the cascade structure for modeling the hysteretic dynamics of PAs. The couplings among the hysteresis, creep, electric and vibration dynamics are fully considered and identified by leveraging on their special characteristics and distinction. First, the creep, electric and vibration dynamics are identified by employing square wave inputs. Then, the Preisach hysteresis is identified by employing amplitude-varying harmonic inputs and amplitude-dependent sampling rules. To validate the effectiveness of the hysteretic dynamics identification, this chapter employs the model-based inver-

sion feedforward control in addition to the comparison of the hysteretic curves of the simulated and measured displacements versus the input voltage.

The organization of this chapter is as follows. Section 4.2 provides the problem statement. Section 4.3 discusses the hysteretic behavior of Preisach model under square inputs. Section 4.4 proposes the input signals and the sampling law for hysteresis identification. Sections 4.5 and 4.6 propose the systematic identification approach and the simulation studies of the identification approach. Following by this, Section 4.7 presents the experimental studies and the demonstration of the proposed identification strategy. Finally, Section 4.8 concludes this chapter.

4.2 Comprehensive Modeling of PAs

To accurately and conveniently represent the hysteretic dynamics, we have investigated the multifield effect and dynamics of PAs in Section 4.1. Generally, a PA can be described as a capacitor with linear piezoelectric effect, but the linear relationship has very limited accuracy. As a result, the theoretical modeling of PAs has been explored. This chapter synthesizes the modeling approaches of the investigated references. Based on the Refs. [26, 39, 61, 82], the cascade structure is employed for PA dynamics. First, a rate-independent Preisach model is employed to represent the static hysteresis effect according to [37], and the coupling creep effect is also considered in this chapter. The direct piezoelectric effect is not modeled in PAs according to the investigation in [39]. Thus, this thesis employs the cascade connection of the Preisach hysteresis, creep, elec-

tric and vibration dynamics to represent the complex behavior of PAs. Furthermore, transfer functions are used for the creep, electric and vibration dynamics.

Fig. 4.2 shows the hysteresis effect Γ and the electric dynamics comprising the resistance R and the capacitance C. u is the input voltage to the PA. u_v is the voltage drop due to piezoelectricity. T_{em} is the electromechanical transformer ratio due to the inverse piezoelectric effect.

Fig. 4.3 illustrates the cascade connection of the rate-independent hysteresis and the non-hysteretic dynamics. The model sketch is represented by the classical Preisach model Γ, the creep dynamics G_{c}, the electric dynamics G_{e} and the vibration dynamics G_{v}. v is the unmeasurable hysteresis output. x is the vibration displacement before creep and y is the piezo displacement. F_v is the force due to the inverse piezoelectric effect. According to the piezoelectricity principle, the following linear relationship holds [26].

$$F_v = T_{\mathrm{em}} u_v. \tag{4.1}$$

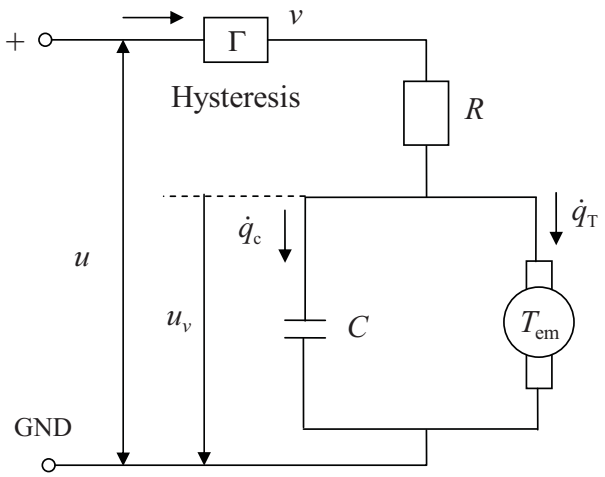

Figure 4.2: Sketch of the hysteresis, electric dynamics and piezoelectricity.

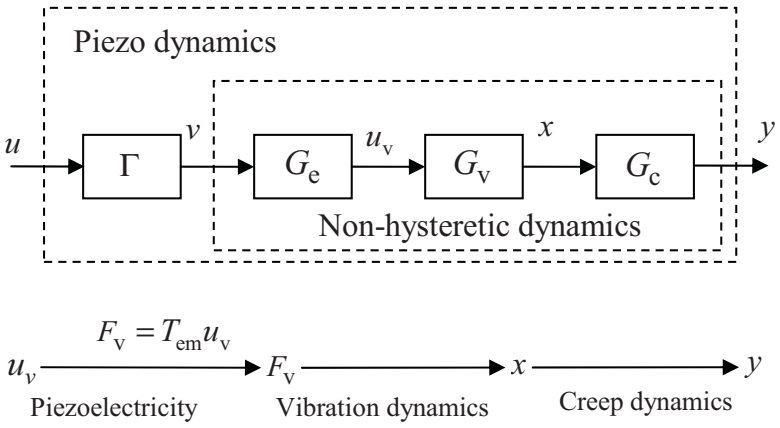

Figure 4.3: Series of the Preisach hysteresis and non-hysteretic dynamics.

The rate-independent hysteresis Γ is represented by classical Preisach model [29]

$$v(t) = \iint_S \mu(\alpha, \beta)\gamma_{\alpha\beta}[u(t)]d\alpha d\beta \tag{4.2}$$

where S is the limiting triangle with $\alpha \geq \beta$ in Preisach plane and $v(t)$ is the hysteresis output. $\mu(\alpha, \beta)$ and $\gamma_{\alpha\beta}$ are the density function and the hysteron output at point (α, β) in Preisach plane, respectively. For PAs with positive input voltage, the hysteron output can be set to be 1 and 0. The limiting triangle S in Preisach plane is divided into S^+ with $\gamma_{\alpha\beta} = 1$ and S^- with $\gamma_{\alpha\beta} = 0$. According to Fig. 4.3, the electric and vibration dynamics can be collectively represented as

$$G_{\text{ev}}(s) = \frac{k_{\text{ev}}}{\tau s + 1} \frac{\prod_{j-2}^{n} \left(s^2 + 2\bar{\xi}_j \bar{\omega}_j s + \bar{\omega}_j^2\right)}{\prod_{j}^{n} \left(s^2 + 2\xi_j \omega_j s + \omega_j^2\right)} \tag{4.3}$$

where $G_{\text{ev}}(s) = G_{\text{e}}(s)G_{\text{v}}(s)$, $\tau = RC$ is the time constant of the electric dynamics, ξ_j and ω_j are the damping ratio and mode frequency of the mechanical mode j, respectively, n is the model number of vibration dynamics.

Using the series connection of springs and dampers [75], the relationship between x

and y is the creep dynamics which is represented as

$$G_{\mathrm{c}}(s) = k_{\mathrm{c}} \prod_i \frac{s + z_{ci}}{s + p_{ci}} \tag{4.4}$$

where p_{ci} and z_{ci} are the poles and zeros of the creep dynamics, respectively, k_{ev} and k_{c} are constants.

The objective of this chapter is to estimate the Preisach density function $\mu(\alpha, \beta)$ and the creep, electric and vibration dynamics of the PAs represented in equations (4.2)-(4.4), by employing designed input signals. Additionally, the soundness of the identification will be demonstrated in experiments.

4.3 Hysteretic Behavior of Preisach Model Under Square Inputs

This section will highlight the Preisach hysteretic behavior when the input signal is a square wave. The rate-independent Preisach hysteresis with a square wave input behaves as an input uncertainty gain without dynamic responses. Thus, if the electrical and vibration dynamics of PAs are separately identified using a square wave signal, the DC gain identified will be different with different input signal amplitudes. This gain uncertainty is actually due to the Preisach hysteresis.

The classical Preisach model is employed to represent the rate-independent hysteresis, as given in (4.2). Additionally, the Preisach hysteresis is path-dependent and has global memories, and clearly, there is no velocity or acceleration terms in the classical Preisach hysteresis. Fig. 4.4 illustrates the square wave input signal in Preisach plane. Fig. 4.4

(a) shows the input voltage increasing from 0 to u_2. In the shaded area, the hysterons are activated with $\gamma(\alpha, \beta) = 1$. Conversely, the hysterons in the blank area and the outside of the triangle have $\gamma(\alpha, \beta) = 0$. The same shaded range is formed whether the voltage variation happens in instantaneous time or over a very long period, i.e., this is the rate-independent property as the output only relies on the historical input extremes and current input. If the voltage alters instantaneously, the hysteresis output also responds instantaneously. Similarly, if the input voltage changes from u_2 to u_1, a new shading range is formed as shown in Fig. 4.4(b). Fig. 4.4(c) shows the resultant area S_m due to the square input signal. The square wave input signal with the extremes of u_1 and u_2 results in square output with the extremes of v_1 and v_2. Moreover, there is no time delay between the input and output signals, as shown in Fig. 4.4(d). Thus, under square wave inputs, the hysteresis output v can be represented as

$$v = \lambda_0 + \lambda_u u \tag{4.5}$$

where λ_0 is the offset value and λ_u is the uncertainty gain.

Remark 4.1. *The effect of classical Preisach hysteresis with a square wave input is to alter the input signal magnitude. In other words, for a square wave input, the classical Preisach hysteresis behaves as a nonlinear amplifier without phase delay and dynamic response. This property will be harnessed in the identification of the non-hysteretic components.*

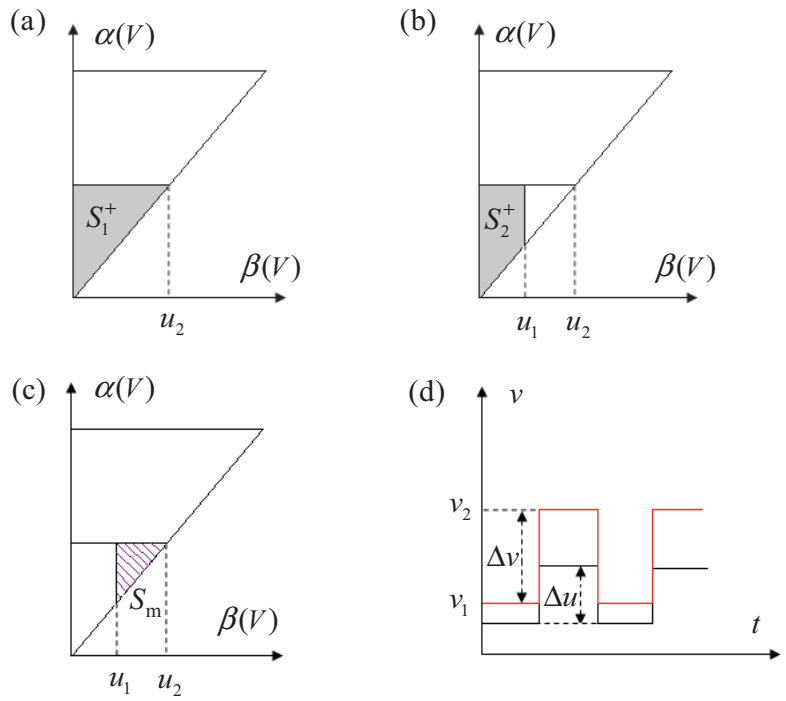

Figure 4.4: Preisach hysteresis behavior under square wave input signals. (a): The input voltage increases from 0 to u_2, forming the activated area S_1^+ in Preisach plane. (b): The input voltage decreases from u_2 to u_1, forming activated area S_2^+ in Preisach plane. (c): The area change (S_m) in Preisach plane under the square wave input with u_1 and u_2 as peak-to-peak values. (d): The resulting hysteresis output $v(t)$ under the square wave input. $\triangle v$ is the variance of the hysteresis output and $\triangle u$ is the variance of input signal.

4.4 Design of Input and Sampling Rules for Preisach Hysteresis Estimation

4.4.1 Input Signal Design

Special input signals with varying amplitudes are constructed to yield the data set for Preisach hysteresis identification. Unlike the case of dynamical systems, adequate frequencies are not helpful to identify the rate-independent Preisach hysteresis as it has no dynamic elements. Conversely, the input signals with adequate amplitudes can activate more relay hysterons and result in adequate memory curves. Thus, adequate amplitudes are efficient to satisfy the PE condition in parameter identification of Preisach model.

To achieve adequate amplitudes, the input voltage $u(t)$ with monotonically increasing stair amplitudes is constructed as in equation (4.6). With the maximum voltage $u_{\max}$, the input range is $[0, u_{\max}]$. After each harmonic period, the input signal returns to 0.

$$u(t) = \frac{P(t)}{2}(1 - \cos \omega_{\mathrm{r}} t) \tag{4.6}$$

where t is time, $\omega_{\mathrm{r}} = 1/T_{\mathrm{sub}}$, and T_{sub} is the period of each harmonic signal, as shown in Fig. 4.5. $P(t)$ is the stair amplitude of the input signal which is represented as

$$P(t) = fix(1 + \frac{t - fix(t/T)T}{T_{\mathrm{sub}}}) \cdot \delta \tag{4.7}$$

where T is the period of $P(t)$, and $T = L\omega_{\mathrm{r}}$, as shown in Fig. 4.5. $fix(x)$ is a function to round x to its nearest integer towards zero and δ is given by

$$\delta = u_{\max}/L \tag{4.8}$$

where L is the discretization level, and $u_{\max}$ is the maximum voltage for identification.

Fig. 4.5 graphically illustrates the input signal constructed using equation (4.6). The amplitudes match the discretization grid points in the Preisach plane.

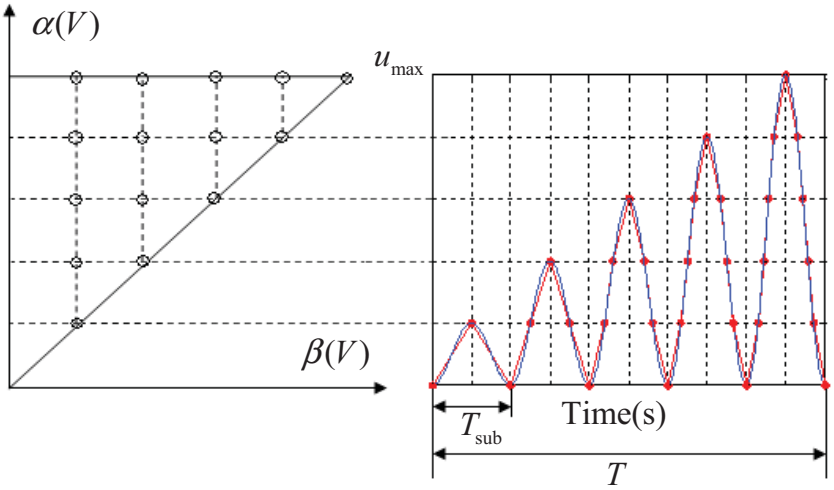

Figure 4.5: Sampling and discretization of Preisach plane.

4.4.2 Sampling Rule Design

The sampling rule is constructed depending on the input signal in equation (4.6). The Preisach plane is expanded by the input voltage. The hysteresis output directly depends on input voltage u, not on time t. Moreover, the classical Preisach model is rate-independent. Thus, it is more suitable to perform sampling based on the input u instead of time t. In this chapter, a sampling law depending on input voltage u is designed. To improve computing efficiencies, the input voltage u is sampled according to the discretization points in the Preisach plane.

The uniform sampling interval δ_s is represented as

$$\delta_s = \delta/N \tag{4.9}$$

where N is the sampling number at each grid.

According to input voltage equation (4.6), the sampling time in the ith harmonic signal is computed and represented as

$$\begin{cases} t_{i,j} = \arccos(1 - \frac{2j\delta_s}{P(t)})/\omega_{\mathrm{r}} + t_{i,1} \\ t_{i,2s_i-j} = (2\pi - \arccos(1 - \frac{2j\delta_s}{P(t)}))/\omega_{\mathrm{r}} + t_{i,1} \end{cases} \tag{4.10}$$

where $j = 1, 2, \cdots, s_i$, $s_i = P_i/\delta_s$, and $t_{i,1}$ is the starting time of ith harmonic signal.

Fig. 4.6 shows the sampling points in ith harmonic signal. P_i is the amplitude of ith harmonic signal in equation (4.7).

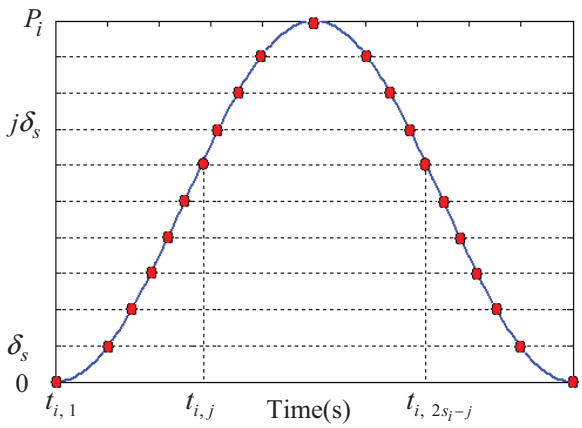

Figure 4.6: Illustration of sampling points in the i period.

4.4.3 SVD-based Hysteresis Identification

According to the discretized Preisach model and the sampling rule in (4.10), the following equation can be obtained for hysteresis identification.

$$AX = Y \tag{4.11}$$

where $A^T = [A_1^T, A_2^T, \cdots, A_m^T]$ and m is the sample number.

Using the input voltage in (4.6) and the sampling rule in (4.10), $A^T A$ is full rank and the PE condition of Preisach identification can be satisfied, as shown in the Appendix 6.2. However, there are measurement noise and disturbances which may result in small singular values and degrade identification accuracy. Furthermore, $A^T A$ is easily ill-conditioned because of large discretization of Preisach hysteresis.

To estimate the vector X with less sensitivity to disturbances and measurement noise in Y, least squares method and singular value decomposition (SVD) are used to compute the pseudo inverse of A. The SVD of $A^T A$ can be written as

$$A^T A = U \Sigma V \tag{4.12}$$

where $U = [u_1, u_2, \cdots, u_{L(L+1)/2}]$, $V = [v_1, v_2, \cdots, v_{L(L+1)/2}]$, U and V are unitary matrices, $\Sigma = \mathrm{diag}(\sigma_1, \sigma_2, \cdots, \sigma_{L(L+1)/2})$. Singular values $\sigma_1 \geq \sigma_2 \geq \cdots \geq \sigma_{L(L+1)/2} \geq 0$. If the singular values less than σ_r are truncated, the pseudoinverse of A is written as

$$A^+ = V \Sigma_r^{-1} U^T A^T \tag{4.13}$$

where $\Sigma_r^{-1} = \mathrm{diag}(1/\sigma_1, 1/\sigma_2, \cdots, 1/\sigma_r, 0, \cdots, 0)$.

Finally, the estimation $\hat{X}$ is represented as

$$\hat{X} = A^+ Y \tag{4.14}$$

where A^+ is the pseudoinverse of matrix A.

The sampling rule in (4.10) is not only to satisfy the PE condition of Preisach identification, but also the computational efficiency is also improved. For example, for the

discretization $L = 50$, 50 harmonic signals are needed to satisfy the PE condition. If the sampling depends on time, the time interval is 1ms and the input signal period $T_{\text{sub}} = 2$s, the dimension of matrix A is 100000×1275 which is a very large matrix and it is computationally intensive to get A^+ using software. However, the sampling law in equation (4.10) is employed instead, the dimension of matrix A is reduced to 2551×1275.

Remark 4.2. *The input signal with adequate amplitudes satisfies the PE condition of Preisach hysteresis identification. To treat the ill-conditioned problem resulting from large discretization of Preisach hysteresis, SVD can be employed to compute the pseudo-inverse of A, in which small singular values should be truncated.*

4.5 Proposed Identification Approach

The components of hysteretic dynamics of PAs are identified step by step. The square wave signal is employed to identify the creep, electric and vibration dynamics with multiple temporal scales. For typical PAs, the time constant of the creep dynamics is in the order of minutes, but the electric and vibration dynamics is in the order of ten milliseconds. Thus, the creep and electric/vibration dynamics are identified over two steps. In this chapter, the ARMAX modeling approach is employed to yield the non-hysteretic dynamic models [64]. Afterwards, the Preisach hysteresis is identified by employing the input signal in (4.6) and the sampling rules in (4.10).

First, the identification of creep dynamics is carried out using a square wave input signal with the period in the order of minutes. The gain k_{c} is normalized to one, since

k_c is absorbed in the hysteretic part. Moreover, compared with the sampling for the identification of the electric and vibration components, the sampling rate for the creep identification is slower so as to reduce the measurement noise and the effects resulting from the electric and vibration dynamics.

Second, the identification of the electric and vibration is implemented also by employing a square wave signal, but the period is the order of ten milliseconds. The gain k_{ev} is set to one. During this step, the creep effect is eliminated with a model-based inversion, as shown in Fig. 4.7. $\hat{G}_c^{-1}(s)$ is the inversion of the estimated creep model. Moreover, the sampling rate is set as fast as possible to capture the responses at high frequencies.

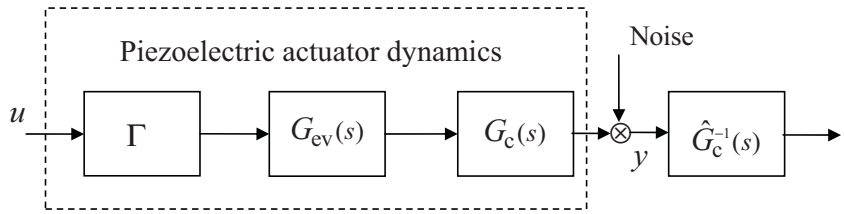

Figure 4.7: Inverse creep to identify electric and vibration dynamics.

Finally, by employing the designed harmonic signal and sampling rules, the rate-independent hysteresis is identified with the SVD-based least square estimation in (4.14). The creep, electric and vibration affection are eliminated using their model inversion, as shown in Fig. 4.8. $\hat{G}_{ev}^{-1}(s)$ is the inversion of the estimation of electric and vibration dynamics.

Remark 4.3. *The creep, electric and vibration dynamics in PAs are typically of multiple temporal scales. The creep is slow dynamics in the order of minutes, but the electric and vibration dynamics are fast dynamics in the order of milliseconds. It is not suitable to*

identify them simultaneously. This chapter identifies the creep, electric and vibration dynamics by employing square inputs at different temporal scales.

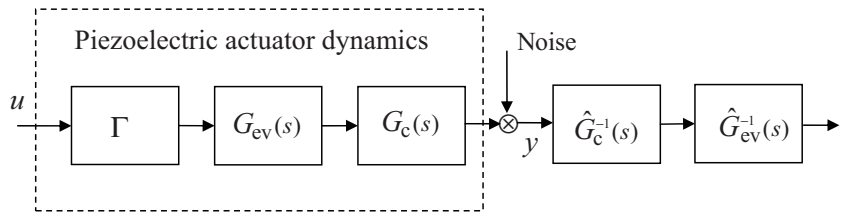

Figure 4.8: Inverse creep and vibration to identify hysteresis.

4.6 Simulation Studies

This section presents the simulation study of the proposed identification approach. The density function $\mu(\alpha, \beta)$ in (4.2) is set to $0.1+0.05(\alpha+\beta)$. The parameters of the electric and vibration dynamics in (4.3) are set as $\tau = 0.001$, $\xi = 0.1$ and $\omega_n = 3000$rad/s. The parameters of creep dynamics in (4.4) are set as $p_{c1} = 0.02$, $p_{c2} = 10$, $z_{c1} = 0.12$, $z_{c2} = 15$ and $k_c = 2$. Additionally, white noise with the root mean square (RMS) of $0.07\mu m$ is added to the measured displacements.

4.6.1 Creep, Electric and Vibration Dynamics Identification

Two sampling rates are used in the identification of the creep, electric and vibration dynamics. A slow sampling rate is used in the creep identification. Conversely, a fast sampling rate is used in the identification of the electric and vibration dynamics. For the creep identification, the sampling interval is set to 20ms and the input square period is set to 200s. The identified model is shown in equation (4.15), while the na, nb and nc

of the ARMAX model are set to 3, 4, 3, respectively.

$$\hat{G}_{\mathrm{c}}(s) = \frac{(s+0.1199)(s+14.58)}{(s+0.02)(s+10.11)}\left(\frac{-s+98.82}{s+100.1}\right). \tag{4.15}$$

The estimated errors of $p_{c1}, p_{c2}, z_{c1}, z_{c2}$ are less than 3% of the real values. Note that the gain is normalized to one and k_{c} is absorbed into the hysteresis part. The last term $(-s+98.82)/(s+100.1)$ on the right side of equation (4.15) is due to the coupling effects from the electric and vibration dynamics at high frequencies. In this step, it is directly removed. The residual dynamics is identified together with the electric and vibration dynamics. The creep dynamics is represented as

$$\hat{G}_c(s) = \frac{(s+14.58)(s+0.1199)}{(s+10.09)(s+0.02)}. \tag{4.16}$$

After the creep identification, the electric and vibration identification is carried out. The creep effect is eliminated with the model inversion $\hat{G}_c(s)^{-1}$. The period of square wave signal is set to 0.1s and the sampling interval is 0.1ms. 2000 points are used to estimate the electric and vibration dynamics using ARMAX approach. The identified result is given as

$$\hat{G}_{\mathrm{ev}}(s) = \frac{1}{0.001016s+1}\cdot\frac{8.999\times 10^6}{(s^2+593.6s+8.999\times 10^6)}. \tag{4.17}$$

The estimated time constant, resonant frequency and damping ratio are 0.001016, 2999.8 and 0.0989, respectively. The parameter estimation errors of the electric and vibration dynamics are 1.6%, 0.007%, 1.1% of their normal values.

Remark 4.4. *The poles and zeros close to the slow sampling frequency can be ignored in the identification of the creep dynamics which is slow and in large temporal-scale*

compared with the electric and vibration dynamics. Afterwards, the poles and zeros ignored in the creep identification can be accurately identified in the electric and vibration dynamics in which the fast sampling rate is employed.

4.6.2 Hysteresis Identification

The input signal frequency is chosen to be 1Hz. Let the identified density function be in the voltage range of $[0, 5]$. The discretization level of the Preisach plane is set to 10. The amplitude variance of the harmonic signals in each period is chosen to be 0.5V. The sampling level N is set to 1. The parameters of the input signal in (4.6) and sampling law in (4.10) are chosen as $u_{\max} = 5$, $L = 10$, $\delta = 0.5$, $\omega_{\mathrm{r}} = 2\pi$, $T_{\mathrm{sub}} = 2$s and $T = 10$. Model based inversion is used to eliminate the creep, electric and vibration dynamics. Since the input signal is at low frequencies, the inversion of electric and vibration dynamics is simplified as

$$\hat{G}_{ev}^{-1} \approx 1 + 0.001082\frac{s}{1+\epsilon s} \tag{4.18}$$

where ϵ is a small positive value that is chosen according to the input signal frequency. ϵ is set to 0.01 in this simulation.

Fig. 4.9(a) shows the hysteresis curve with drift suppression using the blue model-based inversion of creep, electric and vibration dynamics. The magnitude distortion and phase delay are suppressed by the model-based inversion. 66 sampling points are collected to identify Preisach density function by employing the least squares method. The matrix $A^T A$ is full rank and PE condition is satisfied. Fig. 4.9 (b) shows the identified density function. The density function identification is close to its nominal

value with the relative error less than 2%.

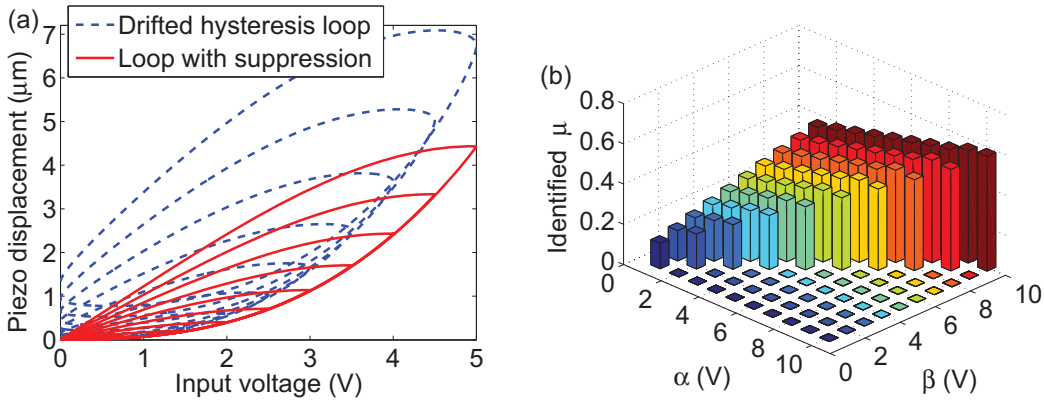

Figure 4.9: (a): Creep suppression. (b): Identified result of density function.

As a comparison, the frequency-domain identification approach in [65] is also performed in the simulation study, in which the input is a chirp signal with a constant amplitude but varying frequencies (higher than 100Hz). The identified electric and vibration dynamics are shown in Fig. 4.10. In addition to the DC gain uncertainty, the mode frequencies of the identified electric and vibration dynamics decrease compared with the actual model, because the hysteresis effect is not modeled and regarded as part of the electric and vibration dynamics.

4.7 Experimental studies

4.7.1 Identification of the Hysteresis, Creep, Electric and Vibration Dynamics

First, the creep dynamics is identified using a square wave input signal with the period of 400s. The sampling interval is set to 10ms. Using this time scale, less dynamic response is sampled. The poles and zeros faster than the sampling interval are ignored.

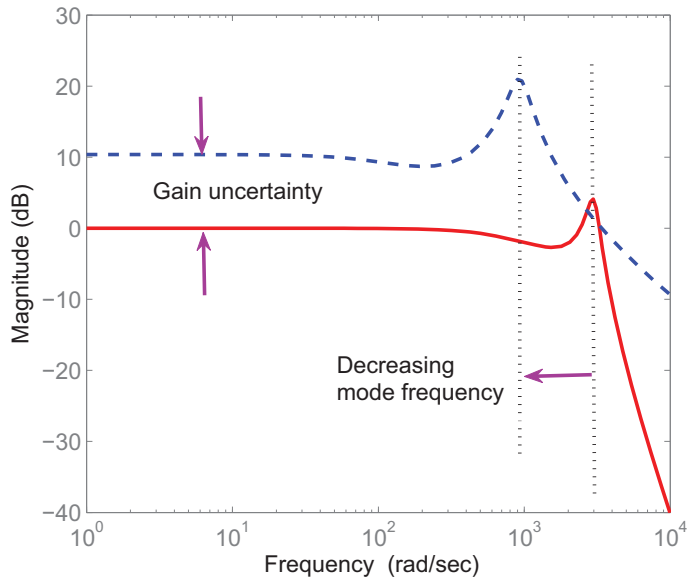

Figure 4.10: Identified vibration and electric dynamics by employing frequency-domain method. Solid line: The real vibration and electric dynamics. Dashed line: The identified vibration and electric dynamics. There are DC gain uncertainties and mode frequency decreasing due to the hysteresis effect.

The identified creep transfer function is represented as

$$\hat{G}_c(s) = \frac{(s+0.01458)(s+0.1716)(s+0.241)}{(s+0.01419)(s+0.1684)(s+0.2402)} \cdot \frac{(s+1.07)(s+18.29)}{(s+1.053)(s+17.57)}.$$

After the identification of creep dynamics, the identification of the electric and vibration dynamics is carried out with a sampling interval of 0.05ms. The square wave input signal with 20 millisecond period is used. The creep effect is eliminated with its model inversion. Similarly as in the simulation study, ARMAX structure with na=5, nb=6, and nc=5 is used.

The identified electric and vibration dynamics is represented as

$$\hat{G}_{ev}(s) = \frac{1}{0.00049s+1} \cdot \frac{8.1\times 10^6}{s^2+3901s+8.1\times 10^6} \cdot \frac{2.41\times 10^7}{s^2+805s+2.41\times 10^7}$$

In equation (4.19), the time constant is 0.00049s. The mode frequencies of the piezo-

electric stage are 2846 rad/s and 4909 rad/s. The mode damping factors are 0.69 and 0.082. The identification results indicate that the model structure in Section 4.2 is effective for the piezoelectric stage.

Finally, the rate-independent Preisach hysteresis is identified by employing the harmonic signal with varying amplitudes in equation (4.6). The period of each signal is 2s. The identified voltage range is [0, 50]V. The discretization level L is set to 50. Thus, 50 harmonic signals are needed. The parameters in equations (4.6) and (4.7) are with $\delta = 1$, $u_{\max} = 50$, $T_{\text{sub}} = 2$s, $\omega_{\text{r}} = 0.5$, $T = 100$s and $N = 1$. The drift is observed in the displacement output.

At low frequencies, the inversion of the identified electric and vibration equation (4.19) is simplified as

$$\hat{G}_{ev}^{-1}(s) \approx 1 + 0.001005\frac{s}{1+\epsilon s} \tag{4.19}$$

where $\epsilon = 0.02$ is used to eliminate the electric and vibration effect for hysteresis identification.

Fig. 4.11 shows the identified Preisach density function. The singular values less than 0.00001 times of the maximum singular value are truncated.

4.7.2 Model Validation

The adequacy of the identified hysteretic model is validated by employing the comparison of the measured and simulated hysteretic curves, in additional to the model-based inversion feedforward control. First, the input-output hysteretic curves, based on the identified model at different frequencies, are compared to the measured hysteretic curves.

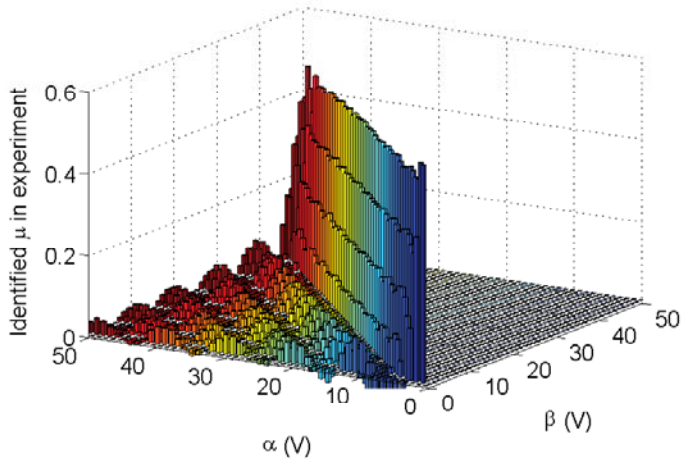

Figure 4.11: Identified density function μ in the experiment.

Fig. 4.12 shows the measured and simulated hysteretic curves at different frequencies without considering displacement offset. The simulated hysteresis curves have small errors compared with the measured hysteresis curves.

To represent the identification accuracy of the hysteretic dynamics, we employ the relative error between the estimated displacement error and the measured displacement, because the density function μ is unknown in real experiments. The relative error $e_y(\%)$ is represented as

$$e_y(\%) = \frac{\|y - \hat{y}\|}{\|y\|} \times 100\% \tag{4.20}$$

where $\|\cdot\|$ denotes the Euclidean norm, y and $\hat{y}$ are the measured and estimated displacements, respectively.

The relative errors $e_y(\%)$ at 0.05Hz, 4Hz, 100Hz and 600Hz are shown in Table 4.1. The relative errors between the simulated and measured hysteretic curves are within a small range, which indicates the soundness of the model identification.

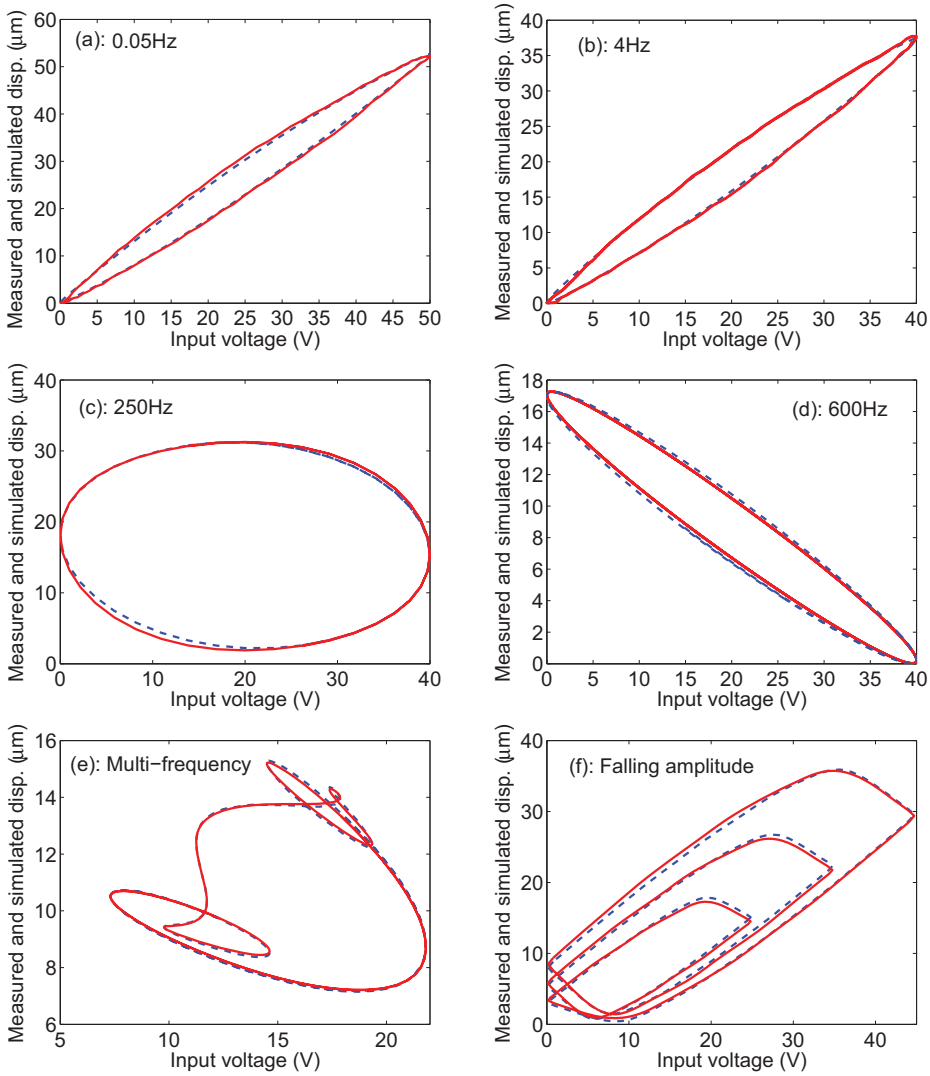

Figure 4.12: Comparison of the measured and simulated hysteretic curves at different frequencies. Solid line: The simulated hysteretic curves. Dashed line: The measured hysteretic curves. (a)-(d): Sinuoidal inputs. (e): Multi-frequency input $u(t) = 2\sin 200\pi t + \sin 600\pi t + \sin 800\pi t + \sin 1000\pi t + 11$. (f): Triangular input with falling amplitudes.

Table 4.1: Relative errors (%)

Frequency	Simulated e_y	Inversion (e_r)	Open loop (e_r)
0.05Hz	0.51%	0.77%	7.52%
4Hz	1.08%	1.34%	9.12%
250Hz	1.79%	2.41%	74.88%
600Hz	2.42%	4.32%	107.12%
Multi-fre.	1.42%	2.18%	56.95%
Multi-amp.	2.46%	3.01%	39.03%

Next, without considering displacement offset, the model-based inversion feedforward compensator is implemented to demonstrate the effectiveness of model identification. Fig. 4.13 illustrates the model-based inverse feedforward compensator and the direct open loop control without compensation. In the open loop case without compensation, the positive value γ is used to regulate the input-output gain, such that the desired and the actual displacements have a gain of one. The values of γ at 0.05Hz, 4Hz, 100Hz and 600Hz are set to 0.9, 0.96, 1.0, 1.05, respectively.

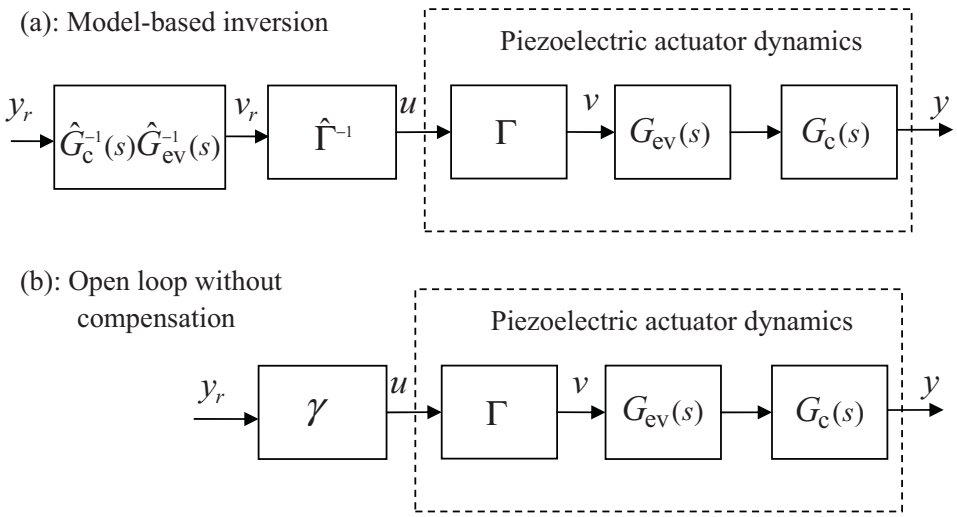

Figure 4.13: (a): Model-based inversion. (b): open loop without compensation.

This chapter only employs periodic trajectories $y_r(t)$ which can be represented by sinusoidal signals using the Fourier series as follows

$$y_r(t) = \sum_i M_i \sin(\omega_i t + \theta_i). \tag{4.21}$$

where M_i, ω_i and θ_i are the amplitude, frequency, and phase of the ith term, respectively.

For a sinusoidal signal, the inversion of the non-hysteretic dynamics can be achieved by changing the phase and gain. Therefore, the reference trajectory v_r can be obtained as [44]

$$v_r(t) = \sum_i M_i / |G_{\mathrm{c}} G_{\mathrm{ev}}(j\omega_i)| \sin(\omega_i t + \theta_i - \angle G_{\mathrm{c}} G_{\mathrm{ev}}(j\omega_i)) \tag{4.22}$$

Then, the inversion of Preisach hysteresis is computed. The output $v_r(t)$ of $\hat{G}_{\mathrm{c}}^{-1}\hat{G}_{\mathrm{ev}}^{-1}$ is regarded as the input of $\hat{\Gamma}^{-1}$, as shown in Fig. 4.13(a).

If the estimated hysteresis output $\hat{v}$ tracks the reference v_r within the error range e, the feedforward voltage remains the same. If the estimated hysteresis output $\hat{v}$ is less than the reference v_r and $|v_r - \hat{v}| > e$, the feedforward voltage is increased and vice versa. The details of the Preisach-based hysteresis inversion can be found in Ref. [84].

Fig. 4.14 shows the performance of the model-based inversion feedforward compensation. The feedforward compensator reduces the error significantly compared to the open loop without compensation. Similarly, the relative error e_r is represented as

$$e_r(\%) = \frac{\|y_r - y\|}{\|y_r\|} \times 100\% \tag{4.23}$$

where $\|\cdot\|$ denotes the Euclidean norm, y_r and y are the desired and the measured displacements, respectively.

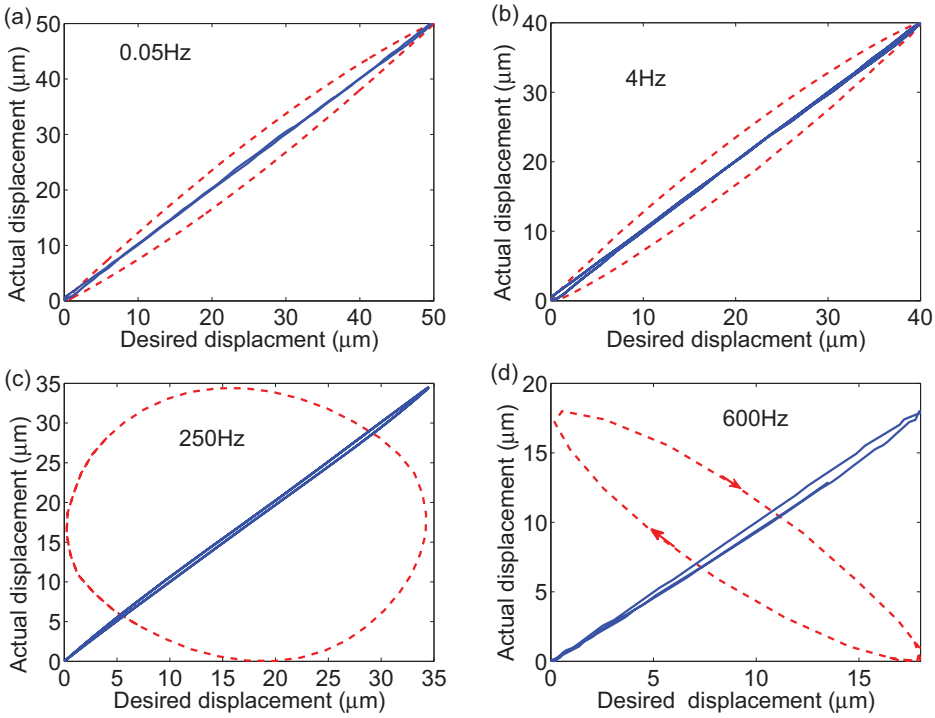

Figure 4.14: Model-based inverse feedforward performance of sinusoidal signals. Dashed line: open loop without compensation. Solid line: model-based inversion feedforward compensation.

To further demonstrate the effectiveness of the identification result, multi-frequency and falling-amplitude trajectories are also investigated using the model-based inversion feedforward compensator, as shown in Figs. 4.15 and 4.16. The PA displacement tracks the desired trajectories within small error range.

The relative errors e_r are shown in Table 4.1. It can be seen that, without considering offset, the model-based inversion feedforward compensator is effective to compensate the hysteretic dynamics over broadband frequencies, indicating that the modeling and the identification of the PA are also effective.

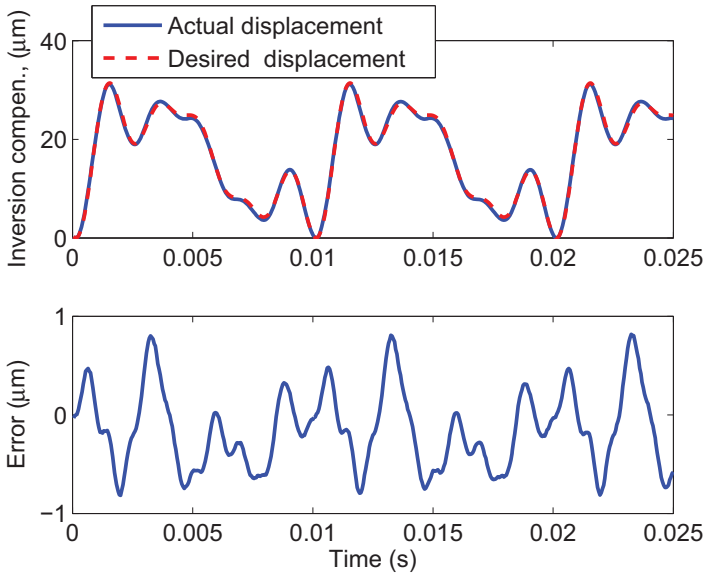

Figure 4.15: Model-based inversion feedforward performance of the multi-frequency trajectory ($y_r = 12\sin 200\pi t + 6\sin 600\pi t + 6\sin 800\pi t + 6\sin 1000\pi t + 16.2$).

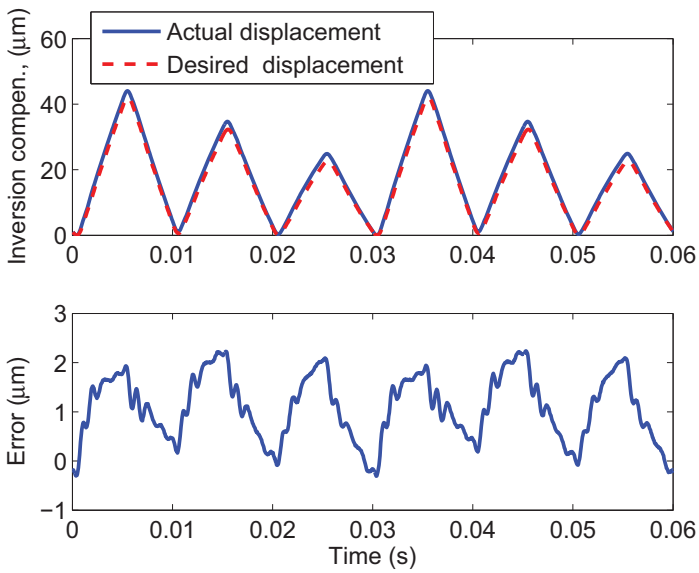

Figure 4.16: Model-based inversion feedforward performance of the dropping triangular trajectory with three extremes and a basic frequency of 100Hz.

4.7.3 Discussion

The accurate identification over broadband frequencies is a key bottleneck for simultaneous high-speed and precision motion of PAs using model-based inversion feedforward compensators. In the experimental investigation of the piezoelectric stage over a broad range of frequencies, the hysteretic dynamics, comprising the coupled hysteresis, creep, electric and vibration dynamics, has been identified by employing the proposed systematic strategy. Additionally, the effectiveness has been demonstrated by the model-based inversion feedforward compensator and the comparison of the hysteretic curves between the piezo displacement and the input voltage.

Compared with the identification approaches of the cascade model comprising the hysteretic and non-hysteretic dynamics in Refs. [80,81], the couplings are fully considered in this chapter. The coupling treatment improves the identification accuracy. Additionally, in contrast to the dynamic hysteresis identification based on the rate-dependent hysteresis model as in Ref. [59], the density function assumption and the curve fitting technique are not adopted in this chapter. Furthermore, it is convenient to design modern controllers based on the identified non-hysteresis dynamics rather than the rate-dependent hysteresis. Compared with the investigated references in this chapter, the proposed identification strategy is described step-by-step and it is convenient to perform the experiments by other readers and researchers with the proposed guidelines.

To implement the model-based inversion feedforward compensator efficiently, the feedforward input signal can be computed offline. Then, the data is written into a DSP board

for realtime compensation. The measurement noise lays outside the feedforward branch. Thus, it is more suitable to track high frequency trajectories compared with feedback compensators.

At low frequencies, the modeling of PAs could be simplified to static Preisach hysteresis, because the electric and vibration dynamics of PAs approach their DC gains at low frequencies. Chapter 2 investigates the static Preisach hysteresis of PAs at low frequencies where the creep is suppressed using curve fitting techniques, but as the reference frequencies increase to 25Hz, the compensation errors of the Preisach-based inversion feedforward increase significantly. Conversely, the compensation error of the model-based inversion feedforward in this chapter is still less than 4.32% at 600Hz.

The limitation of discretization levels of the Preisach hysteresis still exists in this chapter. If the Preisach hysteresis in (4.2) is discretized with larger levels, the computing of $A^T A$ will be more time-consuming for a CPU [39]. As a result, the discretization level is limited in experiments, and the identification accuracy of the Preisach hysteresis is also limited.

4.8 Conclusion

To achieve accurate model identification of PAs at broadband frequencies, this chapter presents a systematic identification strategy of the coupled rate-independent hysteresis, creep, electric and vibration dynamics. First, the creep dynamics is identified using square wave signals with long periods. After eliminating the creep effect, the electric and

vibration dynamics are identified by employing square wave signals with short periods. Finally, using harmonic signals with varying amplitudes, the rate-independent hysteresis is identified by specially designed input signals and sampling rules. The soundness of the proposed identification approach is demonstrated in simulation and experimental studies.

Furthermore, using the identified hysteretic model in this chapter, Chapter 5 will design a muitirate-based composite controller which can track trajectories at rates twice higher than the resonant frequencies using a modest DSP platform.

Chapter 5

Multirate-Based Controller Design for High-Bandwidth and Precision Tracking

5.1 Introduction

High-speed nanofabrication and dynamic imaging of scanning probe microscopes are requiring PAs to perform fast tracking, possibly beyond their first resonant frequencies. However, classical controllers have limited bandwidth and high frequency performance. Simultaneous high-bandwidth (beyond resonant frequencies) and precision tracking of PAs are still not solved well. Commercial atomic force microscopes typically operate at rates lower than 10% of their first resonant frequencies due to the complex and hysteretic dynamics comprising the coupled hysteresis, creep, electric and vibration dynamics in PAs [23, 44, 56, 60].

To compensate hysteretic dynamics and achieve precision tracking, various model-based compensators have been investigated. At low frequencies, Preisach-based inversion feedforward controller can be employed to compensate the static hysteresis of PAs [84,85].

High-gain feedback controllers are also employed to compensate the static hysteresis and creep of PAs [25], such as integral or proportional-integral controllers with high loop gain at low frequencies [54]. To expand the tracking bandwidth, modern feedback and inversion-based feedforward controllers have been combined mainly based on linear models of PAs [44]. For instance, [65] presents a 2-DOF feedforward-feedback controller and the tracking error at 300Hz (still lower than the first resonant frequency) is 5.28%. [25] proposes a notch filter and a inversion-based feedforward controller to enhance the high-gain feedback. However, the hysteresis is not modeled and the fine tracking at rates higher than the resonant frequency is still not provided in PA experiments. Additionally, dynamic or rate-dependent hysteresis models is employed to represent and compensate PA dynamics over a broadband range of frequencies [58]. Based on the rate-dependent Prandtl-Ishlinskii (P-I) hysteresis, the hysteresis-based inversion is employed to extend the tracking bandwidth [86], but it is difficult to apply modern control techniques to rate-dependent hysteresis, since most modern controllers are designed using non-hysteretic models.

To enhance the motion tracking of PAs, modern or intelligent controllers have also been investigated, such as the robust H_∞ controller [65], adaptive-based controller [39, 87], neural network-based controller [30], learning-based controller [88], etc. However, advanced or intelligent controllers are typically complex and need more calculations, which limits the updating rates of control signals. For instance, H_∞ and H_2 controllers commonly have high orders, since they have the same order as the generalized plants [89].

Furthermore, at high frequencies, feedback controllers with high gains easily approaches chattering and saturation when the amplified high frequency measurement noise coincides with the vibration modes of PAs. Thus, we design a feedback controller with the bandwidth lower than the resonant frequency of the PA to guarantee robust stability in the face of noise and disturbances at high frequencies. The broadband performance is achieved mainly by a model-based inversion feedforward controller.

To develop a composite controller with adequate high-bandwidth performance, we employ multirate techniques in the feedforward and feedback loops. Based on the linear dynamics of PAs, various multi-rate composite controllers have been investigated with different objectives. For example, [90], [91] and [92] present multirate perfect tracking controllers to handle non-minimum phase zeros, [93] models the transfer function of a multirate controller to evaluate the open-loop response. [94] provides an adaptive feedforward controller based on multirate discretization to compensate periodic disturbances. [95] proposes a multirate feedback controller to improve the intersample behavior. In this chapter, we investigate the different design and application of multirate techniques. The feedback controller is designed with a sampling rate, such that it can reject disturbances, reduce feedforward control errors, and suppress noise effect.

To track broadband trajectories beyond the resonant frequencies of PAs, I design the multirate-based composite controller comprising a model-based inversion feedforward controller and a robust H_∞ feedback controller, using the identified hysteretic dynamics in Chapter 4. For high bandwidth tracking, the model-based inversion feedforward

controller is constructed based on the identified hysteretic dynamics. Furthermore, a high sampling rate is used in the feedforward branch, since the computing of feedforward control signals can be performed off-line. To reject disturbances, a discrete robust H_∞ controller is designed with a low sampling rate which depends on disturbance bandwidth and DSP limits. In experimental studies, the proposed composite controller provides precision tracking at a rate beyond the resonant frequencies of the piezoelectric stage.

The organization of this chapter is as follows. Section 5.2 proposes the design strategy of the multirate-based composite controller. Section 5.3 presents the experimental studies of the proposed composite controller. Finally, Section 5.4 concludes the chapter.

5.2 Proposed Multirate-based Composite Controller Design

In this section, the multirate-based composite controller is presented. It consists of a model-based feedforward controller and a discrete H_∞ feedback controller. First, the model-based inversion feedforward controller is constructed to compensate the phase-lag and magnitude distortion. In order to improve the computing efficiency, the feedforward control signals are computed off-line. Then, they are written into the DSP platform for real-time implementation. The discrete H_∞ feedback controller with an integral action is built to suppress disturbances. The H_∞ controller design is a trade-off among the feedforward error, disturbances, calculations and noise.

Fig. 5.1 illustrates the proposed composite control strategy. "ZOH" denotes the zero-order-hold sampling, u_{ff} and u_{fb} are the feedforward and feedback signals, respectively.

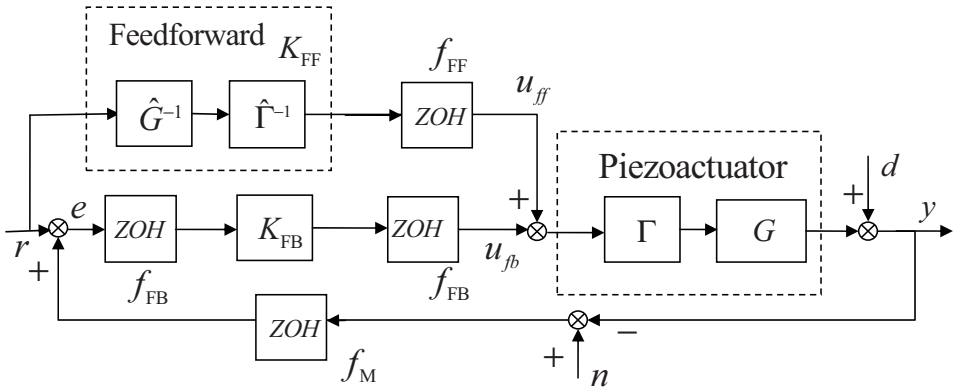

Figure 5.1: Multirate composite control strategy of PAs

The variables e, d and n denote the tracking error, output disturbance and measurement noise, respectively, G denotes the non-hysteretic dynamics of PAs and $G = G_c G_{ev}$, f_{FF}, f_{FB} and f_M denote the sampling rates of the feedforward, feedback and measurement signals, respectively, $f_{FF} = f_M$ is used in this article, $\hat{G}^{-1}$ and $\hat{\Gamma}^{-1}$ denote the inversions of the estimated non-hysteretic dynamics and hysteretic dynamics, respectively, K_{FF} and K_{FB} denote the feedforward and feedback controllers, respectively. The feedforward controller is constructed based on the PA dynamics. The discrete feedback controller is designed using the non-hysteretic dynamics while the rate-independent hysteresis in (3.1) is regarded as a bounded uncertainty.

5.2.1 Analysis of Proposed Composite Controller

The proposed composite controller is analyzed in this section. First, the model-based inversion feedforward controller K_{FF} of PAs can be written as

$$K_{FF} = \hat{\Gamma}^{-1} \circ \hat{G}^{-1} \tag{5.1}$$

where $\circ$ denotes the composition operator [96]. Multiplication is not used in (5.1), since the hysteresis Γ and its estimation $\hat{\Gamma}$ are strong nonlinearities with global memories [29]. $\hat{G}^{-1}$ and $\hat{\Gamma}^{-1}$ can be represented as

$$\begin{cases} \hat{G}^{-1} = G^{-1}(1+\delta_l) \\ \hat{\Gamma}^{-1} = \Gamma^{-1}(1+\delta_h) \end{cases} \tag{5.2}$$

where δ_l denotes the inversion error of the non-hysteretic dynamics and δ_h denotes the inversion error of the rate-independent hysteresis. δ_l and δ_h are bounded uncertainties and determined by the identification accuracy of PAs. Then, $\hat{\Gamma}^{-1}$ and $\hat{G}^{-1}$ can be rewritten as

$$\hat{\Gamma}^{-1} \circ \hat{G}^{-1} = \Gamma^{-1} \circ G^{-1}(1+\delta_l+\delta_h+\delta_l\delta_h). \tag{5.3}$$

Let $\delta_f = \delta_l + \delta_h + \delta_l\delta_h$, the model-based inversion feedforward controller of PAs is rewritten as

$$K_{\mathrm{FF}} = \Gamma^{-1} \circ G^{-1}(1+\delta_f) \tag{5.4}$$

where the bounded uncertainty δ_f can be determined using the feedforward control.

Then, the feedforward control signal u_{ff} can be given by

$$u_{ff} = \Gamma^{-1} \circ G^{-1}(1+\delta_f)r \tag{5.5}$$

The measurement noise n lays outside of the feedforward branch. With only the feedforward controller K_{FF} in (5.4) while the feedback controller $K_{\mathrm{FB}} = 0$, the relative error in e/r is given by

$$\frac{e}{r}|_{K_{\mathrm{FB}}=0} = \delta_f + \frac{d}{r}. \tag{5.6}$$

Eq. (5.6) indicates that the tracking performance of feedforward relies on the identification accuracy and the output disturbances are not suppressed. Thus, feedback control is necessary to guarantee stability and robustness in the face of modeling error δ and disturbance d.

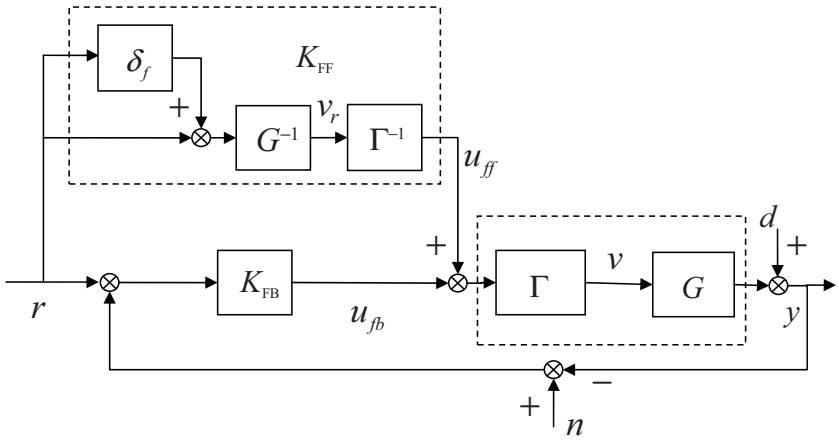

Figure 5.2: Analysis of proposed composite control strategy

Fig. 5.2 shows the proposed composite control strategy where $\hat{G}^{-1}$ and $\hat{\Gamma}^{-1}$ are represented by G^{-1} and Γ^{-1} according to (5.4), respectively. With the proposed composite controller, the relationship between the reference r and tracking error e can be represented as

$$\frac{e}{r} = \frac{1}{G \circ \Gamma \circ K_{\mathrm{FB}} + 1}\delta_f + \frac{1}{G \circ \Gamma \circ K_{\mathrm{FB}} + 1}\frac{d}{r} + \frac{G \circ \Gamma \circ K_{\mathrm{FB}}}{G \circ \Gamma \circ K_{\mathrm{FB}} + 1}\frac{n}{r}$$

where δ_f is the feedforward error, K_{FB} denotes the feedback controller, n and d are the measurement noise and output disturbance, respectively.

If the tracking error is suppressed by a factor of $\eta + 1$, i.e., $1/(G \circ \Gamma \circ K_{\mathrm{FB}} + 1) = 1/(\eta + 1)$, the feedback control signal due to measurement noise can be written as

$$u_{fb}^{n} = n\eta\,(\Gamma \circ G)^{-1} \tag{5.7}$$

where $\eta \gg 1$ at frequencies with fine tracking performance.

Typically, the PA is a low pass filter and the system gain is decreased at high frequencies. Conversely, the model-based inversion $(G \circ \Gamma)^{-1}$ is a high pass filter. Equation (5.7) indicates that the measurement noise n is amplified by $\eta\,(\Gamma \circ G)^{-1}$, and easily results in chattering and saturation when the amplified measurement noise coincides with the vibration modes of PAs.

Thus, the high frequency gain of K_{FB} is reduced for stability. Multi-objective robust H_∞ control is employed to design K_{FB}. The different objectives of the feedback controller are specified at different frequencies. The sampling rate and bandwidth of K_{FB} are the main specifications to be considered.

Remark 5.1. *The model-based inversion feedforward controller is employed to expand the bandwidth beyond the resonant frequencies of PAs, because the measurement noise lies outside of the feedforward branch. Conversely, the feedback controller is employed to reject disturbances and modeling error within feedback bandwidth. The high frequency gain of the feedback controller should be reduced to suppress noise effect.*

5.2.2 Off-line Model-based Inversion Feedforward Controller

Off-line model-based inversion feedforward controller can be employed if the reference is known. The feedforward controller is used to overcome the bandwidth limitation of the

feedback controller. It encompasses the inverse non-hysteretic dynamics and the inverse hysteresis. First, the reference signals pass through the inverse non-hysteresis dynamics $\hat{G}^{-1}$, then the inverse hysteresis $\hat{\Gamma}^{-1}$. The details of the model-based inversions $\hat{\Gamma}^{-1}$and $\hat{G}^{-1}$ can be found in Refs. [84, 97].

The Preisach-based inversion $\hat{\Gamma}^{-1}$ is shown in Chapter 3. The inversion of the non-hysteretic dynamics can be represented as

$$\hat{G}^{-1}(s) = \frac{\hat{\tau}s + 1}{\hat{k}_{\text{ev}}} \prod_{i=1}^{m} \frac{s + \hat{p}_i}{s + \hat{z}_i} \cdot \frac{\prod_i^n (s^2 + 2\hat{\xi}_i \hat{\omega}_i s + \hat{\omega}_i^2)}{\prod_j^{n-2} (s^2 + 2\hat{\xi}_j \hat{\omega}_j s + \hat{\omega}_j^2)} \tag{5.8}$$

where $\hat{k}_{ev}$, $\hat{\tau}$, $\hat{\xi}_i$, $\hat{\xi}_j$, $\hat{\omega}_j$ and $\hat{\omega}_j$ are the identified parameters of the electric and vibration dynamics, respectively, $\hat{z}_i$ and $\hat{p}_i$ are the estimated zeros and poles of the creep dynamics. Negative $\hat{z}_i$ and $\hat{\xi}_j$ are not considered in (5.8).

The feedforward control signal u_{ff} can be computed off-line through $\hat{G}^{-1}$ and $\hat{\Gamma}^{-1}$ for known and periodic trajectories which can be represented by Fourier series. Then, the data are written into a DSP platform for real-time feedforward control.

5.2.3 Design of Bandwidth and Sampling Rate

This section presents the design of the bandwidth and sampling rate of the multirate-based composite controller. The design of the bandwidth and sampling rate in the feedback loop is the key issue, since the bandwidth and sampling rate in the feedforward loop is easier to determine as the computations can be done off-line. The feedforward bandwidth is determined by the identification accuracy of the PA dynamics and its sampling rate can be set to the maximum value which a DSP supports.

Design of Feedback Bandwidth

The bandwidth of the feedback controller is important to guarantee stability and suppress disturbances. Design of the bandwidth in the feedback loop is a trade-off among tracking errors, disturbances and measurement noise. Let the bandwidth of output disturbances be ω_d. The measurement noise n is assumed to be white noise. First of all, the maximum sampling rate $f_{\max}$ of a DSP platform poses a limitation on both the feedforward and feedback bandwidth [98]

$$\omega_{\mathrm{FF}} \leq \frac{f_{\max}}{2}, \quad \omega_{\mathrm{FB}} < \frac{f_{\max}}{2}$$

To reduce modeling error, drifts and other disturbances in piezoelectric mechanisms, the bandwidth of feedback controller is higher than the disturbance bandwidth ω_d

$$\omega_{\mathrm{FB}} > \gamma\omega_d.$$

where γ is a factor denotes the suppression performance of disturbances. γ should be as large as possible to reject more disturbances. The modeling error, drifts, offset and other disturbances lower than ω_d can be suppressed by K_{FB}.

The bandwidth of the feedback controller is also limited to the frequency ω_{bc} to guarantee the robust stability under the modeling error δ, measurement noise n and the coupling with feedforward controller at high frequencies. ω_{bc} can be estimated by the Nyquist stability criterion.

$$\omega_{\mathrm{FB}} < \omega_{bc}.$$

Additionally, the computational complexity of the feedback controller K_{FB} is another

limitation. Let the maximum calculation time of K_{FB} is T_{FB}. T_{FB} increases as the order and the complexity of K_{FB} increase. To guarantee the accurate updating of feedback control signals in real-time implementation, the feedback bandwidth should satisfy

$$\omega_{\mathrm{FB}} < \frac{1}{T_{\mathrm{FB}}}.$$

Finally, the bandwidth of the feedback controller satisfies

$$\gamma\omega_d < \omega_{\mathrm{FB}} < \min\left(\frac{f_{\max}}{2}, \frac{1}{T_{\mathrm{FB}}}, \omega_{bc}\right). \tag{5.9}$$

Design of Sampling Rate in Feedback Loop

The sampling rate in the feedback loop is related to the feedback bandwidth, the calculating capacity of DSPs, the noise level and the ultimate frequency of a PA. In the real-time control of the PA experiment, too fast sampling in the feedback loop may degrade performance, and even result in instability. First, a DSP needs time to calculate and update the feedback signals, but the calculating capability of a DSP restricts the sampling rate, especially for the complex and modern controllers. Secondly, fast sampling of high gain feedback controllers amplifies the high frequency noise n that may contain signals coinciding with resonant (mode) frequencies of a PA, resulting in serious chattering.

Both the upper and the lower bounds of the sampling rates are necessary for the feedback controller K_{FB}. Let $\bar{f}_{\mathrm{FB}}$ denote the upper bound of sampling rates that can be implemented in a DSP. $\bar{f}_{\mathrm{FB}}$ is mainly related to the calculations of the feedback controller K_{FB}. Additionally, the lower bound of sampling rate $\underline{f}_{\mathrm{FB}}$ is related to the disturbance

bandwidth ω_d, the ultimate frequency ω_r of a PA and the feedback bandwidth ω_{FB}. Thus, the sampling rate f_{FB} in the feedback loop can be given by

$$\underline{f}_{\mathrm{FB}} < f_{\mathrm{FB}} < \bar{f}_{\mathrm{FB}} \tag{5.10}$$

where $\underline{f}_{\mathrm{FB}} = 2\max(\omega_{\mathrm{FB}}, \omega_r, \omega_d)$ and $\bar{f}_{\mathrm{FB}} = \min(f_{\max}, 1/T_{\mathrm{FB}})$.

Fig. 5.3 illustrates a slow sampling rate in the feedback loop. The frequencies of the desired trajectories in Figs. 5.3 (a-c) are 200%, 100% and 50% of the sampling rate.

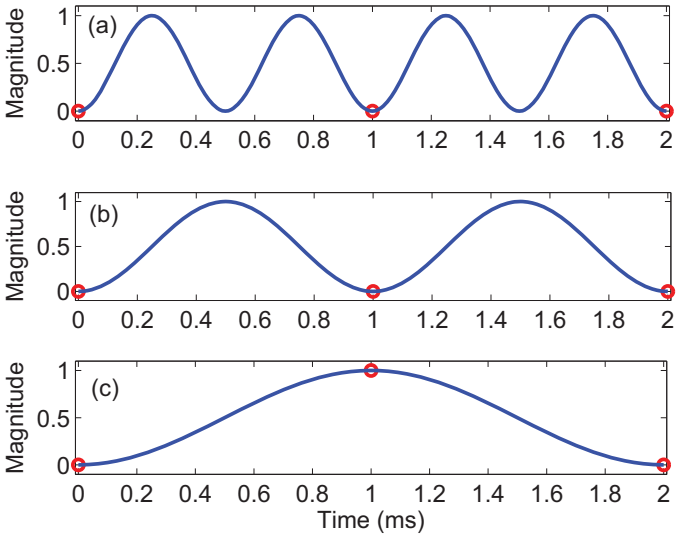

Figure 5.3: Sampling rates of the desired high-frequency trajectories (no unit) in the feedforward and feedback loops. The desired trajectories with fast sampling rate (solid) are employed for the feedforward controller. The sampling points in circle are employed for the feedback controller.

Remark 5.2. *Compared with the sampling in the feedforward loop, insufficient sampling is possible to be employed for the feedback controller when the trajectory rates are beyond the resonant frequencies of PAs. In this case, the feedback controller still rejects disturbances within its bandwidth, but has no tracking performance.*

5.2.4 Design of Discrete Feedback Controller

This section presents the design of the discrete feedback controller according to the sampling rate f_{FB} and the disturbance bandwidth ω_d. Additionally, the loop shaping technique is used. The feedforward controller is effective in reducing phase-lag and achieve high-bandwidth tracking, but there are undesirable modeling errors and other disturbances. It is necessary to design an optimal feedback controller to reject disturbances and guarantee robust stability.

Fig. 5.4 illustrates the loop shaping technique to design the feedback controller. The performance and stability requirements are satisfied by specifying L_1 and L_2. ω_c is the cross frequency of GK_{FB} and is related and close to the feedback bandwidth ω_{FB}, ω_p is related to the disturbance rejection performance, and ω_s is related to the robust stability under modeling errors, disturbances and measurement noise at high frequencies. ω_p and ω_s can be represented as

$$\omega_p = \gamma\omega_d, \quad \omega_s = \min(\frac{f_{\mathrm{FB}}}{2}, \frac{1}{T_{\mathrm{FB}}}, \omega_{bc}). \tag{5.11}$$

Weighting functions are suitable for specifying different requirements at different frequencies as shown in Fig. 5.4. It is convenient to achieve multiple objectives using weighting functions [89]. The robust discrete H_∞ controller is designed based on the non-hysteresis dynamics, while the rate-independent hysteresis Γ can be regarded as an input uncertainty consisting of the nominal gain k_h and the weighting function w_u.

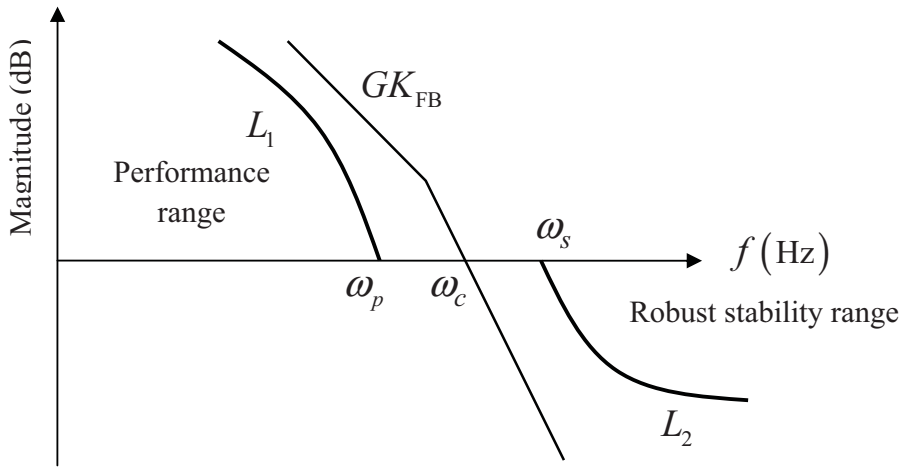

Figure 5.4: Illustration of loop shaping

Fig. 5.5 shows the sketch of the multi-objective robust H_∞ control. w_1 is the performance weighting function to specify performance requirements. Moreover, significant vibrations are easily induced by high gains at high frequencies. Then, an integral action is added to w_1 to reduce the feedback bandwidth ω_{FB} and enhance the disturbance suppression at low frequencies. w_n, w_r and w_d denote the noise, reference and disturbance weighting functions, respectively, w_2 is the control weighting function to limit the control gain and suppress noise at high frequencies, w_u denotes the uncertainty due to the hysteresis nonlinearity, Δ_u is an unit complex uncertainty with norm $\|\Delta_u\| < 1$.

The feedforward control error δ_f can be written as

$$\delta_f = w_\delta \Delta_\delta \tag{5.12}$$

where Δ_δ denotes an unit complex uncertainty with $\|\Delta_\delta\| \leq 1$, w_g is the weighting function to describe the feedforward error.

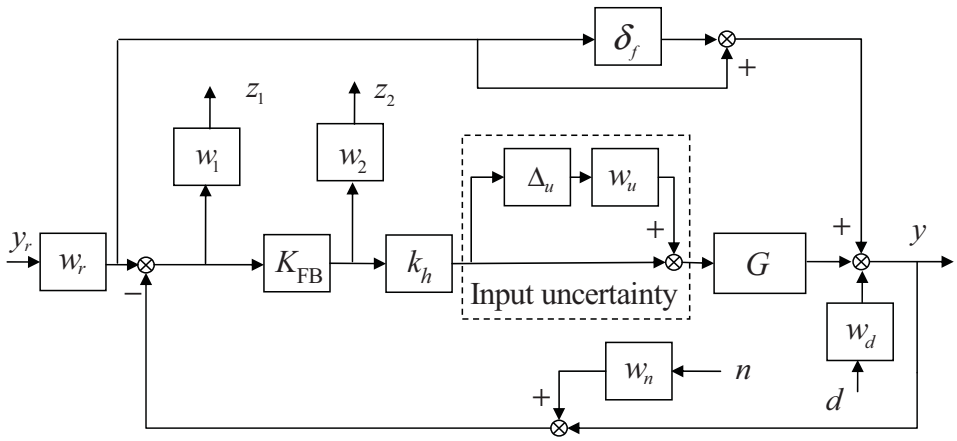

Figure 5.5: Illustration of multi-objective H_∞ control

Weighting functions w_1 and w_2 are employed to satisfy the trajectory requirement of GK_{FB} which is bounded by L_1 and L_2. The relationships are as follow

$$\begin{cases} w_1|_{\omega \le \omega_p} = L_1 \\ w_2|_{\omega \ge \omega_s} = 1/L_2 \end{cases} \tag{5.13}$$

G is the non-hysteretic dynamics of PAs and its identification $\hat{G}$ can be regarded as the nominal model to design the discrete H_∞ controller. The discrete state space of the nominal model can be represented as

$$\begin{cases} x(k+1) = \bar{A}x(k) + \bar{B}v(k) \\ y(k) = \bar{C}x(k) \end{cases} \tag{5.14}$$

where $v(k)$ is the output of rate-independent hysteresis, $\bar{A}$, $\bar{B}$ and $\bar{C}$ can be transformed from the identified non-hysteretic dynamics in PAs. The sampling rate f_{FF} in the feed-forward loop is N times of f_{FB} in the feedback loop, i. e., $f_{\mathrm{FF}} = Nf_{\mathrm{FB}}$.

Remark 5.3. *The specifications and the feedforward control error are incorporated into the feedback controller by loop shaping techniques.*

5.3 Experimental Studies

5.3.1 Proposed Multirate-based Composite Controller

This section presents the multirate-based composite controller of the piezoelectric stage employing the design strategy in Sections 5.2.2 and 5.2.4. The model-based inversion feedforward is achieved first. In addition, the maximum sampling $f_{\max}$ of the DSPACE 1104 board is 40 kHz. The sampling rate in the feedforward loop is then set to 40 kHz.

After testing the feedforward performance, the feedforward-error function δ, without considering the offset and drifts in the displacement y, is less than 5%. Thus, w_δ is set to 0.05. Based on the identified Preisach hysteresis, the nominal gain k_h of the hysteresis is 0.96, and the weighting function w_u reflecting the input uncertainty is set to 0.12. The disturbances, such as displacement offset and drifts, are at frequencies less than 20Hz, indicating that the disturbance bandwidth ω_d is 20Hz. To reject more disturbances, $\gamma = 2$ and w_p=40Hz are used in the experiment.

The ultimate frequency of the piezoelectric stage is 500Hz, i. e., ω_r=500Hz. Moreover, let ω_{bc} be equal to ω_r in this chapter. To reduce high frequency noise and induced vibrations, w_s is set to 350Hz. The requirement of $1/T_{\mathrm{FB}}$ is tested using the designed controller in the PA experiment. The sampling rate f_{FB} is a more flexible parameter to design. In this chapter, much slower f_{FB} is tested, such that the multirate-based composite controller can be performed in a slow DSP. The lower bound due to the feedback bandwidth, ultimate frequency and disturbance bandwidth in Eq. (5.10) is 1 kHz.

According to w_p and w_s in (5.11), with the sampling rate f_{FB} of 1 kHz in the feedback loop, weighting functions w_1 and w_2 used for H_∞ control are as follows

$$\begin{cases} w_1 = 0.1(z+1)/(z-1) \\ w_2 = 1.2496(z-0.2283)^2/(z+0.7254)^2 \end{cases} \tag{5.15}$$

where $(z+1)/(z-1)$ is the integral action of w_1.

With the same f_{FB}, the reference signal, disturbances and measurement noise are represented by the weighting functions w_r, w_d and w_n, respectively

$$\begin{cases} w_r = 1 \\ w_n = 0.0395(z-0.9691)/(z+0.222) \\ w_d = 0.1182(z+1)/(z-0.8818) \end{cases} \tag{5.16}$$

Doyle presented an analytical solution of H_∞ optimization, but the optimization through H_∞ norm is conservative. To reduce the conservation, the discrete D-K iteration with structured singular values is used to solve the controller [89]. Using the weighting functions in (5.15) and (5.16), the structure singular value is 0.81 after 4 discrete D-K iterations. The robust stability is satisfied according to small gain theorem. The H_∞ controller is as follows

$$K_{\mathrm{FB}}(z) = k_z \prod_{j=1}^{k} \frac{z + z_{kj}}{z + p_{kj}} \tag{5.17}$$

where k is the order of the controller, $k = 15$, $k_z = 0.1665$, the zeros of $K_{\mathrm{FB}}(z)$ are $-1, -0.6836 \pm 0.6529\mathrm{i}$, -0.7254, $-0.2088 \pm 0.4324\mathrm{i}$, $-0.2220, -0.0266$, 0.6938, 0.8603, 0.9170, 0.9825, 0.9989, 0.9998, and 1.0000, and the poles of $K_{\mathrm{FB}}(z)$ are $-0.682 \pm 0.614\mathrm{i}$, $-0.0996 \pm 0.4964\mathrm{i}$, $-0.3081 \pm 0.3721\mathrm{i}$, $-0.2345 \pm 0.0369\mathrm{i}$, $0.9730 \pm 0.0168\mathrm{i}$, 0.9987, 0.9997, 0.9998, and 1.0000.

5.3.2 Performance of Proposed Composite Controller

For easy implementation, the harmonic signal $r(t)$ is chosen as the desired trajectory and given by

$$y_r(t) = A\frac{1 - \cos 2\pi ft}{2} \tag{5.18}$$

where A is the amplitude of the reference trajectory $y_r(t)$, t is time, f is the desired frequency. The percent root-mean-square (RMS) error e_{rms} is used to measure the tracking performance.

To verify the effectiveness of the proposed multirate composite controller, the tracking performances at 500Hz (ultimate frequency of the piezoelectric stage) and 1 kHz are investigated. The phase-drop of the PA at 500Hz and 1 kHz are 180° and 390°, respectively. The magnitudes of $r(t)$ at frequencies 500Hz and 100Hz are set to 21μm and 10.25 μm, respectively. The sampling rates in the feedback and feedforward loops are set to 1 kHz and 40 kHz, respectively.

Transient Responses Under Disturbances

Fig. 5.6 shows the transient responses of tracking errors using the proposed multirate composite controller with the specified $r(t)$ at 500Hz and 1 kHz, respectively. The tracking errors are reduced to the steady values after 20 milliseconds (ms). Thus, the performance of disturbance suppression of the feedback controller is verified. The corresponding steady responses are presented in next section.

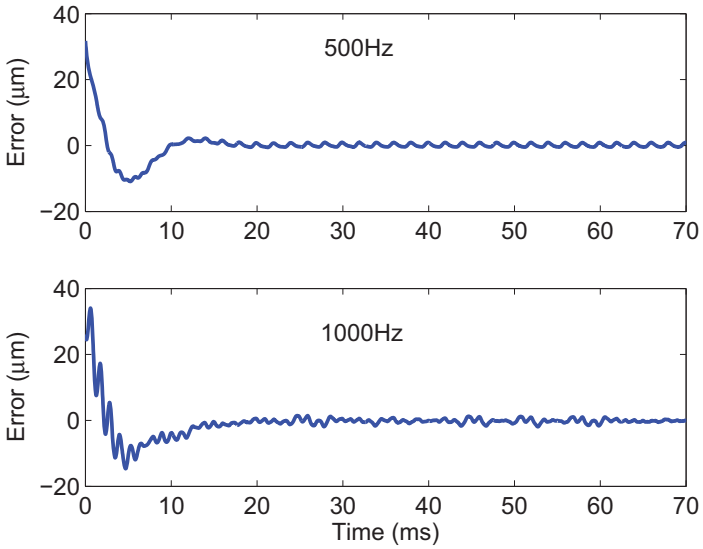

Figure 5.6: Tracking errors under disturbances

Steady Responses

The steady responses of the piezoelectric stage at 500 Hz and 1 kHz are presented, respectively. Figs. 5.7 (a-b) show the tracking performance at 500Hz, the RMS tracking error is 0.486μm and its e_{rms} is 2.3%. Figs. 5.7 (c-d) show the feedforward and feedback control signals. In each period, 80 sampling points of feedforward signals, which are computed off-line, are used to track the desired $r(t)$, but only 2 points of the reference and the measured displacement are used for feedback to reject disturbances.

Figs. 5.8 (a-b) show the tracking performance at 1 kHz (twice the ultimate frequency), the RMS tracking error is 0.226μm and the e_{rms} is 2.2%. Figs. 5.8 (c-d) show the feedforward and the feedback control signals in voltage. In each period, 40 sampling points of feedforward signals are used to track the reference, but only 1 point of the reference and the measured displacement are used for feedback control to reject disturbances.

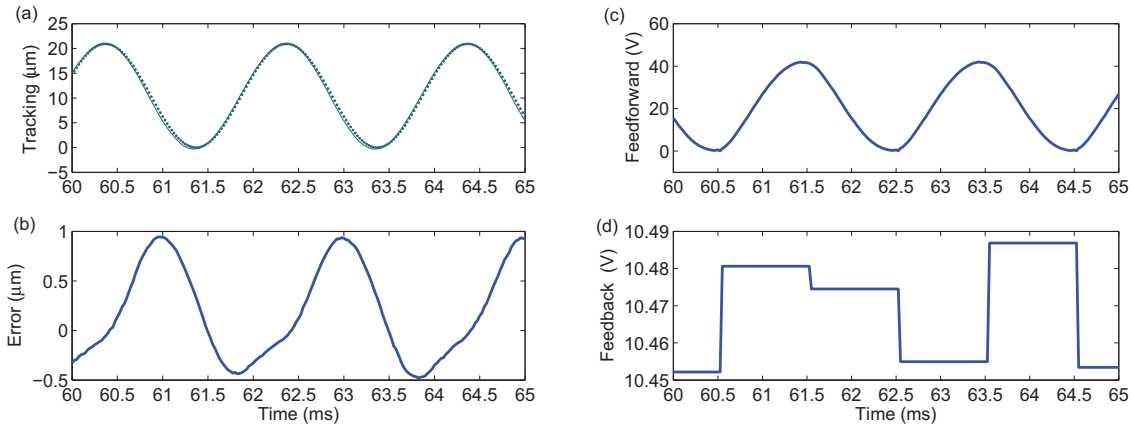

Figure 5.7: Tracking performance and control signals at 500Hz. (a): Tracking performance(solid: actual displacement; dotted: desired displacement); (b): Tracking error; (c): Feedforward control signal; (d): Feedback control signal.

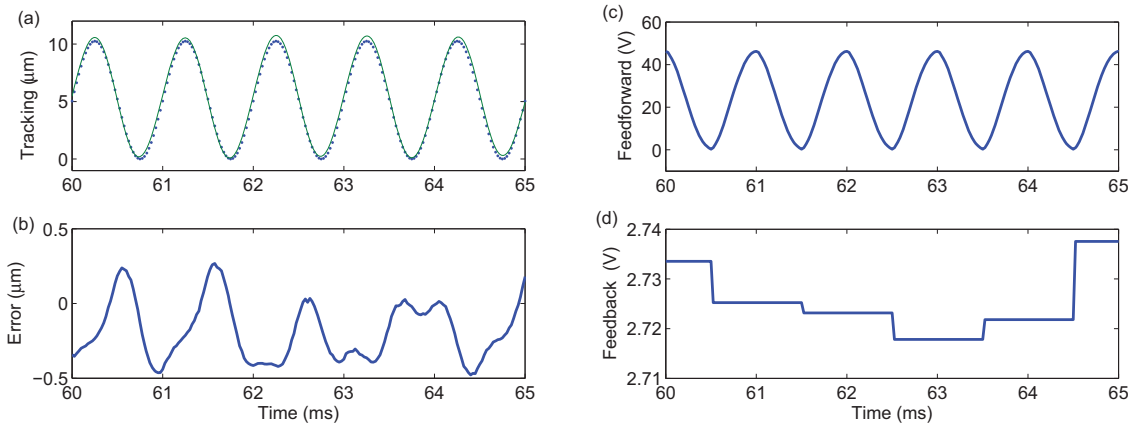

Figure 5.8: Tracking performance and control signals at 1 kHz. (a): Tracking performance (solid: actual displacement; dotted: desired performance); (b): Tracking error; (c): Feedforward control signal; (d): Feedback control signal.

Figs. 5.9 (a-b) show the power spectral densities (PSDs) of the feedforward and the feedback control signals at 500 Hz and 1 kHz, respectively. The PSDs of the feedback control signals are less than 200Hz, since the H_∞ feedback controller is designed to suppress modeling error and disturbances at low frequencies and its bandwidth is less than the resonant frequency. The PSDs of the feedforward control signals are the largest at the reference frequencies, i. e., 500 Hz and 1 kHz, respectively.

The control signals and their PSDs in Figs. 5.7 (b), 5.8 (b) and 5.9 (a-b) indicate that the feedforward control achieves fast tracking at high frequencies and the feedback control rejects disturbances within the feedback bandwidth.

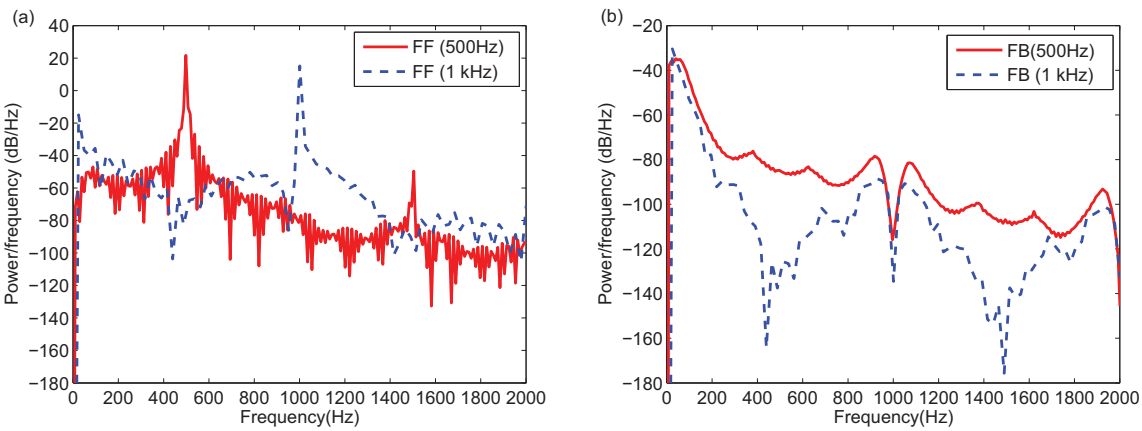

Figure 5.9: PSDs of feedforward and feedback control signals at 500Hz and 1 kHz. (a): PSDs of feedforward control signals (FF: feedforward); (b): PSDs of feedback control signals (FB: feedback).

Remark 5.4. *The experimental studies of a piezoelectric stage have demonstrated the effectiveness of the proposed composite controller. The feedforward controller successfully contributes to the broadband tracking at rates higher than the resonant frequency of the piezoelectric stage. In contrast, the robust feedback controller sufficiently rejects*

disturbances and modeling errors within feedback bandwidth. The phase-drops of the piezoelectric stage at 500Hz and 1 kHz are up to 180° and 390°, respectively, but the smooth and precision tracking are still achieved at 500Hz and 1 kHz.

5.3.3 Performance of Single-rate Composite Controller

The single-rate composite controller is also tested. The proposed composite controller in Section 5.3.2 is transformed to the corresponding single-rate controller. If both the feedforward and the feedback loops have a slow sampling rate of 1 kHz, the composite controller cannot track trajectories at rates higher than 500Hz. To track the trajectories both at 500 Hz and 1 kHz, 40 kHz sampling rate is used for both the feedforward and feedback loops.

The composite controller in (5.17) is transformed into the single-rate controller with the sampling rate of 40 kHz. However, the full-order composite controller cannot be implemented in the DSPACE 1104 board. The error "task over-run" occurs until the order of the H_∞ controller is reduced to 10. The tracking performance with the reduced-order composite controller is degraded compared to the multirate case in Section 5.3.2, and the corresponding tracking accuracies are degraded by 68% and 46% at 500Hz and 1 kHz, respectively.

5.3.4 Discussion

Both high-bandwidth and precision tracking are achieved by the multirate-based composite controller which employs a fast sampling rate in the feedforward loop to achieve

high-bandwidth tracking, but a slow sampling rate in the feedback loop to reject disturbances. Furthermore, the slow sampled feedback controller can be performed in a modest DSP. In the experimental studies, the percent RMS tracking errors at 500 Hz and 1 kHz are less than 2.2% and 2.3%, respectively.

The tracking performance of the multirate-based composite controller is better than the single-rate composite controller with either a slow or a fast sampling rate. The slow sampled single-rate composite controller is not sufficient to track high-frequency trajectories. Conversely, overrun errors easily occur in the fast sampled single-rate composite controller.

In most published works to the best of the authors' knowledge, the precision tracking rates are still lower than the resonant frequency. For instance, [25] proposes a high gain feedback controller augmented with a inversion feedforward based on linear vibration dynamics. The tracking error e_{rms} with a maximum rate of 450Hz is 10.15%, while the first resonant frequency of the PA is 486Hz. In this chapter, we employ a multirate composite controller based on the complete modeling comprising the coupled hysteresis, creep, electric and vibration dynamics. Fine tracking can be achieved at rates beyond the first resonant frequency of the piezoelectric stage.

5.4 Conclusion

In this chapter, a multirate-based composite controller is designed for simultaneous high-bandwidth and precision tracking of PAs. The fast sampled feedforward controller

approaches broadband tracking. The slow sampled controller rejects disturbances. The experimental results validate that the proposed composite controller presents precision tracking at rates twice higher than the first resonant frequency.

Chapter 6

Conclusions

6.1 Summary of Contributions

To achieve high-bandwidth and precision motion control of piezoelectric actuators (PAs), this thesis has investigated the identification and compensation of hysteretic dynamics over a broad range of frequencies.

First, at low frequencies, this thesis investigates the identification and compensation strategy of Preisach hysteresis. The SVD-based least squares estimation is presented. Additionally, the online updating of the Preisach hysteresis identification is provided. The Preisach-based inversion compensation validates the identification of the Preisach hysteresis. With the Preisach-based inversion compensator, the reference tracking of the PID tuning control is significantly improved.

Next, based on the identification result of the Preisach hysteresis, electric and vibration dynamics, the model-based composite compensation is designed, which contains a model-based inversion feedforward compensator and a PI tuning feedback controller. In the experimental studies, the compensation approach is effective at rates faster than the

first resonant frequency of the piezoelectric stage. The inversion feedforward and the PI feedback controllers are employed for the hysteretic dynamics compensation and disturbance rejection, respectively.

Then, over a broad band range of frequencies, the comprehensive identification of the hysteretic dynamics is provided, consisting of the identification of the Preisach hysteresis, creep, electric and vibration dynamics. The identification metrology is effective at broadband frequencies, which is demonstrated in the experimental results.

Finally, by using the identification result of the comprehensive methodology, the multirate-based composite controller is designed for simultaneous high-bandwidth and precision tracking of PAs. With different sampling rates in the feedforward and feedback branches, the model-based inversion feedforward controller is effective to compensate the hysteretic dynamics over a broad range of frequencies. Conversely, the feedback controller is effective to suppress disturbances within the feedback bandwidth.

The systemic identification and compensation of hysteretic dynamics have been investigated in this thesis. Simultaneous high-bandwidth and precision motion control of PAs have been achieved in experimental studies. Based on the accurate identification, the piezoelectric stage tracks the desired trajectories at rates higher than the resonant frequencies.

6.2 Suggestions for Future Work

Although both the identification strategies and the compensation approaches have been investigated in this thesis, there are still improvements which can be achieved. Further investigations of the identification and compensation issues in PAs are suggested as follows:

- Transfer functions can be used to represent creep dynamics in this thesis. However, if the input voltage has a large range, hysteretic creep model can be used to enhance the modeling accuracy.

- The coupled Preisach hysteresis, creep, electric and vibration dynamics have been identified step-by-step in this thesis by employing designed input signals, but the treatment can result in undesirable errors. Thus, the simultaneous identification of the coupled components can be performed to reduce undesirable errors.

- This thesis presents the offline compensation of the hysteretic dynamics under periodic trajectories, but the online compensation of hysteretic dynamics under general trajectories is still not presented in this thesis. The online compensation can be extended to the unknown general trajectories.

- There is high-order derivative in the inversions of the electric and vibration dynamics. The derivative is sensitive to noise and computational errors. To implement the inversions online, it is necessary to design a differentiator which is robust in the face of noise and computational errors.

The suggested future work could improve the identification and compensation accuracy of hysteretic dynamics in PAs. Hysteretic creep and simultaneous identification can improve the modeling accuracy over a large input range. Online model-based inversion compensators can be designed to track unknown general trajectories. Additionally, the differentiator is less sensitive to noise and computational errors, compared with derivative.

Appendix A

A.1: Properties of Preisach Hysteresis

This section presents three properties of Preisach model, i. e., the rate-independence, memory rules and wiping out properties, which will be employed to construct the identification strategy of the coupled hysteresis.

Rate-independence. The rate-independence property is represented as [28, 33]

$$\Gamma[u \circ \varphi] = \Gamma[u] \circ \varphi \tag{6.1}$$

where $\circ$ the composition operator, and φ is increasing function mapping the considered time onto itself.

Figs. 6.1(a-b) illustrates the rate-independence of Preisach model. The input signal has a constant amplitude but varying frequencies. The resultant hysteresis curve of the hysteresis output versus the input voltage is still invariant.

Remark: The rate-independence property indicates that adequate frequencies are not helpful to improve identification of Preisach hysteresis, which is different from the identification of non-hysteretic dynamics where adequate frequencies are necessary to achieve accurate identification.

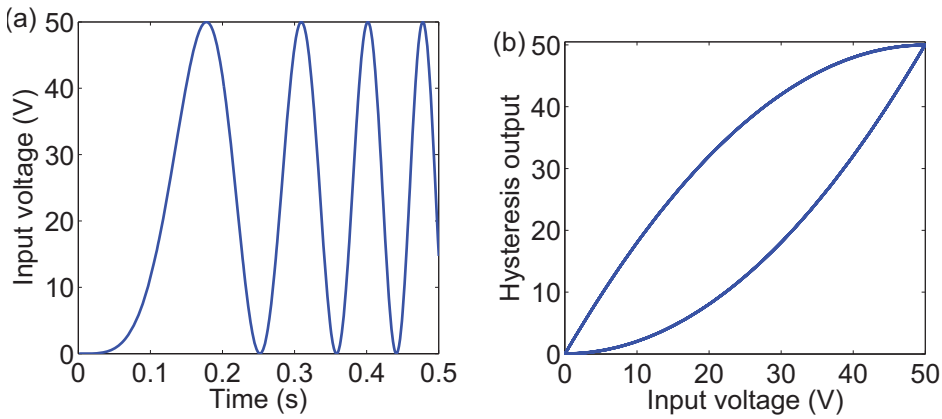

Figure 6.1: Illustration of rate-dependence of Preisach model. (a): Input voltage with constant amplitude but variant frequencies. (b): Hysteresis curve of the hysteresis output versus input voltage.

Memory rules and wiping out property. The details of memory rules of Preisach model is described in Ref. [29]. Figs. 6.2(a-b) shows the memory rules of Preisach model.

As the input signal $u(t)$ is monotonically increased from zero to the local maximum value M_1, all the hysteresis operators $\gamma_{\alpha\beta}[u(t)]$ with switching values less than M_1 will be activated. Next, the input signal is monotonically decreased from the local maximum value M_1 to the local minimum value m_1, the $\gamma_{\alpha\beta}[u(t)]$ with switching values larger than m_1 becomes deactivated. Geometrically, this corresponds to a division of the limiting triangle into two regions, i.e., the activated S^+ and the deactivated S^-, as shown in Fig. 6.2(b). If $M_2 > M_1$, the extreme M_1 and m_1 will be deleted in the Preisach memory according to the wiping out property. The three properties of Preisach model will be employed to identify the coupled hysteresis and creep dynamics.

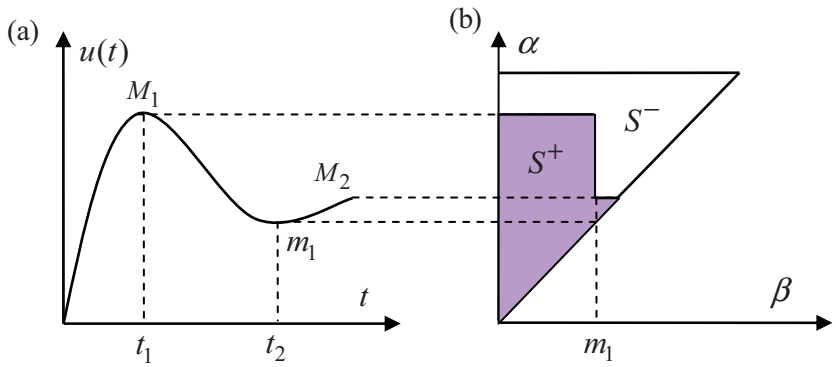

Figure 6.2: Illustration of memory rules of Preisach model. (a): Input signal. (b): Hysteresis representation in Preisach plane.

A.2: PE condition Under Designed Input Signals and Sampling Rules

A.2.1: Proposed Inputs and Sampling law

The section illustrates the satisfaction of the PE condition by employing the input in equation (4.6) and the sampling in equation(4.10). For instance, let $N = 1$, $\delta = 1$, $\delta_s = 1$, $\omega_{\mathrm{r}} = \pi$, and $T = 8$. The density values of 10 grids are needed to be identified. According to the input signal and the sampling rule, partial sampling points are collected and used. Fig. 6.3 illustrates the sampling points corresponding to the discretization points on the Preisach plane in the first 4 periods. It can be seen that 10 samples are collected in the first 4 periods.

According to the discretization of the Preisach model, the matrix A for the 10 sampling points is obtained as shown in (6.2). Furthermore, one non-singular matrix E can be used to pre-multiply matrix A to exchange the columns of A, such that the following EA is achieved as shown in (6.2).

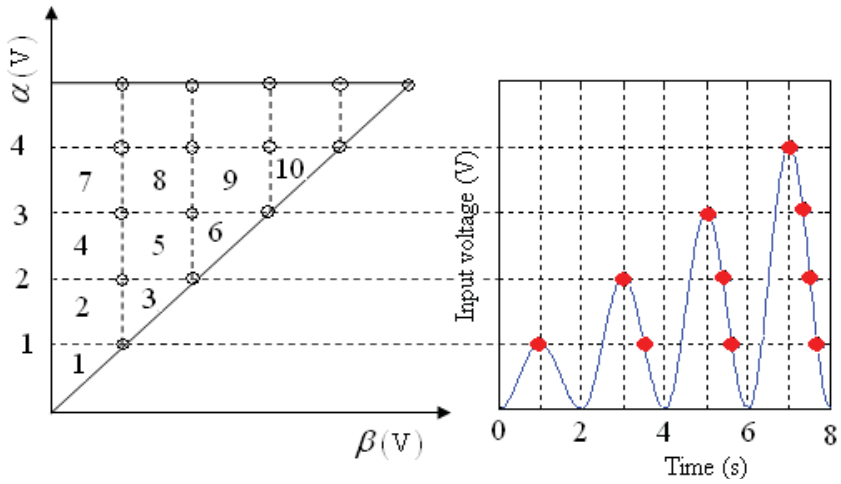

Figure 6.3: Illustration of sampling points.

The matrix EA is lower triangular and full rank. Thus, the matrix A is also non-singular and full rank because of the non-singularity of E. According to the sampling law, the special sampling points are reserved in matrix A. If the detailed disretization is applied, the matrix $A^T A$ is still non-singular and full rank. Finally, the PE condition in the estimation equation (4.14) is satisfied.

$$A = \begin{bmatrix} 1 & 0 & 0 & 0 & 0 & 0 & 0 & 0 & 0 & 0 \\ \hline 1 & 1 & 1 & 0 & 0 & 0 & 0 & 0 & 0 & 0 \\ 1 & 1 & 0 & 0 & 0 & 0 & 0 & 0 & 0 & 0 \\ \hline 1 & 1 & 1 & 1 & 1 & 1 & 0 & 0 & 0 & 0 \\ 1 & 1 & 1 & 1 & 1 & 0 & 0 & 0 & 0 & 0 \\ 1 & 1 & 0 & 1 & 0 & 0 & 0 & 0 & 0 & 0 \\ \hline 1 & 1 & 1 & 1 & 1 & 1 & 1 & 1 & 1 & 1 \\ 1 & 1 & 1 & 1 & 1 & 1 & 1 & 1 & 1 & 0 \\ 1 & 1 & 1 & 1 & 1 & 0 & 1 & 1 & 0 & 0 \\ 1 & 1 & 0 & 1 & 0 & 0 & 1 & 0 & 0 & 0 \end{bmatrix}, \; EA = \begin{bmatrix} 1 & 0 & 0 & 0 & 0 & 0 & 0 & 0 & 0 & 0 \\ \hline 1 & 1 & 0 & 0 & 0 & 0 & 0 & 0 & 0 & 0 \\ 1 & 1 & 1 & 0 & 0 & 0 & 0 & 0 & 0 & 0 \\ \hline 1 & 1 & 0 & 1 & 0 & 0 & 0 & 0 & 0 & 0 \\ 1 & 1 & 1 & 1 & 1 & 0 & 0 & 0 & 0 & 0 \\ 1 & 1 & 1 & 1 & 1 & 1 & 0 & 0 & 0 & 0 \\ 1 & 1 & 0 & 1 & 0 & 0 & 1 & 0 & 0 & 0 \\ 1 & 1 & 1 & 1 & 1 & 0 & 1 & 1 & 0 & 0 \\ 1 & 1 & 1 & 1 & 1 & 1 & 1 & 1 & 1 & 0 \\ 1 & 1 & 1 & 1 & 1 & 1 & 1 & 1 & 1 & 1 \end{bmatrix}. \tag{6.2}$$

A.2.2: PE Condition Using Standard Inputs and Sampling

Next, the input signals with constant amplitude and the time-based sampling (uniformly over time) are used for comparison. In this section, two inputs are considered. Fig. 6.4 (a) shows the input with a constant frequency of 0.5 Hz and a constant amplitude of 4V. Fig. 6.4 (b) shows the input with a constant amplitude of 4V but varying frequencies. The sampling is based on time and the sapling interval is set to 0.01s. According to the Preisach discretization in Section 6.2, the matrix A is achieved. In both cases, 800 points are collected and used in 8 seconds. However, the rank of $A^T A$ in both cases is 7. The PE condition in both cases is not satisfied.

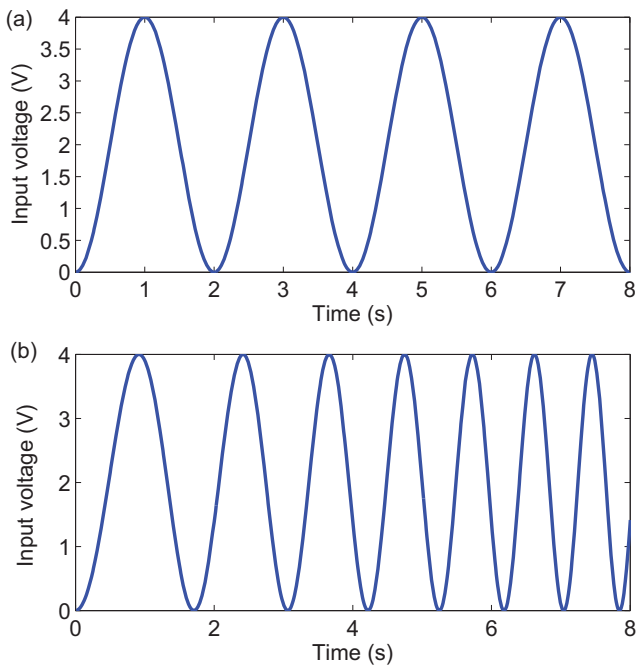

Figure 6.4: Two standard inputs. (a): The input signal with a fixed amplitude. (b): The input signal with varying frequencies.

Bibliography

[1] Physik Instrumente GmbH, "Piezoe-driven nanopositioning and scanning stages, high-dynamcis tip/tilt steering mirrors," http://www.physikinstrumente.com/en/products/nanopositioning/index.php, accessed Apr. 2012.

[2] L. M. Picco, L. Bozec, A. Ulcinas1, D. J. Engledew, M. Antognozzi, M. A. Horton, and M. J. Miles, "Breaking the speed limit with atomic force microscopy," *Nanotechnol.*, vol. 18, no. 4, pp. 044030. 2007.

[3] A. A. Tseng, "Advancements and challenges in development of atomic force microscopy for nanofabrication," *Nano Today*, vol. 6, pp. 493–509, Sept. 2011.

[4] S. Polit and J. Dong, "Development of a high-bandwidth XY nanopositioning stage for high-rate micro/nanomanufacturing," *IEEE/ASME Trans. Mechatron.*, vol. 16, no. 4, 724–733, Aug. 2011.

[5] A. D. Humphris, M. J. Miles, and J. K. Hobbs, "A mechanical microscope: high-speed atomic force microscopy,"*Appl. Phys. Lett.*, vol. 86, no. 3, pp. 034106, Jan. 2005.

[6] Y.-L. Zhang, Q.-D. Chen, H. Xia, and H.-B. Sun, "Designable 3D nanofabrication by femtosecond laser direct writing," *Nano Today*, vol. 5, no. 5, pp. 435–448. Sept. 2010.

[7] X. Jiang, G. Wu, Z. Du, K.-J. Ma, J. Shirakashi, and A. A. Tseng, "Nanoscale scratching of platinum thin films using atomic force microscopy with DLC tips," *J. Vac. Sci. Technol. B*, vol. 30, no. 2, Mar. 2012.

[8] K. Sugihara, I. Mori, T. Tojo, C. Ito, M. Tabata, and T. Shinozaki, "Piezoelectrically driven XY table for submicron lithography systems," *Rev. Sci. Instrum.*, vol. 60, no. 9, pp. 3024–3029, 1989.

[9] J. C. Rubio, J. G. Dubuch, and A. Vieira Porto, "Micropositioning device using solid state actuators for diamond turning machines: A preliminary experiment," *Proc. SPIE*, 1997, vol. 3044, pp. 317–326.

[10] A. A. Tseng, "Three-dimensional patterning of nanostructures using atomic force microscopes," *J. Vac. Sci. Technol. B*, vol. 29, no. 4, pp. 040801. Aug. 2011.

[11] C. M. Olmos, L. G. Villanueva, P. D. van der Wal, A. Llobera, N. F. de Rooij, J. Brugger, and F. Perez-Murano, "Conductivity of SU-8 thin films through atomic force microscopy nano-patterning," *Advanced Functional Materials*, vol. 22, no. 7, pp. 1482-1488. Apr. 2012.

[12] T. Ando, T. Uchihashi, and T. Fukuma, "High-speed atomic force microscopy for nano-visualization of dynamic biomolecular processes," *Progress in Surface Science*, vol. 83, pp. 337–437. 2008.

[13] F. M. Salem, "Ultra-high speed atomic force microscopy: videorate and beyond," *IEEE International Symposium on Circuits and Systems (ISCAS)*, Jun. 2010. pp. 1197–1200.

[14] T. Ando, "High-speed atomic force microscopy coming of age," *Nanotechnol.*, vol. 23, no. 6, pp. 062001. Feb. 2012.

[15] A. J. Fleming, "High-speed vertical positioning for contact-mode atomic force microscopy," *IEEE/ASME International Conference on Advanced Intelligent Mechatronics*, Singapore, Jul. 2009. pp. 522–527.

[16] T. Ando, T. Uchihashi, N. Kodera, D. Yamamoto, A. Miyagi, M. Taniguchi, and H. Yamashita, "High-speed AFM and nano-visualization of biomolecular processes," *Pflugers Arch.–Eur. J. Physiol.*, vol. 456, no. 1, pp. 211–225. Apr. 2008.

[17] K.-C. Liua, C. Blaurock, J. Alexander, and L. Dewell, "Terrestrial planet finder coronagraph pointing control system design and evaluation for flight baseline," *Proc. SPIE*, vol. 5687, doi. 10.1117/12.619329. pp. 56870Z. 2005.

[18] D. M. Boroson, J. J. Scozzafava, D. V. Murphy, and B. S. Robinson, "The lunar laser communications demonstration (LLCD)," *IEEE International Conference on Space Mission Challenges for Information Technology*, 2009. pp. 23-28.

[19] B. J. Smernoff. "The Strategic Value of Space-Based Laser Weapons," *Air University Review*. vol. 33, no. 3, pp. 2–7. Mar. 1982.

[20] T.T. Hyde, K-C. Liu, C. Blaurock, J. Bolognese, J. Howard, W. Danchi, "Requirements formulation and dynamic jitter analysis for Fourier-Kelvin stellar interferometer," *Proc. of SPIE*, vol. 5497, doi. 10.1117/12.552186. pp.553–564. 2004.

[21] Y. Xie, Y. Tan, and R. Dong, "Nonlinear modeling and decoupling control of XY micropositioning stages with piezoelectric actuators," *IEEE/ASME Trans. Mechatron.*, doi. 10.1109/tmech.2012.2187794. Mar. 2012.

[22] M. Mohammadzaheri, S. Grainger, and M. Bazghaleh, "A comparative study on the use of black box modelling for piezoelectric actuators," *Int. J. Manuf. Technol.*, doi: 10.1007/s00170-012-3987-5, Feb. 2012.

[23] S. O. Moheimani, "Accurate and fast nanopositioning with piezoelectric tube scanners: emerging trends and future chanllenges," *Rev. Sci. Instrum.*, vol. 79, pp. 071101. Jul. 2008.

[24] Y. Li and Q. Xu, "Adaptive sliding mode control with perturbation estimation and PID sliding surface for motion tracking of a piezo-driven micromanipulator," *IEEE Trans. Control Syst. Technol.*, vol. 18, no. 4, pp. 798–810. Jul. 2010.

[25] K. K. Leang and S. Devasia, "Feedback linearized inverse feedforward for creep, hysteresis and vibration compensation in AFM piezoactuators," *IEEE Trans. Control Syst. Technol.*, vol. 15, no. 5, pp. 927–935, Sept. 2007.

[26] M. Goldfarb and N. Celanovic, "Modeling piezoelectric stack actuators for control of micromanipulation," *IEEE Control Syst. Mag.*, vol. 17, no. 3, pp. 69–79, Jun. 1997.

[27] D. Davino, C. Natale, S. Pirozzi, and C. Visone, "Phenomenological dynamic model of a magnetostrictive actuator," *Phys. B: Condensed Matter*, vol. 343, no. 1, pp. 112–116. Jan. 2004.

[28] A. Visintin, *Differential Models of Hysteresis*. New York: Springer-Verlag. 1996.

[29] I. Mayergoyz, *Mathematical Models of Hysteresis*, Belin: Springer-Verlag. 2003.

[30] H. Liaw and B. Shirinzadeh, "Neural network motion tracking control of piezo actuated flexure based mechanisms for micro nanomanipulation," *IEEE/ASME Trans. Mechatron.*, vol. 14, no. 5, pp. 517–527, Oct. 2009.

[31] S. Mittal and C. Menq, "Hysteresis compensation in electromagnetic actuators through Preisach model inversion," *IEEE/ASME Trans. Mechatron.*, vol. 5, no. 4, pp. 394-408, Dec. 2000.

[32] K. Kuhnen, "Modeling, Identification and compensation of complex hysteretic nonlinearities: a modified Prandtl-Ishlinkskii approach," *European J. Control*, vol. 9, no. 4, pp. 407–418. 2003.

[33] C. Visone, "Hysteresis modeling and conpensation for smart sensors and actuators," *J. Phys.: Conf. Ser.*, vol. 138, no. 1, pp. 012028, 2008.

[34] A. Putra, S. Huang, K. K. Tan, and T. H. Lee, "Design, modeling, and control of piezoelectric actuators for intracytoplasmic sperm injection," IEEE *IEEE Trans. Control Syst. Technol.*, vol. 15, no. 5, pp. 879–90. Sept. 2007.

[35] F. Ikhouane and J. Rodellar, "A linear controller for hysteresis systems," *IEEE Trans. Autom. Control*, vol. 51, no. 2, pp. 340–44, Feb. 2006.

[36] H. Hu, "Compensation of hysteresis in piezoceramic actuators and control of nano-positioning system," PhD dissertation, University of Toronto, Toronto, 2003.

[37] G. Song, J. Zhao, and X. Zhou, "Tracking control of a piezoceramic actuator with hysteresis compensation using inverse Preisach model," *IEEE/ASME Trans. Mechatron.*, vol. 10, no. 2, pp. 198–209, Apr. 2005.

[38] R. Iyer, X. Tan, and P. Krishnaprasad, "Approximate inversion of Preisach hysteresis operator with application to control of smart actuators," *IEEE Trans. Autom. Control*, vol. 50, no. 6, pp. 798-809. Jun. 2005.

[39] X. Tan and J. S. Baras. "Adaptive identification and control of hysteresis in smart materials," *IEEE Trans. Autom. Control*, vol. 50, no. 6, pp. 827–839, Jun. 2005.

[40] O. Henze and W. M. Rucker, "Identification procedures of Preisach model," *IEEE Trans. Magn.*, vol. 38, no. 2, pp. 833–836, Mar. 2002.

[41] K. Astrom and B. Wittenmark, *Adaptive control.* New York: Addison-Wesley. 1994.

[42] R. Aster, B. Borcher, and C. Thurber, *Function analysis and inverse problem.* Amsterdam: Elsevier. 2005.

[43] S. S. Aphale, B. Bhikkaji, and S. R. Moheimani, "Minimizing scanning errors in piezoelectric stack-actuated nanopositioning platforms," *IEEE Trans. Nanotechnol.*, vol. 7, no. 1, pp. 79–90, Jan. 2008.

[44] G. M. Clayton, S. Tien, K. K. Leang, Q. Zou, and S. Devasia, "A review of feed-forward control approaches in nanopositioning for high-speed SPM," *ASME J. Dyn. Syst. Control*, vol. 131, pp. 0611011, Nov. 2009.

[45] G. Tao and P. Kokotovic, "Adaptive control of plants with unknown hysteresis," *IEEE Trans. Autom. Control*, vol. 40, no. 2, pp. 200–12, Jan. 1995.

[46] X. Chen, T. Hisayama, and C. Su, "Pseudo-inverse-based adaptive control for uncertain discrete time systems preceded by hysteresis," *Automatica*, vol.45, pp. 469–76, 2009.

[47] J. R. Bunch and C. P. Nielsen, "Updating the singular value decomposition," *Numerical Mathematics*, vol. 31, no. 2, pp.111-129, Jun. 1978.

[48] M. Brand, "Fast online SVD revisions for lightweight recommender systems," *SIAM international conference on data mining.* 2003. pp. 37–48.

[49] J. Lin, H. Chiang, and C. C. Lin, "Tunnung PID control gains for micro piezo-stage using grey relational analysis," *International conference on machine learning and cybernetics*. Jul. 2008. pp. 3863–3868.

[50] Y. Wu and Q. Zou, "Iterative control approach to compensate for both the hysteresis and the dynamics effects of piezo actuators," *IEEE Trans. Control Syst. Technol.*, vol. 15, no. 5, pp. 936–944, Sept. 2007.

[51] L. Liu, K. K. Tan, S. N. Huang, and T. H. Lee, "Identification and control of linear dynamics with input Preisach hysteresis," *American control conference*. June, 2010. pp. 4301–4306.

[52] H. Xie, M. Rakotondrabe, and S. Rgnier, "Characterizing piezoscanner hysteresis and creep using optical levers and a reference nanopositioning stage," *Rev. Sci. Instrum.*, vol. 80, no. 4, pp. 046102, Apr. 2009.

[53] K. Leang, Q. Zou, and S. Devasia, "Feedforward control of piezoactuators in atomic force microscope systems," *IEEE Control Syst. Mag.*, vol. 29, no. 1, pp. 70–82, Feb. 2009.

[54] A. Fleming, "Nanapositioning system with force feedback for high performance tracking and vibration control," *IEEE/ASME Trans. Mechatron.*, vol. 15, no. 3, pp. 433–446, Jun. 2010.

[55] W. Kuo, S. Chuang, C. Nian, and Y. Tarng, "Precision nano-alignment system using machine vision with motion controlled by piezoelectric motor," *Mechatron.*, vol. 18, no. 1, pp. 21–34, 2008.

[56] I. A. Mahmood, S. O. Reza Moheimani, and B. Bhikkaji. "A new scanning method for fast atomic force microscopy," *IEEE Trans. Nanotechnol.*, vol. 10, no. 2, pp. 203–216, Mar. 2011.

[57] I. Mayergoyz, "Dynamic Preisach models of hysteresis," *IEEE Trans. on Magnetics*, vol. 24, no. 6, pp. 2925–2927, Nov. 1988.

[58] M. Janaiden, C. Su, and S. Rakheja, "Development of the rate-dependent Prandtl-Ishlinskii model for smart actuators," *Smart Mater. Struc.*, vol. 17, pp. 035026, Jun. 2008.

[59] M. A. Janaideh, S. Rakheja, and C. Y. Su, "An analytical generalized Prandtl-Ishlinskii model inversion for hysteresis compensation in micropositioning control," *IEEE/ASME Trans. Mechatron.*, vol. 16, no. 4, pp. 734–744, Aug. 2011.

[60] S. Devasia, E. Eleftheriou, and S. Moheimani, "A survey of control issues in nanopositioning," *IEEE Trans. Control Syst. Technol.*, vol. 15, no. 5, pp. 802–823, Sept. 2007.

[61] H. Liaw and B. Shirinzadeh, "Sliding mode cotrol enhanced adaptive motion tracking control of piezoelectric actuation systems for micro/nano manipulation," *IEEE Trans. Control Syst. Technol.*, vol. 16, no. 4, pp. 826–833, Jul. 2008.

[62] H. C. Liaw and B. Shirinzadeh, "Robust adaptive constrained motion tracking control of piezo-actuated flexure-based mechanisms for micro/nano manipulation," *IEEE Trans. Ind. Electron.*, vol. 58, no. 4, pp. 1406–1415, Apr. 2011.

[63] X. Chen and T. Hisayama, "Adaptive sliding-mode position control for piezo-actuated stage," *IEEE Trans. Ind. Electron.*, vol. 55, no. 11, pp. 3927–3934, Nov. 2008.

[64] L. Ljung, *System Identification: Theory for the User, 2nd ed.*, Upper Saddle River, NJ: Prentice–Hall, 1999.

[65] Y. Wu and Q. Zou, "Robust inversion-based 2-DOF control design for output tracking: piezoelectric-actuator example," *IEEE Trans. Control Syst. Technol.*, vol. 17, no. 5, pp. 1069–1082, Sept. 2009.

[66] M. Shibata, H. Yamashita, T. Uchihashi, H. Kandori, and T. Ando, "High-speed AFM and nano-visualization of biomolecular processes," *Nature Nanotechnol.*, vol. 5, no. 3, pp: 208–212, Feb. 2010.

[67] T. Fujita, A. Matsubara, D. Kono, and I. Yamaji, "Dynamic characteristics and dual control of a ball screw drive with integrated piezoelectric actuator," *Precision Eng.*, vol. 34, no. 1, pp. 34–42, Jan. 2010.

[68] R. Merry, M. Massen, and M. Molengraft, "Modeling and waveform optimization of a nano-motion piezo stage," *IEEE/ASME Trans. Mechatron.*, vol. 16, no. 4, pp. 615–626, Aug. 2011.

[69] G. Gu and L. Zhu, "Modeling of rate-dependent hysteresis in piezoelectric actuators using a family of ellipses," *Sensors Actuators A: Phys.*, vol. 165, pp. 303–309, Feb. 2011.

[70] A. Salvini, F. R. Fulginei, and G. Pucacco. "Generalization of the static Preisach model for dynamic hysteresis by a genetic approach," *IEEE Trans. Magn.*, vol. 39, no. 3, pp. 1353–1356, May. 2003.

[71] M. Cirrincione, R. Miceli, and G. R. Galluzzo, "Preisach function identification by neural networks," *IEEE Trans. on Magn.*, vol. 38, no. 5, pp. 2421–2423, Sept. 2002.

[72] D. Guyomar, B. Ducharne, and G. Sebald, "Dynamical hysteresis model of ferroelectric ceramics under electric field using fractional derivatives," *J. Phys. D: Appl. Phys.*, vol. 40, no. 19, pp. 6048–6054, Oct. 2007.

[73] M. Mortell, R. O'Malley, and A. Pokrovskii, *Singular Perturbations and Hysteresis*, Philadelphia: Society for Industial and Applied Mathematics, 2005.

[74] M. A. Krasnoselskii and A. V. Pokrovskii, *Systems with Hysteresis*, translated from the Russian by Marek Niezgodka, New York : Springer-Verlag, 1989.

[75] L. E. Malvern. *Introduction to the Mechanics of a Continuous Medium*, Englewood Clii, NJ: PrenticeHall, 1969.

[76] K. Kuhnen and P. Krejci, "Compensation of complex hysteresis and creep effects in piezoelectrically actuated systems– a new Preisach modeling approach," *IEEE Trans. Autom. Control*, vol. 54, no. 3, pp. 537–550, Mar. 2009.

[77] B. Bhikkaji and S. O. Moheimani, "Integral resonant control of a piezoelectric tube actuator for fast nanoscale positioning," *IEEE/ASME Trans. Mechatron.*, vol. 13, no. 5, pp. 530–537, Oct. 2008.

[78] A. Dubra, J. S. Massa, and C. Paterson, "Preisach classical and nonlinear modeling of hysteresis in piezoceramic deformable mirrors," *Opt. Express*, vol. 13, no. 22, pp. 9062-9070, Oct. 2005.

[79] P. Ge and M. Jouaneh, "Generalized Preisach model for hysteresis nonlinearity of piezoceramic actuators," *Precision Eng.*, vol. 20, pp. 99–111, Mar. 1997.

[80] M. Rakotondrabe, C. Clvy, and P. Lutz, "Complete open loop control of hysteretic, creeped, and oscillating piezoelectric cantilevers," *IEEE Trans. Autom. Sci. Eng.*, vol. 7, no. 3, pp. 440–450, Jul. 2010.

[81] L. Juhasz, J. Maas, and B. Borovac, "Parameter identification and hysteresis compensation of embedded piezoelectric stack actuators," *Mechatron.*, vol. 21, no. 1, pp. 329–338, Feb. 2011.

[82] H. Adriaens, W. L. Koning, and R. Banning, "Modeling piezoelectric actuators," *IEEE/ASME Trans. Mechatron.*, vol. 5, no. 4, pp. 331-341, Dec. 2000.

[83] M. Brokate, "Some mathematical properties of the Preisach model for hysteresis," *IEEE Trans. Magn.*, vol. 25, no. 4, pp. 2922–2924, Jul. 1989.

[84] L. Liu, K. K. Tan, S.-L. Chen, S. Huang, and T. H. Lee, "SVD-based Preisach hysteresis identification and composite control of piezo actuators," *ISA Trans.*, doi. 10.1016/j.isatra.2012.01.002, Jan. 2012.

[85] G. Song, J. Zhao, X. Zhou, and J. Abreu-Garcia, "Tracking control of a piezoceramic actuator with hysteresis compensation using inverse Preisach model," *IEEE/ASME Transacitions on Mechatronics*, vol. 10, vo. 2, pp. 198–209, Apr. 2005.

[86] U. X. Tan, W. T. Latt, C. Y. Shee, C. N. Riviere, and W. T. Ang, "Feedforward controller of ill-conditioned hysteresis using singularity-free Prandtl-Ishlinskii model," *IEEE/ASME Trans. Mechatron.*, vol. 14, no. 5, pp. 598–605, Oct. 2009.

[87] H.-J. Shieh and C.-H. Hsu, "An adaptive approximator-based backstepping control approach for piezoactuator-driven stages," *IEEE Trans. Ind. Electron.*, vol. 55, no. 4, pp. 1729–1738, Ari. 2008.

[88] B. E. Helfrich, C. Lee, D. A. Bristow, and X. H. Xiao, "Combined H_∞-Feedback Control and Iterative Learning Control Design With Application to Nanopositioning Systems," *IEEE Trans. Control Syst. Technol.*, vol. 18, no. 2, pp. 336-351, Mar. 2010.

[89] S. Skogestad and I. Postlethwaite *Multivariable Feedback Control: Design and Analysis,* New York: Wiley, 2005.

[90] H. Fujimoto, Y. Hori, and A. Kawamura, "Perfect tracking control based on multirate feedforward control with generalized sampling periods," *IEEE Trans. Ind. Electron.*, vol. 48, . no. 3, pp. 636–644, Jun. 2001.

[91] H. Fujimoto and B. Yao, "Multirate adaptive robust control for discrete-time nonminimum phase systems and application to linear motors," *IEEE/ASME Trans. Mechatron.*, vol. 10, no. 4, pp. 371–377, Aug. 2005.

[92] K. Saiki, A. Hara, K. Sakata, and H. Fujimoto, "A study on high-speed and high-precision tracking control of large-scale stage using perfect tracking control method based on multirate feedforward control," *IEEE Trans. Ind. Electron.*, vol. 57, no. 4, pp. 1393–1400. Mar. 2010.

[93] W. Cao, Q. Bi, X. Liu, C. Lim, and Y. Soh, "Frequency domain transfer function of digital multirate controller with current estimator," *IEEE Trans. Control Syst. Technol.*, vol. 13, no. 1, pp. 131–137, Jan. 2005.

[94] C. Duan, G. Gu, C. Du, and T. C. Chong, "Robust compensation of periodic disturbances by multirate control," *IEEE Trans. Magn.*, vol. 44, no. 3, pp. 413-418, Feb. 2008.

[95] S.-H. Lee, "Multirate digital control system design and its application to computer disk drives," *IEEE Trans. Control Syst. Technol.*, vol. 14, no. 1, pp. 124–133, Jan. 2006.

[96] M. Brokate and J. Sprekels, *Hysteresis and Phase Transitions.* Berlin-Heidelberg-NewYork: Springer-Verlag, 1996.

[97] L. Liu, K. K. Tan, C. S. Teo, S. L. Chen, and T. H. Lee. "Development of an approach towards comprehensive identification of hysteretic dynamics in piezoelectric actuators," *IEEE Trans. Control Syst. Technol.*, under review.

[98] G. F. Franklin, J. D. Powell, and M. L. Workman, *Digital Control of Dynamic Systems, 3rd ed.* Menlo Park: Addition-Wesley, 1997.

Author's Publications

Journal Papers:

1. Lei Liu, Kok Kiong Tan, and Tong Heng Lee, SVD-based Preisach Hysteresis Identification and Composite Control of Piezo Actuators. *ISA Transactions*, 51(3):430-438, May. 2012.

2. Lei Liu, Kok Kiong Tan, and Tong Heng Lee, Active Vibration Isolation Based on Model Reference Adaptive Control, *International Journal of Systems Science*, doi: 10.1080/00207721.2012.683834, May. 2012.

3. Lei Liu, Kok Kiong Tan, Silu Chen, Chek Sing Teo, and Tong Heng Lee, Discrete Composite Control of Piezoelectric Actuators for High Speed and Precision Scanning, *IEEE Transactions on Industrial Informatics,* accepted. 2012.

4. Lei Liu, Kok Kiong Tan, Chek Sing Teo, Silu Chen, and Tong Heng Lee, Development of an Approach Towards Comprehensive Identification of Hysteretic Dynamics in Piezoelectric Actuators, *IEEE Transactions on Control Systems Technology*, doi: 10.1109/TCST.2012.2200896. 2012.

5. Lei Liu, Kok Kiong Tan, and Tong Heng Lee, Multirate-Based Composite Con-

troller Design of Piezoelectric Actuators for High-Bandwidth and Precision Tracking, *IEEE Transactions on Control Systems Technology*, second round review. 2012.

6. Lei Liu, Kok Kiong Tan, and Tong Heng Lee, SVD-based Accurate Identification and Compensation of the Coupled Hysteresis and Creep Dynamics in Smart Actuators. *Asian Journal of Control*, accepted. 2012.

Conference Papers:

1. Lei Liu, Kok Kiong Tan, Sunan Huang, and Tong Heng Lee, Identification and Control of Linear Dynamics with Input Preisach Hysteresis, *American Control Conference*, Baltimore, USA, 2010, Jun. 4301–4306.

2. Lei Liu, Kok Kiong Tan, and Tong Heng Lee, Online Parameter Estimation and Compensation of Preisach Hysteresis by SVD updating, *18th IFAC World Congress*, Italy, August, 18(1): 5249-5254, 2011.

3. Lei Liu, Kok Kiong Tan, Sunan Huang, and Tong Heng Lee, Flexible Spacecraft Jitter and Its Suppression by Stewart Platform, *23rd Canadian Congress of Applied Mechanics*, Vancouver, Canada, pp.57-60, Jun. 2011.

4. Lei Liu, Kok Kiong Tan, Silu Chen, Chek Sing Teo, and Tong Heng Lee, Identification and Compensation of Hysteretic Dynamics of Piezoelectric Actuators for Accurate and Fast Scanning, *7th IEEE Conference on Industrial Electronics and*

Applications, Singapore, Jul. 2012.

5. Lei Liu, Kok Kiong Tan, Silu Chen, Chek Sing Teo, and Tong Heng Lee,Identification of coupled hysteresis, creep, electric and vibration dynamics in piezoelectric actuators for high bandwidth precision motion control *12th euspen International Conference*, Stockholm, Jun. 2012.